Title
Understanding and Controlling the Chemistry in Liquid Cell Electron Microscopy to Study Nanocrystal Shape Transformations

Author
Hauwiller, Matthew

Publication Date
2019

Peer reviewed|Thesis/dissertation

Understanding and Controlling the Chemistry in Liquid Cell Electron Microscopy to Study Nanocrystal Shape Transformations

by

Matthew R. Hauwiller

A dissertation submitted in partial satisfaction of the

requirements for the degree of

Doctor of Philosophy

in

Chemistry

in the

Graduate Division

of the

University of California, Berkeley

Committee in charge:

Professor A. Paul Alivisatos, Chair
Professor Peidong Yang
Professor Alex Zettl

Spring 2019

Understanding and Controlling the Chemistry in Liquid Cell Electron Microscopy to Study Nanocrystal Shape Transformations

Abstract

Understanding and Controlling the Chemistry in Liquid Cell Electron Microscopy to Study Nanocrystal Shape Transformations

by

Matthew R. Hauwiller

Doctor of Philosophy in Chemistry

University of California, Berkeley

Professor A. Paul Alivisatos, Chair

Nanomaterials exhibit unique size-dependent properties, and colloidal, metallic nanocrystals have been utilized in catalytic, biomedical, and optical applications. Observing the dynamics of nanocrystals in their native liquid environment requires the high spatial resolution of the electron microscope and encapsulation using a thin membrane such as graphene. By understanding and controlling the chemistry during liquid cell electron microscopy reactions, fundamental insights about nanoscale processes can be elucidated to improve colloidal synthesis of nanocrystals.

Oxidative etching of gold nanocrystals using a combination of preloaded $FeCl_3$ and electron beam-generated radiolysis products was used as a model system for learning about the chemistry of the liquid cell environment. By collecting etching trajectories of multiple nanocubes and rhombic dodecahedra, with {100} and {110} facets respectively, as they transition through intermediate {hk0} facets, the initial $FeCl_3$ concentration was found to control the chemical potential of the etching process. Using Monte Carlo simulations to help understand the trajectories, the chemical potential was found to change the intermediate facets when etching from cubes but not rhombic dodecahedra due to differences in coordination of inner surface atoms.

The electron beam generates highly reactive radiolysis products during liquid cell imaging, so determining the electron beam's role on the chemistry of the liquid environment is useful for experimental design and reproducibility. Following the volume trajectories of etching nanocrystals, it was found that the electron beam dose rate controls the etching rate independently of the $FeCl_3$ control of the chemical potential. Further, at low dose rates, the electron beam generates sacrificial reductant hydrogen gas bubbles that prevent premature etching. *Ex situ* etching experiments using $FeCl_3$ confirmed the dynamics observed in the liquid cell and provided additional insight into the liquid cell environment.

Additional *in situ* TEM observations of the nanoscale Kirkendall effect of silver nanoparticles and electron stimulated desorption of NaCl nanocubes shows the wide range of processes that can be investigated. Although the chemistry of these liquid cell processes are not as well

understood as the gold nanocrystal etching, useful insights about structural transformations were extracted.

Finally, an undergraduate research program for first-year students was designed and implemented using liquid cell TEM data. The structure of the program is presented with feedback from the participants showing quantifiable gains in self-identification as scientist.

To all my teachers, especially my Mother and Father

Contents

List of Figures

List of Tables

Acknowledgments

First and foremost, I would like to thank my advisor A. Paul Alivisatos for guiding me along my PhD journey over the past 5 years. I have learned an immense amount and developed as both a scientist and a person. I appreciate that I was given the opportunity to pursue whatever avenues I felt would best allow me to achieve my goals.

Dr. Haimei Zheng has also helped guide my last two years in graduate school as a second advisor and mentor. I have appreciated the opportunity to work with and learn from someone who has a passion for and wealth of knowledge about *in situ* electron microscopy.

I would like to thank my labmates who have been there for me through the celebrations and the struggles. They have constantly pushed me to be a better scientist and researcher. I would especially like to thank the undergraduate researchers who worked with me and contributed to the *ex situ* studies presented in this dissertation: Cindy Chan, Prachi Khandekar, Jessica Yu, and Vishnu Dharmaraj.

My mentors and academic role models have helped me get to where I am today. I would especially like to thank Professor David Blank and Kirk Froggatt for providing invaluable advice throughout my undergraduate and graduate education journeys.

I am extremely grateful for the relationship and support I have found at Holy Spirit-Newman Hall Catholic Church including Fr. Ivan, Fr. Steve, Dylan, Teresa, Jeannie, Estella, Brett, Susan, Howard, and Deborah. Graduate school can be all-consuming, but they kept me grounded while showing me what is important in life. I am especially grateful to Dan Cawthon, whose wisdom, understanding, and love for others was truly saintly.

Ken Montgomery showed me the joy of being a Cal fan and a Californian when I did not see many reasons to like Berkeley. Many of my most memorable moments in California have been with Ken. His excitement for life is inspiring, and I truly am grateful that I can call him a friend.

For the majority of my graduate school career, I have had Mariana Verdugo by my side supporting and caring for me. You have cheered me up when Berkeley has saddened me and been my rock through everything. I am grateful that God put you in my life to help me through the Berkeley experience.

Finally, I want to thank my family for all their support and work that has helped me reach this point. Without my mother, father, and sister, I would not be the person I am today. I am privileged to have you for my family.

Chapter 1

Introduction to Nanocrystals and Liquid Cell Electron Microscopy

As technology in every aspect of life continues to advance at a rapid pace, the need to control matter on even smaller length scales becomes ever more critical. Controlling metal or semiconductor structures made up of hundreds or thousands of atoms formed using colloidal synthesis techniques is useful for a variety of applications. Understanding the underlying principles of how atoms interact and come together to form these tiny structures enables further development of size and shape control.

Colloidal nanocrystals are any crystaline material with length scales on the order of 1 to 100 nm solvated in a liquid solution. Usually, organic ligands are bonded to the surface atoms of the nanocrystal to aid in colloidal stability.[1] The most commonly studied nanocrystal materials are metals and semiconductors. Nanocrystals exhibit many unique, size-dependent properties that render them intriguing to researchers for fundamental studies as well as industry for a variety of applications. For example, nanocrystals have size-dependent melting temperatures[2] and size-dependent optical properties like plasmon resonances in metals[3] and photoluminescence in semi-conductors.[4] Applications for nanocrystals include catalysis,[5,6] energy,[7] optics,[8,9] and biomedicine.[10–13]

Due to the small size of nanocrystals, watching nanocrystals during their dynamic processes can be challenging. Visualizing the movement, growth, etching, or other processes of nanoscale matter is critical to elucidating the underlying mechanisms of the processes, especially for non-equilibrium dynamics. The diameter of the nanocrystal is below the diffraction limit of light, so light microscopy techniques are not suitable for watching nanocrystals. Instead, electron microscopy is used to image nanocrystals. Liquid solutions of nanocrystals are able to be imaged using a technique called Liquid Cell Electron Microscopy. In this dissertation, metallic nanocrystal systems were investigated using liquid cell electron microscopy, and a better understanding of metallic nanocrystal dynamics was developed.

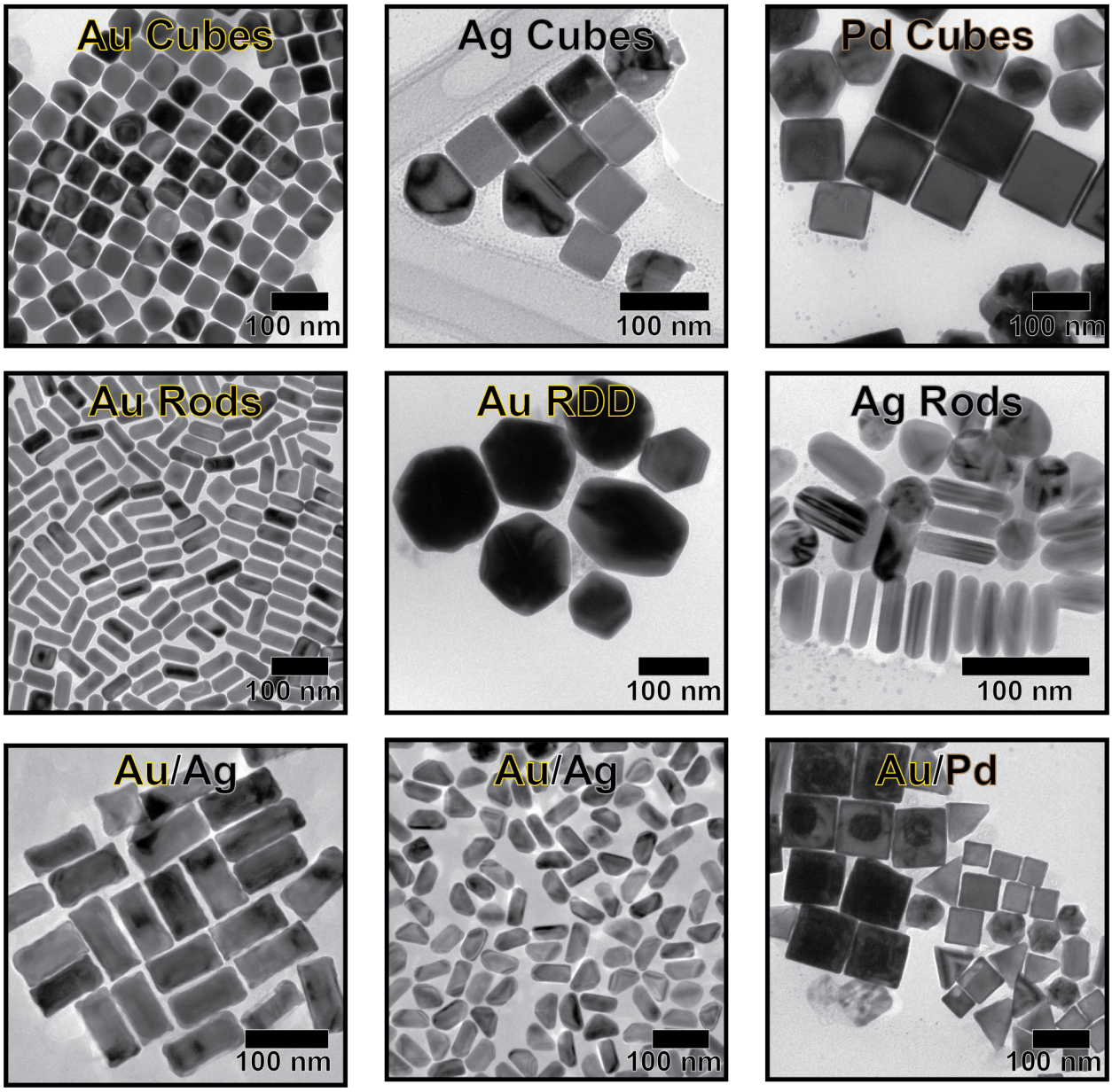

Figure 1.1: Examples of metallic nanocrystal compositions and morphologies including nanocubes of gold, silver, and palladium, gold rods and rhombic dodecahedra, silver rods, and core/shell nanocrystals.These samples are not perfectly monodisperse; however, for single particle liquid cell TEM experiments, monodispersity is not a necessity.

1.1 Metallic Nanocrystals

A large class of nanomaterials that have garnered a significant amount of interest are metallic nanocrystals. Similar to all other types of nanocrystals, the properties of metals change as they go from the bulk to nanoscale, and those properties can be tuned by the composition, faceting, geometric shape, and internal structure.[14] This dissertation will focus on noble metal nanocrystals, but a variety of other metals and metal oxides have been studied in the literature. The most common method for making metal nanocrystals is solution-phase synthesis, especially in water, due to the high quality, large quantity, and high reproducibility that can be achieved.[15] Common synthetic protocol involves reducing a metal salt precursor to generate atomic species which can bond together with other atomic species to form nuclei, seeds, and nanocrystals. A combination of thermodynamics and kinetics determines how atoms are added to, and removed from, the surface of the growing nanocrystal to yield the final size and shape.[16] A large library of metallic nanocrystals can be synthesized with varying compositions and shapes. (Figure 1.1) Some of the many applications for metallic nanocrystals include cancer treatment, biomedicine, optics, and catalysis.

Nanocrystals are crystalline which means that the atoms are arranged in a repeating pattern in 3-Dimensional space. This crystal structure determines the positioning of atoms on the surface of the nanocrystal, and that is important because the organization of atoms on the surface of the nanocrystal can have a strong effect on growth behavior and properties. Metals such as gold, silver, platinum, and palladium have a face-centered-cubic crystal structure.[17] One basic face-centered-cubic unit cell is shown in Figure 1.2. From the basic structure, the pattern can be extended and repeated to form larger structures even up to bulk materials. Crystalline materials can be cut in defined directions to reveal facets. The 100 and 110 facets are shown in Figure 1.2. Making a nanocrystal completely emcompassed by specific facets can lead to different shapes. For example, a nanocrystal with only 100 facets will be a cube and only 110 facets will be a rhombic dodecahedron. Since the surface to volume ratio for nanocrystals is much higher than bulk materials, the surface facets play a large role in the behavior of the nanocrystal. Each type of facet has different surface energies and properties, so controlling the facets on nanocrystal is an active area of research.

In addition to growing nanocrystals to a desired shape from precursor species, nanocrystals can be etched from preformed shapes.[15] Similar to how a sculptor may remove material to make a masterpiece, etching can remove unwanted atoms or make entirely new shapes from pre-synthesized nanocrystals. In oxidative etching, oxidative species interact with atoms on the surface of the nanocrystal, removing electrons from the metal atoms, generating metal ions. These metal ions are solvated in solution, and the nanocrystal shrinks in size. Similar to nanocrystal growth, kinetic and thermodynamic factors play a role in which atoms are removed. By tuning the etching parameters, researchers have harnessed the power of oxidative etching to improve nanocrystal synthesis. Further development of the understanding and control of oxidative etching will provide more pathways to unique or energetically unfavorable nanocrystal shapes.

Metal nanocrystals are also a common material for liquid cell electron microscopy studies.

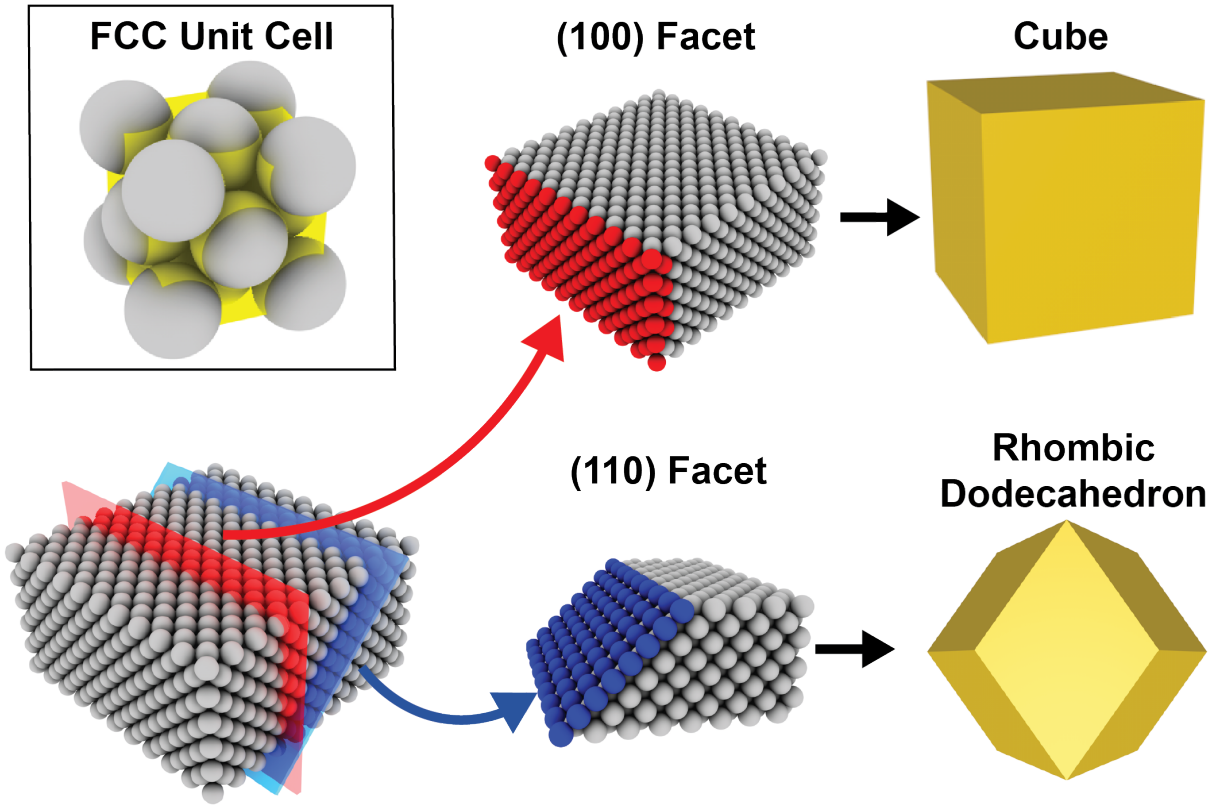

Figure 1.2: Metals such as gold, silver, platinum, and palladium have a face-centered-cubic crystal structure. Repeating the unit cell in 3-dimensional space yields nanocrystals and bulk materials. Slicing along defined directions leads to facets with specific atomic surface arrangements. Encompassing a nanocrystal in {100} facets leads to a nanocube and encompassing a nanocrystal in {110} facets leads to a rhombic dodecahedra.

Under electron beam irradiation, metal nanocrystals are fairly robust and do not degrade or undergo electron stimulated desorption. Further, metal nanocrystals are electron-dense, providing strong image contrast in the electron microscope. These advantages have made metal nanocrystals a desirable material for liquid cell electron microscopy method development, in addition to their many applications where watching metal structures on the nanoscale could be informative.

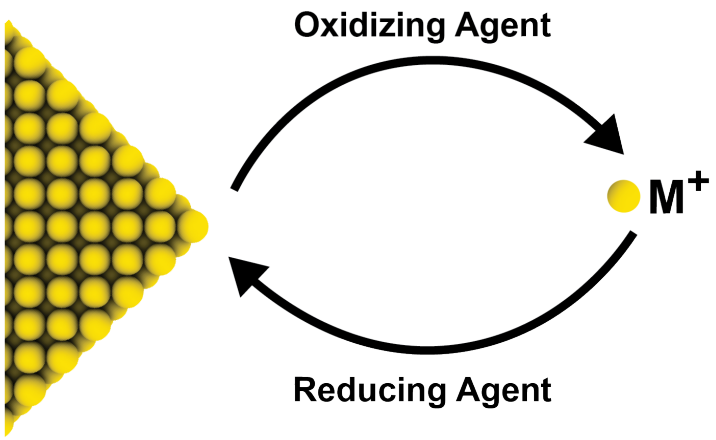

Figure 1.3: Schematic of oxidative etching and reductive growth of an FCC nanocrystal. If oxidizing agents are present, metal atoms on the surface will be converted to metal ions in solution. However, if reducing agents are in the solution, metal ions will be added to the surface of the growing nanocrystal as metal atoms.

1.2 Liquid Cell Electron Microscopy

Development of Liquid Cell Electron Microscopy

For imaging objects on length scales smaller than hundreds of nanometers, light microscopy lacks the necessary resolution due to its relatively large wavelength and the limitations of the diffraction limit. However, as first theorized by Louis de Broglie in 1925, electrons have wave-like character and their wavelength is smaller than individual atoms. Electrons at 200 keV, the energy used for this work, have a wavelength of about 3 pm. First demonstrated by Knoll and Ruska in 1932, the electron microscope has become a cornerstone of materials science due to its ability to image materials with high spatial resolution, including modern instruments regularly yielding high resolution images of atomic columns in a material. Since the invention of the electron microscope, many different modes including scattering electron microscopy (SEM), transmission electron microscopy (TEM), and scanning transmission electron microscopy (STEM) have been utilized in conjunction with advances in electron lenses, electron sources, cameras, and analytical equipment. For bright field TEM instruments (like the one utilized in this dissertation), an electron beam irradiates a sample, and electrons are scattered by the sample through attractions to the positive nuclei and repulsion by the atoms' electron clouds.[18] In a simplistic sense, the camera on the other side of the sample detects the unscattered electrons yielding an image of the sample. In nanomaterials research, electron microscopes are critical for visualizing the nanocrystals and their features such as facets and size.

Beyond simply charactizing synthesized nanocrystals (like in Figure 1.1), electron microscopy ideally would also enable observations of growth or dynamics of nanocrystals in their native liquid environment. Unfortunately, electron microscopy requires a high vacuum, so imaging a solution requires encapsulation with a rupture-resistant, electron beam-transparent material. Environmental TEM, or ETEM, is a recent advance that does allow gases near the sample while imaging, but ETEM still does not allow pressures that would be required for imaging liquid samples without evaporation. Early work in liquid cell electron microscopy attempted to use thin plastic windows to encapsulate and image liquid solutions.[19,20] In the early 2000s, Frances Ross and co-workers developed a liquid cell with silicon nitride windows for observing electrodeposition in the electron microscope.[21,22] The Alivisatos group began using silicon nitride to image individual colloidal nanocrystal growth trajectories in 2009.[23] To enhance the spatial resolution, the 2-D material of graphene was employed as the encapsulation material in 2012, enabling high resolution imaging in solution.[24] Further refinements and fabrication techniques have been developed in the years since, but the dominant encapsulation techniques for current liquid cell electron microscopy work are silicon nitride membranes (now commercially available with specifically designed holders and chips) and graphene. (Figure 1.4)

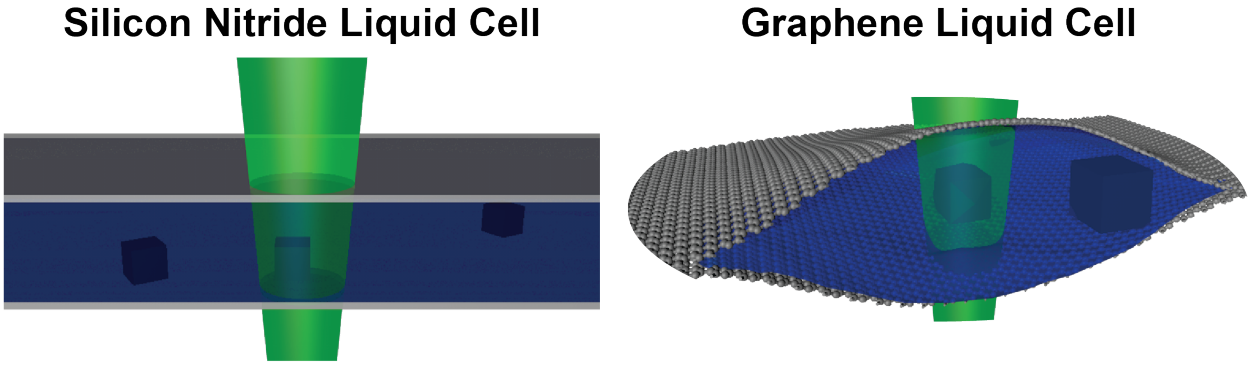

Figure 1.4: Schematics of the two most common encapsulation techniques for liquid cell electron microscopy. Silicon nitride membranes can be used to trap liquid using a specialized holder. Graphene liquid cells create small pockets of liquid sandwiched between graphene sheets.

Graphene liquid cells and commercial silicon nitride liquid cells have distinct advantages that allow researchers to choose the technique that best fits their experimental needs. (Table 1.1) Higher resolution can be achieved in the graphene liquid cell due to thinner windows and thinner liquid layers. Silicon nitride liquid cells have more controllable liquid heights with larger volumes of liquid and flow capabilities. The smaller amount of liquid in the graphene liquid cells has the benefit of not crashing the TEM vaccum if the encapsulation material ruptures during imaging. Commercial silicon nitride requires the purchase of a specialized

Topic	Commercial Silicon Nitride Liquid Cell	Graphene Liquid Cell
Spatial Resolution	Up to Nanometer Objects	Up to Atomic Resolution
Liquid Amount	Heights of 100s nm	Up to 100 nm
Electron Microscopy Holder	Specialized Holder Required	Tradition Holder Suitable
Window Cost	$40 for Top and Bottom Chip	$20 for 2 Graphene-Coated TEM Grids
Risk for Electron Microscope Vacuum	Membrane Rupture Crashes Column	Very Low Risk
Liquid Flow Capability	Yes	Not Currently
User Support	Customer Support from Liquid Cell Company	Graphene Liquid Cell Community

Table 1.1: Comparison of Silicon Nitride and Graphene Liquid Cells

holder and the recurring costs for top and bottoms chips. Graphene liquid cells can be used in traditional single-tilt holders and graphene-coated TEM grids for encapsulation cost about 50% of silicon nitride chips. However, depositing graphene on the TEM grids requires a few hours of fabrication time for every 10 grids. (See Chapter 2) Commercial silicon nitride liquid cells have a significant amount of customer support, whereas graphene liquid cell techniques are home-developed and technique expertise is spread mainly by word of mouth and trial-and-error. To mitigate some of the drawbacks of graphene liquid cells, some research groups are developing next-generation graphene liquid cells that include flow capabilities and reproducible pocket sizes.[25,26] For the work in this dissertation, traditional graphene liquid cells were utilized to provide greater resolution of facets and shape transformations.

Liquid cell electron microscopy has enabled the observation and study of many nanoscale processes. Previously unseen nanocrystal dynamics such as growth,[27–30] etching,[31,32] attachment,[24,33,34] assembly,[35–37] and other interactions have been imaged. Ultimately, liquid cell

electron microscopy should provide more than simply qualitative observations of nanoscale phenomena with quantitative information that can be related back to models and theories. Careful analysis of the electron microscopy videos is necessary to extract that quantitative data. Additionally, understanding and controlling the chemistry of the encapsulated liquid is critical to extending the learned mechanisms beyond the liquid cell.

Chemistry During Liquid Cell Electron Microscopy

Ideally, the probe of an imaging technique should not perturb the system it is investigating. Unfortunately, irradiating an aqueous solution of nanocrystals with 200 keV electrons causes beam-sample interactions. For example, silicon nitride liquid cells exhibit charging effects upon irradiation[38] although these effects can be mitigated by using a conductive window material such as graphene. The electron beam can and does change the chemical environment in all liquid cells. The electron beam induces radiolysis of the water solution, generating highly reactive radical species.[39–41] By understanding the species generated by the electron beam, the electron beam can harnessed as a controllable reactant that initiates desired chemical processes.

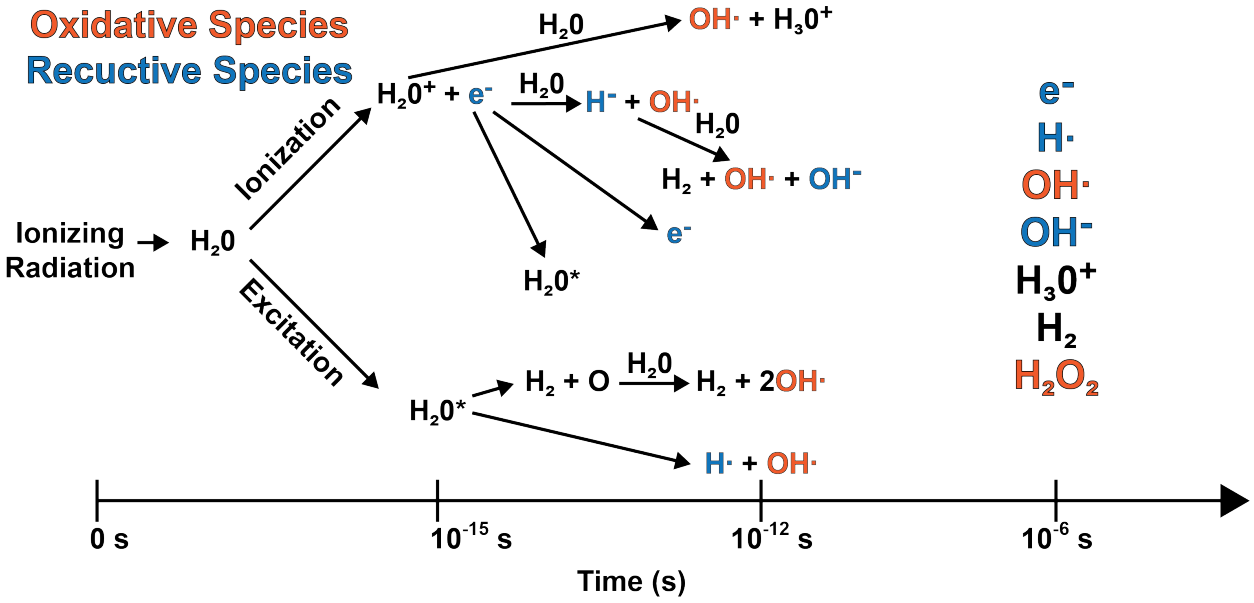

Figure 1.5: Upon irradiation of water, many highly reactive species are generated. Within microseconds, a steady-state is reached with hydrated electrons, hydrogen radicals, hydroxide radicals, hydrogen dioxide radicals, OH^-,H_3O^+, hydrogen gas, and hydrogen peroxide being the dominant species.

Radiolysis of pure water has been heavily studied by radiation chemists, and their extensive understanding is useful in determining the effect of the electron beam on the chemistry

of the liquid solution. Radiolysis of pure water generates a mixture of reactive species in fractions of a second, with the dominant species being hydrated electrons, hydrogen radicals, hydroxide radicals, hydrogen dioxide radicals, OH^-,H_3O^+, hydrogen gas, and hydrogen peroxide.[42] (Figure 1.5) The generation process can be broken down into 3 stages. The physical stage, which lasts for 10^{-15} s after irradiation, involves energy deposition from the electron beam into the water followed by fast relaxation. This process leads to the formation of excited water molecules, ionized water molecules (H_2O^+), and electrons. In the physico-chemical stage, lasting 10^{-15} to 10^{-12} s after irradiation, a variety of processes occur including ion-molecule reactions, dissociative relaxation, auto-ionization of excited states, hydration of electrons, and hole diffusion. Finally, during the chemical stage from roughly 10^{-12} to 10^{-6} s, the species react with each other and water molecules while diffusing around. When there is steady illumination, the concentration of species reaches a steady-state with all of the individual processes happening simultaneously. For pure water, the concentrations at steady state have been measured for a variety of radiation sources.

The solution in liquid cell electron microscopy experiments is rarely pure water, with common additives including metal nanoparticles, metal ions, surfactants, added oxidizing agents, added reducing agents, and pocket stabilizers. Therefore, knowledge acquired from the extensive work on irradiation of pure water is only helpful to an extent because it does not account for all of the interactions between radiolysis products and chemical additives. Unfortunately, the reactions between beam products and each of the chemical species in the liquid cell are far less studied. Direct measurement of the concentrations of species in the liquid cell is difficult with current instrumentation because the measurement would need to be made while irradiation is occurring for the small irradiation volume. Theoretical techniques to estimate the concentrations of species include kinetic simulations where the reaction rate constants for all of the studied reactions are used to determine the concentration over time of the species in solution using the initial concentrations loaded into the liquid cell and the beam conditions.[43,44] Additional species, such as HCl, can be added to these models to provide insight into the time until steady state, concentrations at steady state, and effects of changing initial concentrations or electron beam dose rate. (Figure 1.6) The drawback to kinetic simulations is that missing a single possible reaction could drastically change the complex steady state that is reached. Since not all the reactions between added species and reactive radiolysis radicals (or even the graphene itself![45]) are known, it is not currently possible to accurately model the chemistry of the liquid cell through kinetic simulations. However, kinetic models can provide broad insight into the chemical trends in a liquid cell, and better modeling techniques for the liquid cell environments is an area of active research.

Electron beam effects on the chemistry of liquid cell electron microscopy experiments is not hopeless, for if the chemistry can be understood and controlled, the electron beam can stimulate a desired chemical processes. Often, reaction initiators are needed for dynamic processes, especially in the graphene liquid cell which lacks the ability to bring in new chemical species. The electron beam has the potential to be that reaction initiator. In this dissertation, nanocrystal dynamics will be explored to elucidate non-equilibrium shape transformations, and the nanocrystal dynamics will also be used as an indirect probe of

the chemical environment in liquid cell electron microscopy experiments. Through a better understanding of the chemical environment in liquid cell electron microscopy, future material science experiments will be more systematic and reproducible.

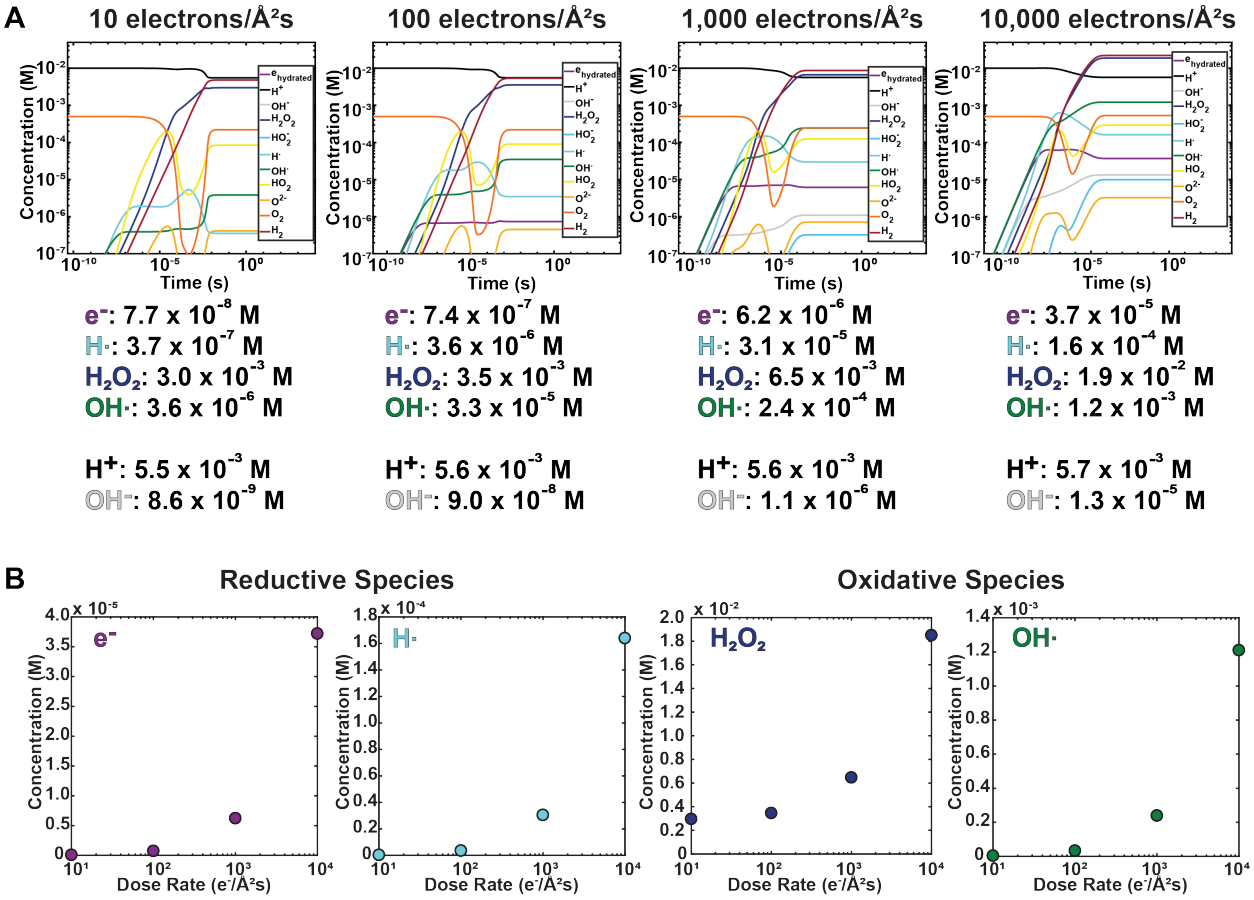

Figure 1.6: Kinetic simulations can be used to estimate the concentrations of species in aqueous solutions under electron beam illumination.[43] These simulations were done at the TEM conditions used in this dissertation with an aqueous HCl solution. A) Concentration of major species over time at different electron beam dose rates. Note that steady-state is reached within a millisecond of irradiation. B) Concentrations of reductive and oxidative species at different dose rates.

Chapter 2

Graphene Liquid Cell Fabrication

Making graphene liquid cells for electron microscopy imaging can be challenging for new researchers to the field. While the technique does not require an excessive or time consuming amount of steps, successful graphene liquid cells do require careful hand control and patience. The following protocol has been published in a video journal, and it is highly recommended that new researchers to the field watch that demonstration of the technique to acclimate themselves to the technique.[46]

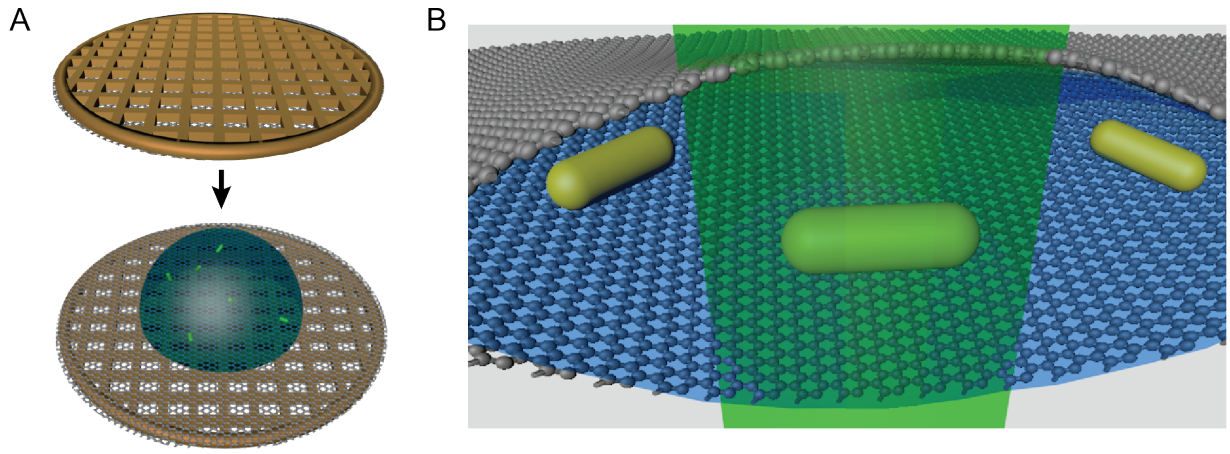

Figure 2.1: Schematic of the graphene liquid cell. A) Two graphene-coated TEM grids make a sandwich around a liquid droplet of the desired encapsulation solution. B) Schematic of a graphane liquid cell pocket with nanorods being imaged by the electron microscope.

2.1 Making Graphene-Coated TEM Grids

A roughly 2 cm^2 piece of premade graphene-on-copper (ACS Materials, 3-5 layer graphene) is cut out. Higher success rates of liquid cell formation were achieved with 3-5 layer graphene, and there is minimal loss of resolution while imaging in the TEM. The graphene-on-copper piece is washed three times in acetone at 50 degrees celsius for 5 minutes to dissolve any leftover PMMA from the protective layer deposited by the supplier. (Figure 2.2A) After drying, macroscopic wrinkles in the graphene-on-copper piece are pushed out by gently pressing between two glass slides. (Figure 2.2B) Holey amorphous carbon support, quantifoil gold TEM grids (SPI Supplies, 300 Mesh Gold, R1.2/R1.3) are placed on the graphene with the carbon side in contact with the graphene. (Figure 2.2C) A couple drops of isopropanol are placed on the grids and let dry for more than 2 hours. Then, the graphene-on-copper sheet with the TEM grids is placed on a sodium persulfate solution (1 g/10 mL deionized water) to etch off the copper. (Figure 2.2D) After the copper is etched away, the graphene-coated grids are carefully rinsed with deionized water.

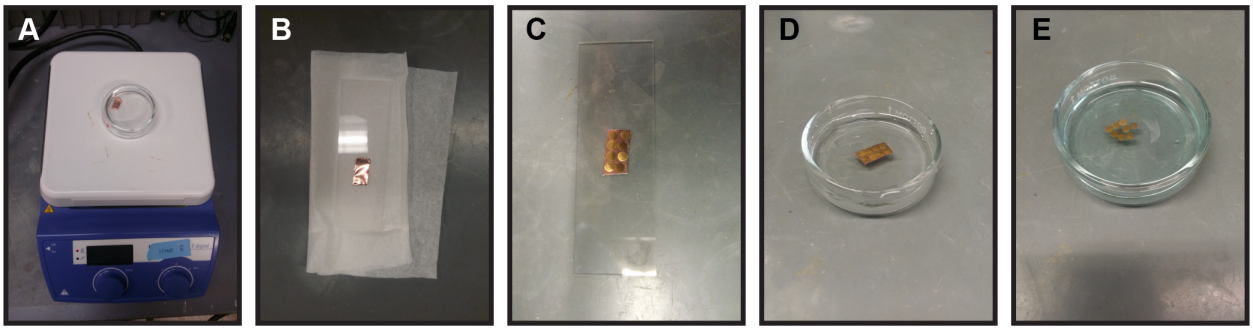

Figure 2.2: Making graphene-coated TEM grids A) Wash graphene-on-copper piece in warm acetone to remove residual PMMA. B) Smooth out macroscopic wrinkles in graphene-on-copper piece. C) Place holey amorphous carbon-gold quantifoil TEM grids on the graphene sheet with the graphene in contact with the amorphous carbon. D) Float the graphene-on-copper sheet with the TEM grids on a sodium persulfate solution. E) After the copper has etched, rinse the graphene-coated grids with water.

2.2 Making Liquid Cell Pockets

Two graphene-coated TEM grids are placed on a glass slide with the graphene side facing upwards. A corner is cut off of one of the graphene-coated TEM grids. (Figure 2.3A) A droplet of less than 0.5 μL of solution is placed on the non-cut graphene-coated TEM grid. (Figure 2.3B) It is important to deposit as small a droplet as possible and place it in the center of the grid. Carefully place the graphene-coated TEM grid with the cut corner on top

of the droplet without squeezing out any of the liquid. (Figure 2.3C) This is the hardest step in the fabrication process and requires careful control of the tweezers. Wait 5 minutes and look for liquid leakage out of the graphene liquid cell. The sample is now ready for imaging in the electron microscope.

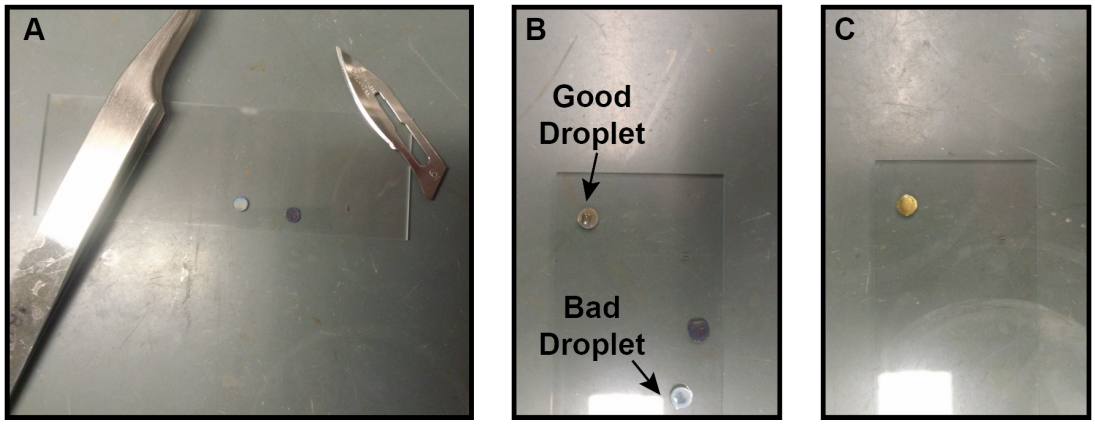

Figure 2.3: Making graphene liquid cell pockets A) Cut off a corner of one graphene-coated TEM grid. B) Place a small droplet of the solution of interest on the uncut graphene-coated TEM grid. C) Place the graphene-coated TEM grid with the cut corner carefully on top of the droplet, forming a graphene liquid cell.

2.3 Imaging the Graphene Liquid Cell in the TEM

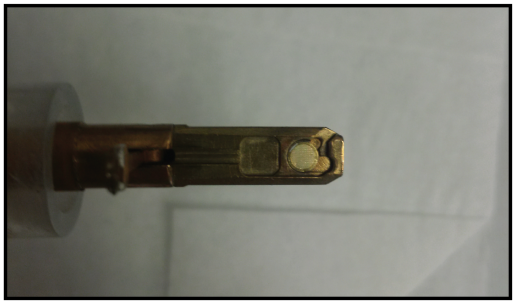

Figure 2.4: The graphene liquid cell is placed in the TEM holder in exactly the same way as a normal TEM grid.

The graphene liquid cell is placed in a traditional TEM single tilt holder (Figure 2.4) and loaded into the TEM column. It is not necessary to rigorously check for leaks because the graphene liquid cell encapsulates such a small amount of liquid that would be unable to crash the TEM column. The nanoparticles and amorphous carbon background are used to properly align the TEM beam and focus the image. Then, the sample is removed from the beam path to calibrate the electron beam dose rate.

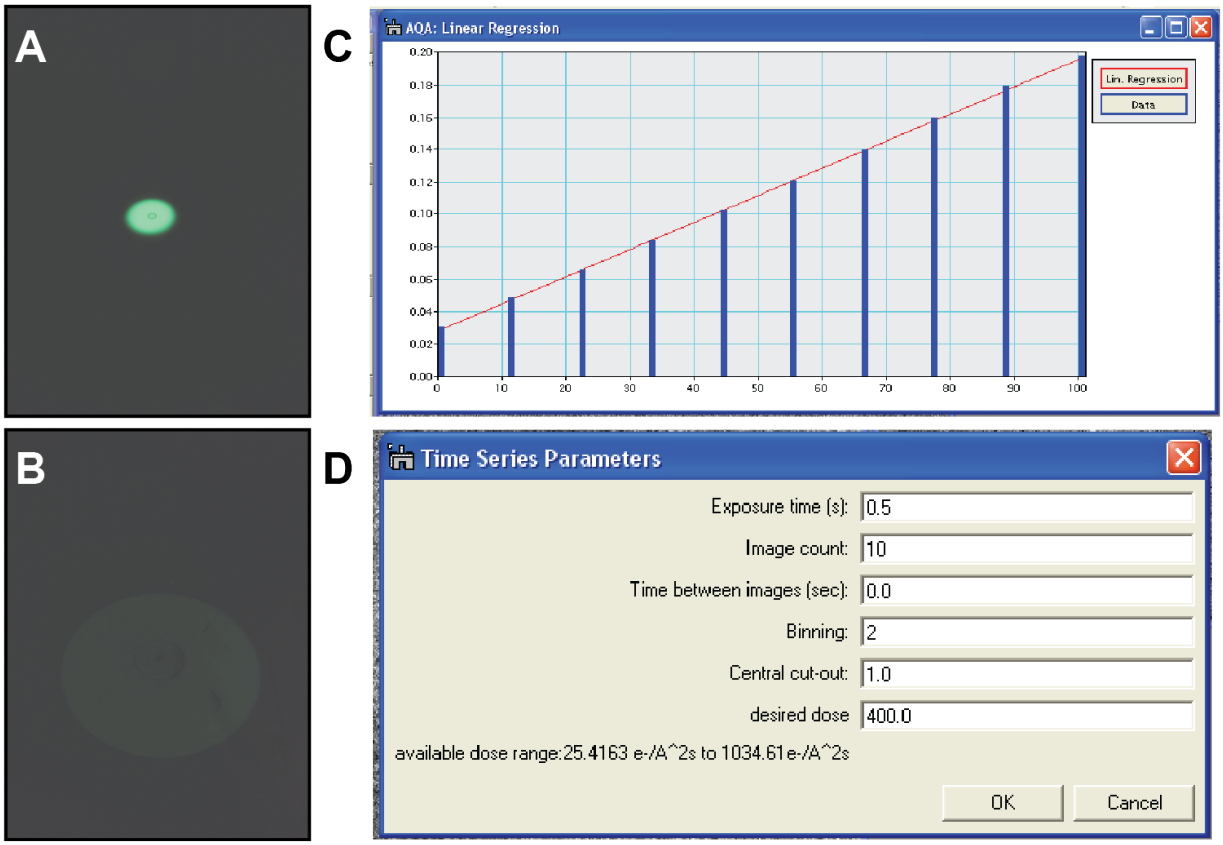

Figure 2.5: Calibrating the electron beam dose rate. A) Condensed electron beam for dose calibration viewed using the fluorescent screen. B) Expanded electron beam for dose calibration viewed using the fluorescent screen. C) Calibration curve relating electron beam dose rate to the consenser lens current. D) Prompts for collecting TEM videos using calibration script.

After the TEM filament has been on for at least 20 minutes to stabilize, the electron beam dose rate calibration script is initiated. First, the electron beam is condensed to the most condensed amount, highest dose rate, needed for the experiments, while reading out and saving the C2 lens current for the condensed electron beam. (Figure 2.5A) Then the electron beam is expanded to the most spread amount, lowest dose rate, needed for the

experiments, and that C2 lens current is saved for the spread electron beam. (Figure 2.5B) Images are collected in the range between the most condensed and most spread dose rates. The CCD counts on the camera can be converted to dose rate using the CCD sensitivity. Finally, a calibration curve can be created to convert between desired electron beam dose rates and C2 lens current. (Figure 2.5C)

The sample is re-inserted into the electron beam path, and the researcher searches for nanoparticles at a low dose rate. (roughly 40 $e^-/Å^2s$ or less) When a nanocrystal of interest is found, the focus is fine-tuned while maintaining a low dose rate. Then, the calibration curve is used to set the condenser lens current to the desired dose rate, and collection of a time series of TEM images is initiated. (Figure 2.6) Metadata of dose rate and time are embedded in the files. After the nanocrystal has finished its dynamics, the beam is spread and new nanocrystals of interest are found. This process can be repeated for as many nanocrystal trajectories as are needed.

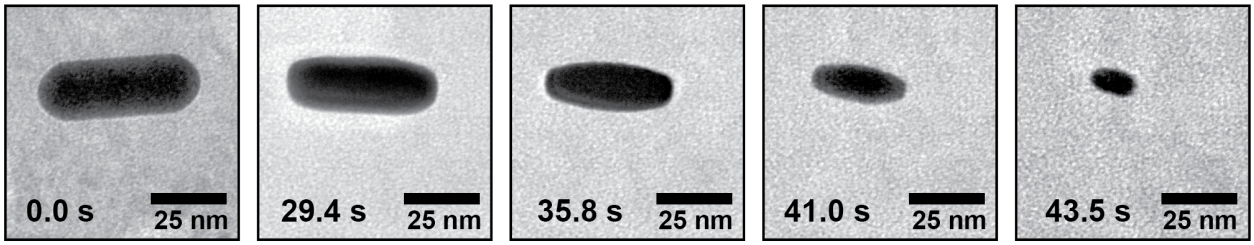

Figure 2.6: Example time series of a nanorod etching in a graphene liquid cell.

2.4 Considerations for Making Graphene Liquid Cells

As mentioned previously, the fabrication of graphene liquid cells can be challenging, and even experienced graphene liquid cell users do not have perfect success rates for encapsulating liquid. Each liquid system has to optimized and tuned through the ionic strength of the liquid to yield proper encapsulation, and even suitable systems with experienced users only have around 50% success rates. The best way to check if the liquid is properly sealed in the graphene liquid cell is by looking for rapid bubble movement in the electron microscope. Sometimes, no liquid is encapsulated or the pocket dries while imaging, leading to a gel-like sample with a high concentration of salt and surfactant. Distinguishing between the gel-like material and actual liquid is relatively easy due to the difference in bubble movement and imaging contrast between the two environments. Results from the gel-like sample are not usable for drawing conclusions about colloidal chemistry.

Most common sources of error occur during tha making of the graphene-coated grids and the assembly of the liquid cell pockets. Direct transfer graphene is needed for the graphene liquid cell because the graphene sheets need to be clean to form a hermetic seal through

Van der Waals forces. Making graphene-coated grids through polymer transfer methods may lead to lower success rates of liquid encapsulation. Handling the graphene-coated grids carefully is also important because any bending or creasing of the grids may lead to cracks in graphene or lack of contact between the two grids during encapsulation. The critical step in making the grids involves the deposition of a small droplet of liquid on the grid and placing the second grid on top. The droplet should be as small as possible (less than 0.5 μL) and be centered on the grid. Occasionally, the tweezers will get stuck between the two grids if the user is not quick enough in laying the second grid down. Practice is important for the fabrication, so we recommend first practicing using traditional copper, amorphous carbon TEM grids before moving on to the more expensive graphene-coated gold grids. With sufficient practice and care, graphene liquid cells can be a reliable technique for observing nanoscale phenomena in their native liquid environments.

Chapter 3

Effect of Driving Force on Oxidative Etching

Etching of nanocrystals is a valuable method for removing unwanted atoms or accessing unique shapes, so unraveling the mechanisms of etching is important. Through systematic graphene liquid cell experiments and careful image analysis, trajectories of nanocyrstals were observed and the facets for each point in the trajectory were measured. The initial $FeCl_3$ concentration was determined to control chemical potential during the etching process. By combining the facet trajectories with Monte Carlo simulations, the mechanisms of etching at high driving forces were elucidated, and methods for synthesizing nanocrystals with energetically unfavorable, high-index facets were proposed.

3.1 Nonequilibrium Etching of Cubes and Rhombic Dodecahedra

Etching gold nanocubes and nano-rhombic dodecahedra in a high-driving-force regime leads to non-equilibrium intermediate tetrahexahedra shapes.[47] High-driving-force etching in a simplified sense occurs when the etching is at a high enough rate that kinetics determine which atoms are being removed instead of thermodynamics. In these situations, the etching nanocrystal transforms to a kinetically stable shape instead of its equilibrium shape. An equilibrium nanocrystal shape is the lowest energy geometry based on the energies and amount of surface area for each individual facet. The absolute lowest energy for a nanocrystal is the Wulff Construction, but usually the nanocrystals can remain stable in local energetic minimums using surface ligands. Cubes and rhombic dodecahedra have {100} and {110} facets respectively, and these facets are both lower in energy than the {hk0} facets of the tetrahexahedra.

The relationship between the surface facets can be visualized by looking at their atomic surfaces, and this relationship explains why both cubes and rhombic dodecahedra can transition to tetrahexahedra intermediate shapes. Starting with a perfect cube of a material with

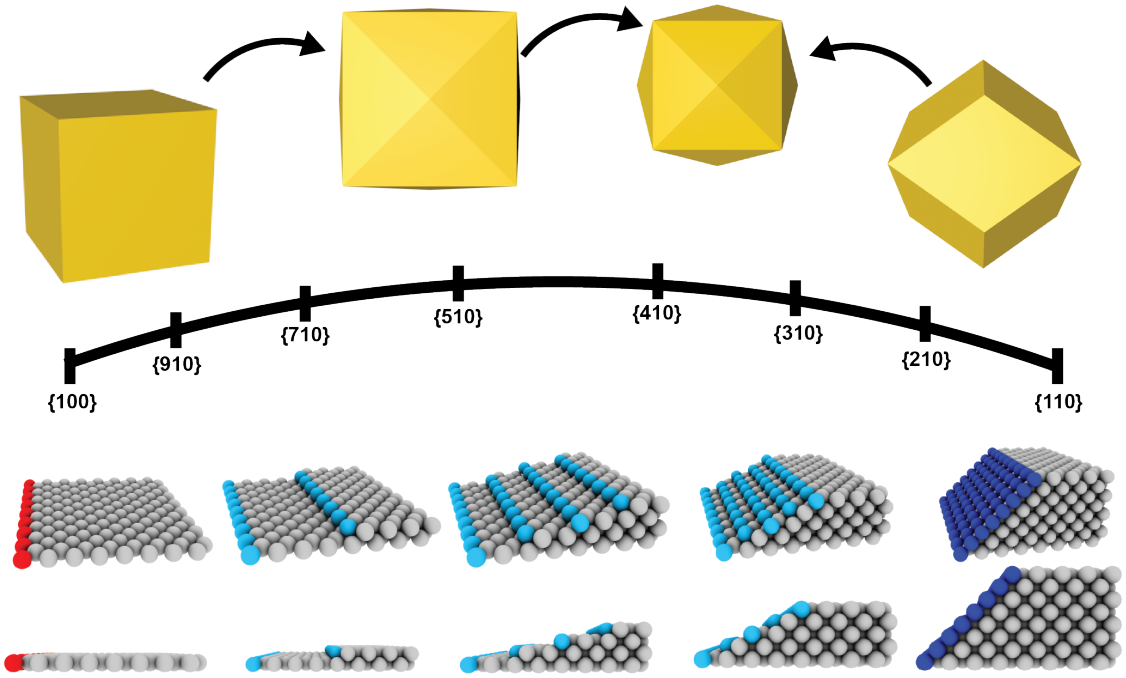

Figure 3.1: Cubes with {100} facets, tetrahexahedra with {hk0} facets, and rhombic dodecahedra with {110} facets can be interconverted by increasing and decreasing the number of step edges on the surface. Schematics of the atomic surface of each facet is shown with the corresponding nanocrystal shape that is produced by covering the entire surface in that facet.

face-centered-cubic crystal structure, which is encompassed by 6 (100) facets, the surface is atomically smooth with no step edges on the face. (Figure 3.1) If a step edge is added every 8^{th} atom, then the surface would look like the second surface from the left in Figure 3.1. Covering an entire nanocrystal in the 810 facet would yield the tetrahexahedral shape shown above. The tetrahexahedral shape is similar to the cube but each face of the cube has a stepped surface on it with a slope corresponding to the {hk0} facets. As the facets go to lower h/k values for the {hk0} facets, the number of step edges on the surface increase with each terrace between steps becoming shorter and leading to steeper facets on the nanocrystal. At the limit where each terrace is only one atom wide, the facets are {110} and the shape is the rhombic dodecahedron. By increasing and decreasing the width of the terrace between atomic steps on the surface of the nanocrystal, the nanocrystal can transition between the cubic, tetrahexahedral, and rhombic dodecahedral geometries.

These shape and facet changes can be imaged during etching using graphene liquid cell

electron microscopy. Since the size of the nanocrystals is similar to the thickness of the pocket, the preformed nanocubes and nano-rhombic dodecahedra orient themselves with their initial flat facet parallel to the graphene. The nanocrystals do not move translationally or rotationally during imaging due to the well-documented slow diffusion in graphene liquid cells and the large size of the nanocrystals. By adding $FeCl_3$ to the aqueous solution of gold nanocrystals, the nanocrystals will start etching upon electron beam irradiation at high enough dose rates. The combination of $FeCl_3$ and the oxidative species generated by the radiolysis of water etches the nanocrystals. (See Chapter 4 for more in-depth information about the chemistry of the etching process in the liquid cell.) Recording TEM videos of the nanocrystals during the etching process provides 2D images that can be converted to 3D shape trajectories. (See Appendix A.3 for information on how the 2D image was converted to a 3D shape.) Etching cubes in this high-driving-force regime reveals intermediate tetrahexahedra with measurable {hk0} facets. (Figure 3.2B) Similarly, etching rhombic dodecahedra at a high-driving-force yields a shape transformation to a tetrahexahedral intermediate, although the tetrahexahedral intermediate is rotated from the cube's intermediate shape because the initial crystals are on a different zone axis. (Figure 3.2D) With the ability to follow individual etching trajectories, factors in the etching process such as the $FeCl_3$ concentration can be investigated to provide insight into the mechanism of high-driving-force etching.

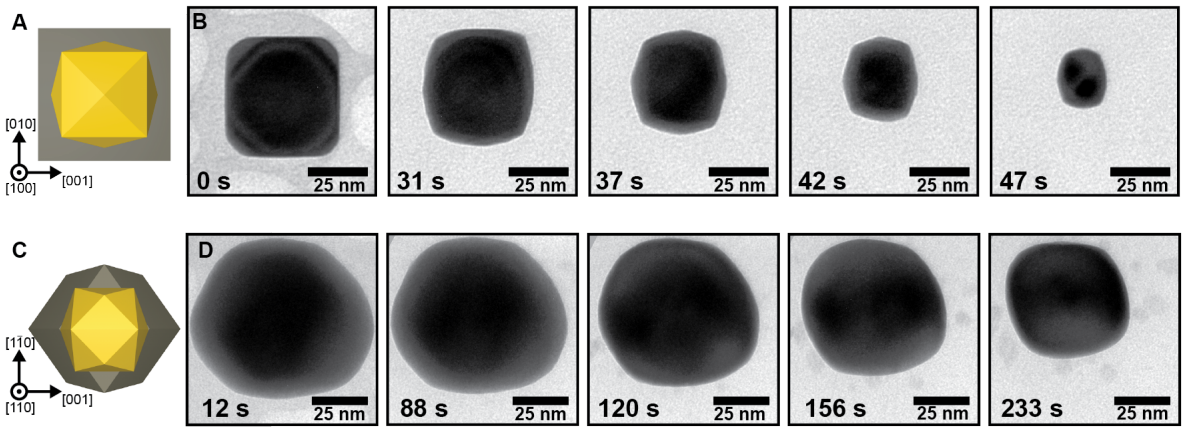

Figure 3.2: Representative images from etching gold cubes and rhombic dodecahedra. A) Orientation of cube and intermediate tetrahexahedra B) Images from an etching gold cube at a dose rate of 800 $e^-/Å^2s$. C) Orientation of rhombic dodecahedra and intermediate tetrahexahedra D) Images from an etching rhombic dodecahedra at a dose rate of 800 $e^-/Å^2s$. The etching time is significantly longer than for the cube because the initial rhombic dodecahedron was much larger.

3.2 Effect of Potential on Cube Etching

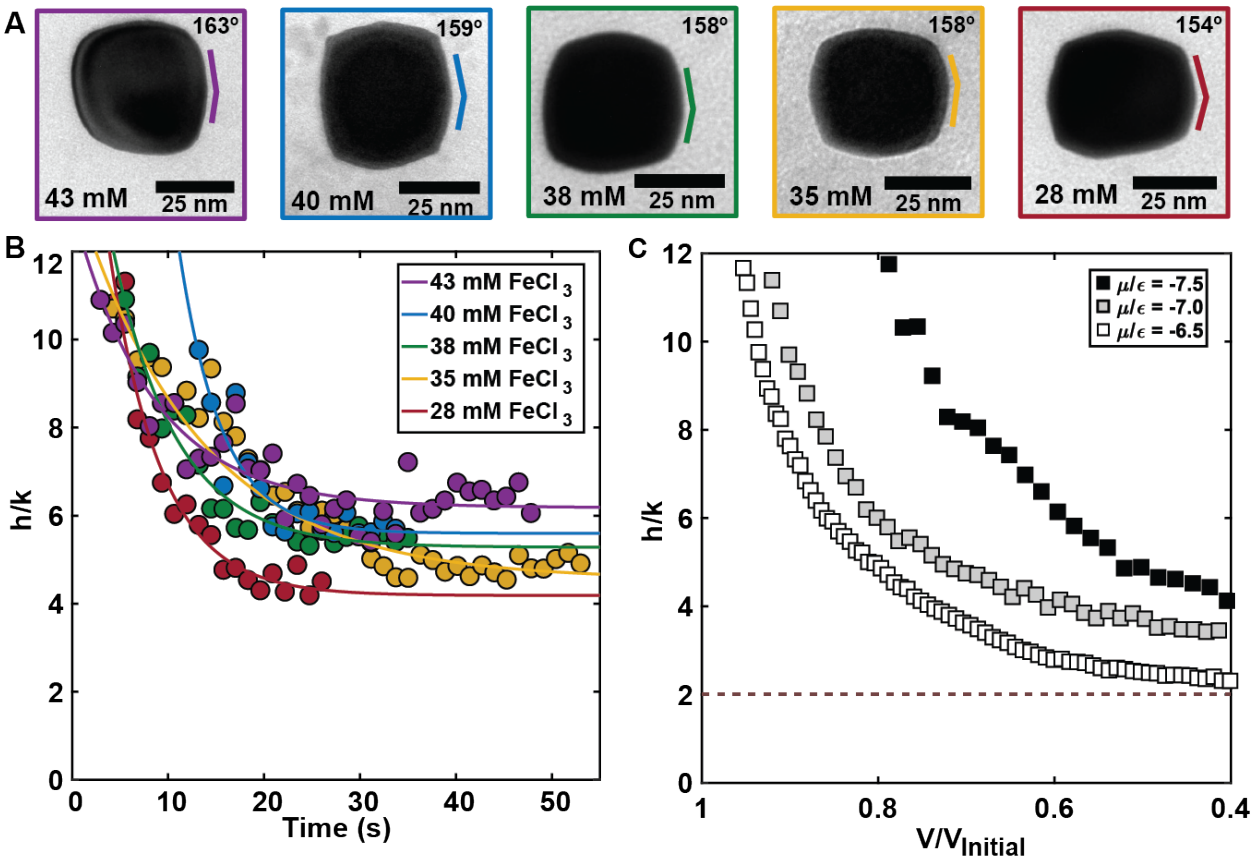

Figure 3.3: The facet trajectories of etching gold nanocubes can be tracked for different initial concentrations of $FeCl_3$. A) Representative intermediate tetrahexahedra at different initial $FeCl_3$ concentrations. B) Representative facet trajectories of nanocubes in the graphene liquid cell. All the trajectories reach a steady {hk0} facet, but the facet is different depending upon the initial $FeCl_3$ concentration. Fits are guides to the eye. C) Monte Carlo simulations show similar facet trajectories when changing the potential. Colors are consistent across panels A and B.

By following the etching facet trajectories at a variety of initial $FeCl_3$ concentrations, the effect of $FeCl_3$ and the underlying mechanisms of high-driving-force etching can be elucidated. The exact concentration of $FeCl_3$ in the liquid cell during etching is not possible to measure; however, the trends in initial concentrations of $FeCl_3$ in the pre-made solution before encapsulation should match the concentrations in the liquid cell because any drying or other effects should be constant between liquid cells. To plot the trajectories of the facets on the nanocubes, the h/k value of the {hk0} facet was calculated. Initially, the h/k value is

infinitely high because cubes have {100} surface facets. As etching progresses and the cubes transform to tetrahexahedra, the h/k value of the facets decreases rapidly before reaching a steady facet. The steady {hk0} facet remains constant despite the volume continuing to decrease at a constant rate. As the initial $FeCl_3$ concentration was modulated, the facet trajectories were similar except for the value of the steady facet. At greater concentrations of $FeCl_3$, the steady facets had a greater h/k value. (Figure 3.3) Collecting multiple individual etching trajectories at each $FeCl_3$ concentration showed a consistent pattern of higher $FeCl_3$ concentration leading to greater h/k value of the steady {hk0} facet. (Figure 3.4)

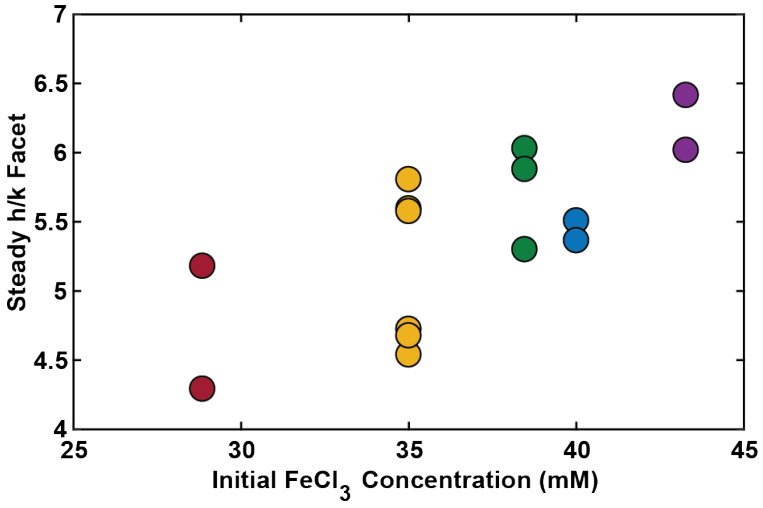

Figure 3.4: Steady facet for etched gold nanocubes at different initial concentrations of $FeCl_3$. Colors are consistent with Figure 3.3

Monte Carlo simulations using a simplified, lattice-gas-like model to remove atoms from a face-centered-cubic nanocube were used to understand the $FeCl_3$ dependence of the steady facet. In the simulations, the probability of removing a surface atom was dependent on its number of nearest neighbor bonds (each contributing an energy ϵ) and the driving force of the etching, μ. For example, at a chemical potential of μ/ϵ = -6.5, atoms with 6 or less nearest neighbor bonds are likely to be removed while atoms with 7 or more nearest neighbor bonds are unlikely to be removed. Using this method for removing atoms, the facet trajectories of etching nanocubes follow an exponential-like curve that qualitatively matches the experimental graphene liquid cell TEM trajectories. (Figure 3.3) At lower potentials, the Monte Carlo simulations go to lower steady h/k facets while higher potentials lead to higher h/k steady facets. The corroboration between the Monte Carlo simulations and the experimental data suggests that in the high-driving-force etching regime, coordination number of the surface atoms determines which atoms can be removed. Further, the concentration of $FeCl_3$ seems to be controlling the etchant potential, and the etchant potential is controlling the intermediate facets when etching from the {100} nanocubes.

3.3 Effect of Potential on Rhombic Dodecahedra Etching

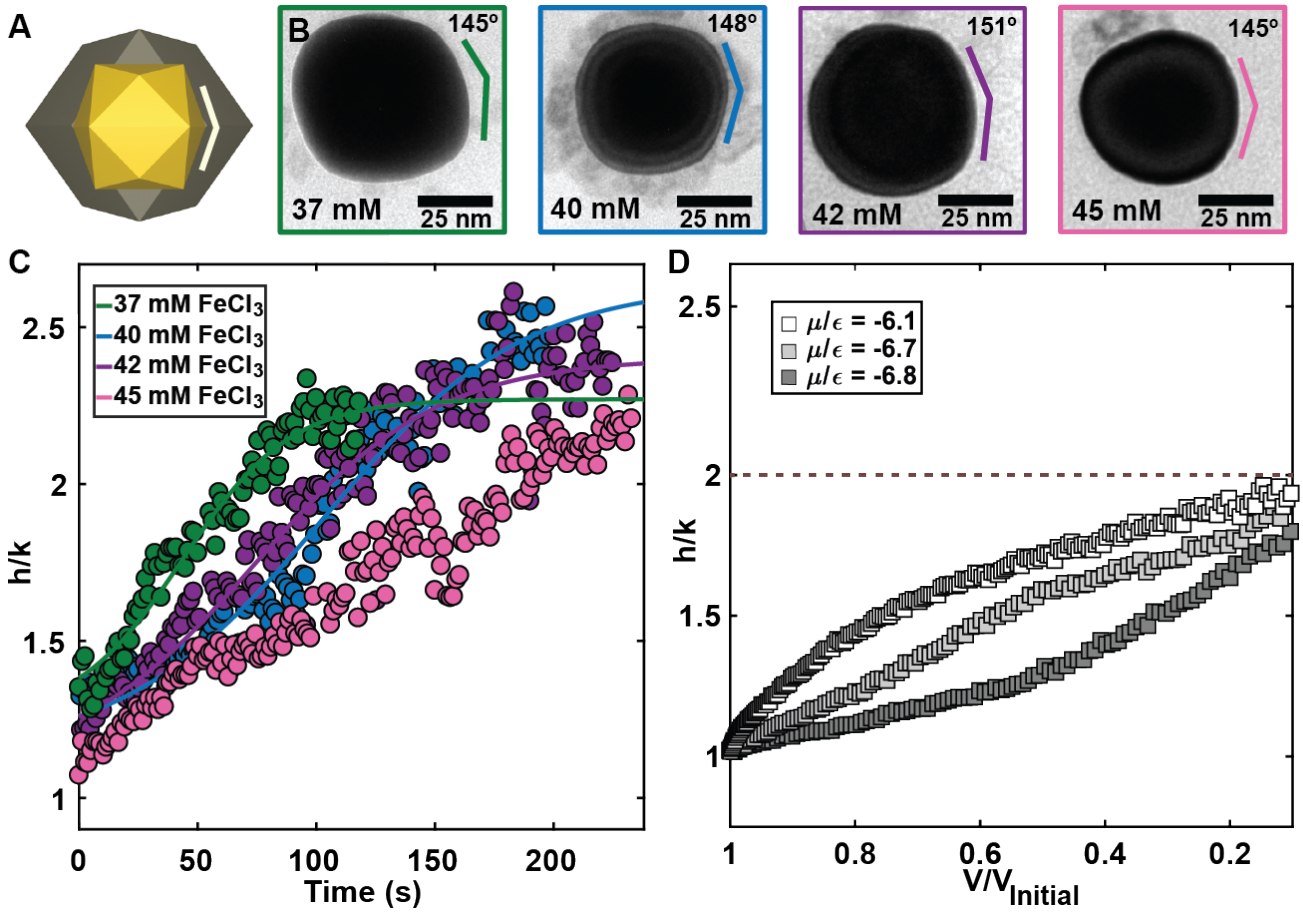

Figure 3.5: The facet trajectories of etching gold rhombic dodecahedra can be tracked for different initial concentrations of $FeCl_3$. A) Orientation of the intermediate tetrahexahdra relative to the initial rhombic dodecahedra. Notice that they are rotated from the tetrahexahedra formed from cubes. B) Representative intermediate tetrahexahedral shapes from rhombic dodecahedra at different initial $FeCl_3$ concentrations. C) Representative facet trajectories of rhombic dodecahedra in the graphene liquid cell. Although the trajectories are different, all the etching rhombic dodecahedra reach the same steady {hk0} facet independent of the initial $FeCl_3$ concentration. Fits are guides to the eye. D) Monte Carlo simulations show similar facet trajectories when changing the potential. Colors are consistent across panels B and C.

Etching from the opposite side of the {hk0} family, the {110} rhombic dodecahedra, pro-

vides further information about how the $FeCl_3$ concentration and etchant potential affect the process of atom removal. Similar to the nanocubes, the rhombic dodecahedra were etched at different initial $FeCl_3$ concentrations in the graphene liquid cell and the facet trajectories were followed. The intermediate tetrahexahedra were rotated from the nanocubes' intermediate tetrahexahdra because the rhombic dodecahedra and cubes align along different facets in the liquid cell. Etching of rhombic dodecahedra takes longer because the nanocrystals are significantly larger than the nanocubes. For the etching of the rhombic dodecahedra at different initial $FeCl_3$ concentrations, the facet trajectories are different but the final steady {hk0} facet is always between h/k = 2 and h/k = 2.5. (Figure 3.5) The curvature of the facet trajectory changes from concave down to concave up as the initial concentration of the $FeCl_3$ increases. Collecting multiple etching trajectories of individual rhombic dodecahedra at different initial $FeCl_3$ concentrations yields consistent {hk0} steady facets with h/k around 2.5, which is markedly dissimilar from the $FeCl_3$ dependence seen in the etching nanocubes.

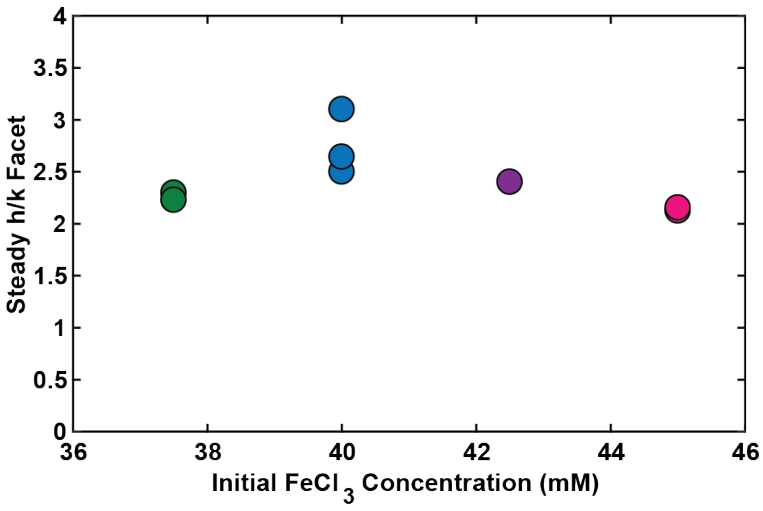

Figure 3.6: Steady facet for etched gold rhombic dodecahdedra at different initial concentrations of $FeCl_3$. Colors are consistent with Figure 3.5

Monte Carlo simulations can again be utilized to investigate the effect of chemical potential on the facet trajectories of rhombic dodecahedra. At potentials μ/ϵ between 6 and 7, the rhombic dodecahedra transform to intermediate tetrahexahedra. Remarkably,the Monte Carlo simulation trajectories match qualitatively with the experimental facet trajectories, following different paths to the same {210} intermediate facet. (Figure 3.5D) At higher potentials the Monte Carlo curve is concave up and lower potentials show a concave down trajectory. Since the Monte Carlo simulations match extremely well with the *in situ* experimental etching of cubes and rhombic dodecahedra, closer examination of the simulations can be used to explain the observed difference in potential dependence.

3.4 Atomic Modeling of Potential Dependence Difference

Investigating how the Monte Carlo simulations work on an atomic level provides insight into the mechanisms of etching in the high-driving-force regime. The Monte Carlo simulations can be visualized using a zero temperature, atomic ball model. In this model, each atom is color-coded by its number of nearest-neighbor bonds. Then, in each step of the model, atoms are removed if they have fewer bonds than the potential. This kinetic model represents what would happen at zero temperature where the removal of atoms is deterministic instead of probabilistic. By progressing through the steps of this model, it is easier to understand how the intermediate facets are formed.

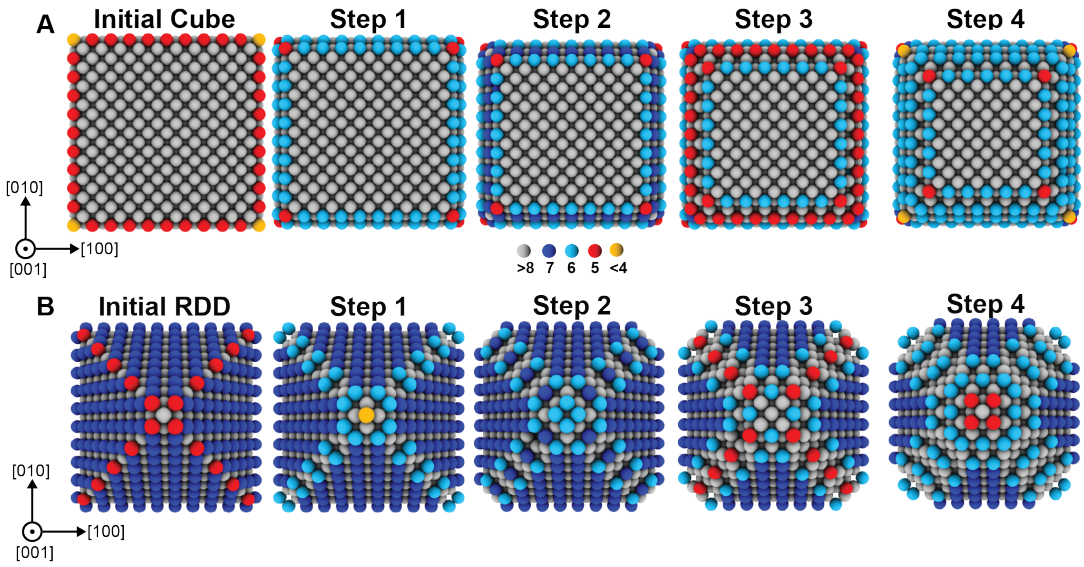

Figure 3.7: Zero temperature kinetic ball model of the etching process. Each atom is color-coded by its number of nearest neighbor bonds. Atoms are removed each step if they have less than 6.5 nearest neighbor bonds. A) Etching of a perfect nanocube. B) Etching of a perfect rhombic dodecahedron.

For the perfect nanocube, the atoms on the surface facets are 8-coordinate with 5-coordinate edge atoms. (Figure 3.7A) At a potential between 6 and 7.5, etching begins at the edges. As atoms are removed through progressive steps in the model at a potential of 6.5, {210} ledges begin to emerge. Continuing to remove atoms following this protocol leads to a tetrahexahedron with {210} facets, exactly what was shown through the Monte Carlo simulation in Figure 3.3C. Although the zero temperature kinetic model ignores unlikely fluctuations that are captured in the Monte Carlo simulation and likely happen during

experimental etching, the zero temperature model helps visualize the etching process making for easier comparisons between cubes and rhombic dodecahedra.

For the perfect rhombic dodecahedra, the surface atoms are 7-coordinate with 5-coordinate edge atoms. (Figure 3.7B) At potentials above 7, all of the surface atoms are able to be removed, so the shape would stay a rhombic dodecahedron with {110} facets. At potentials below 6, no atoms would be removed after Step 2, so no etching would occur except for probabilistically unlikely events. At a potential between 6 and 7, atoms are removed from the edges in a progressive fashion that leads to {210} surface facets and a tetrahexahedral intermediate shape. This predicted {210} surface facet from the zero temperature kinetic model matches the Monte Carlo simulations shown in Figure 3.5D. With the evidence that the zero temperature kinetic models recreate the behavior seen in the Monte Carlo simulations and the graphene liquid cell experiments, the effect of potential on the atomic level can be investigated.

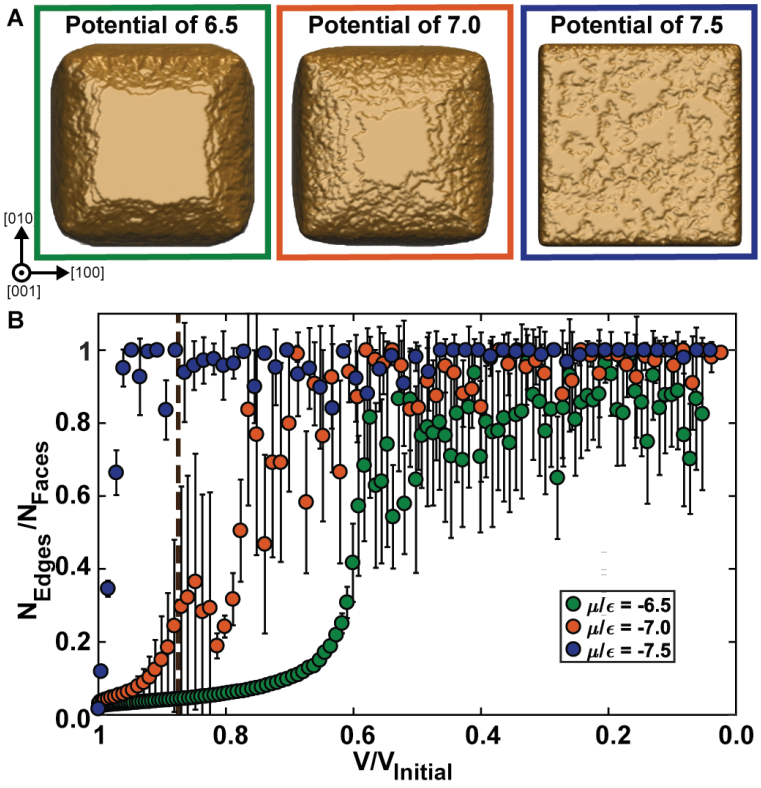

Figure 3.8: At higher potentials, the edges become rougher on the etching nanocubes. A) Representative images from Monte Carlo simulations of etching nanocubes showing the roughness of the top layers of atoms. B) Quantifying the roughness of the edge at different potentials by measuring the ratio of edge atoms to surface atoms. The brown dotted line is the time for the images in panel A.

Investigating the results of the Monte Carlo simulations for etching nanocubes reveals a roughening of the edges of the top layers of atoms at higher chemical potentials. Images from intermediate stages of the etching process show the surface of the etching nanocrystal. (Figure 3.8A) At a potential of 6.5, the top layer of atoms forms an almost uniform square shape, but increasing the potential to 7.0 causes the top layer of atoms to adopt a more irregular shape. Further increasing the potential to 7.5 leads to a top layer of atoms with no defined boundary. This roughening of the top layer edges was quantified by calculating the ratio of edge atoms to surface atoms. (Figure 3.8B) Higher potentials lead to more roughening of the edges causing a greater ratio of edge atoms to surface atoms.

The atomic zero temperature models can help explain why higher potentials cause roughening and why the roughening leads to {hk0} facets with greater h/k values. For the etching cube, removing a 6-coordinate edge atom from the top layer reveals two 7-coordinate interior atoms. (Figure 3.9A) At chemical potentials less than 7, the interior atoms would not be removed and etching would continue removing the 6-coordinate atoms around the edge. This would lead to smooth edges and perfect {210} facets on the intermediate tetrahexehedron. At potentials greater than 7, the inner 7-coordinate atoms are removed. Removing inner atoms on the surface leads to etching into the top layers of atoms causing a rough edge on the surface layers. The ability to remove inner atoms leads to flatter facets and higher h/k values on the {hk0} facets of the intermediate nanocrystal. Changing the chemical potential when etching nanocubes modulates the ratio of removing edge atoms verses interior atoms, thereby changing the resulting morphology of the intermediate shape.

The rhombic dodecahedra did not show a chemical potential dependence in the graphene liquid cell experiments nor the Monte Carlo simulations, and the zero temperature atomic ball model can also explain this behavior. Removing a 6-coordinate edge atom on the rhombic dodecahedra reveals a new 6-coordinate interior atom. (Figure 3.9B) Changing the chemical potential does not change the likelihood of removing edge atoms verses interior surface atoms because they have the same number of nearest neighbor bonds. Since there is no difference in the etching behavior at different potentials for the rhombic dodecahdra, the steady tetrahexehedra facets are the same. The observed curvature of the facet trajectories for the rhombic dodecahedra is caused by the ability to remove probablistically unlikely 7-coordinate surface atoms on the {110} facets. The difference in coordination of the interior atoms on the {100} surface of the cube and the {110} surface of the rhombic dodechedra explains why the chemical potential controlled by the $FeCl_3$ concentration determines the facet when etching cubes but not for rhombic dodecahedra.

This study of the effect of $FeCl_3$ concentration in graphene liquid cell experiments has implications for both colloidal synthesis as well as liquid cell development. It has been shown that the $FeCl_3$ concentration determines the chemical potential of the etching in the liquid cell which determines which atoms can be removed. Through this control, the effect of potential in high-driving-force etching regimes was able to be elucidated and the mechanisms understood. For researchers seeking to make nanocrystals with high index facets for applications such as catalysis, it is better to etch from the {100} facet and use the chemical potential to control exactly which {hk0} facets are made. Through the combination of graphene liquid

cell, Monte Carlo simulations, and zero temperature ball models, the mechanisms of high-driving-force etching were revealed and the chemistry of liquid cell electron microscopy was understood a little better.[48]

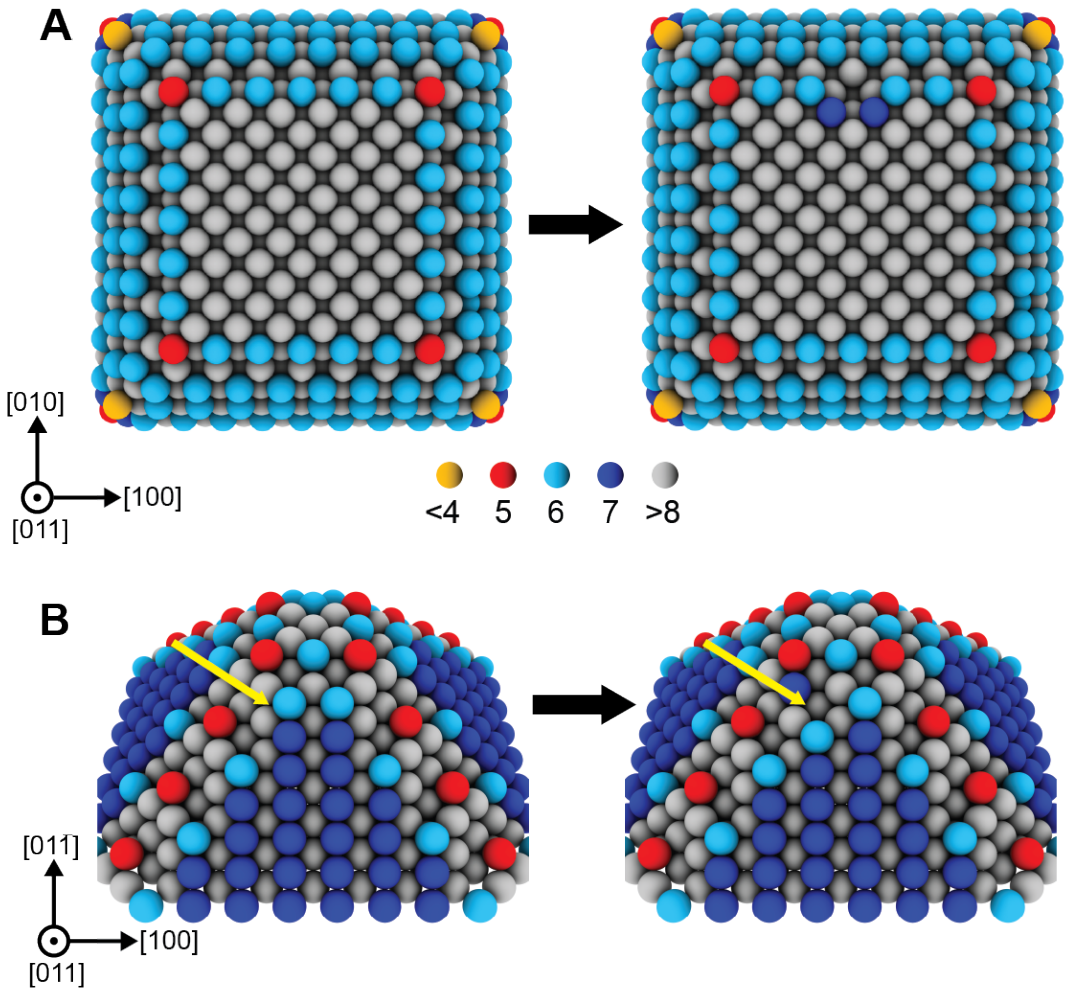

Figure 3.9: Atomic-level differences in the effect of chemical potential on etching of face-centered cubic nanocrystals. A) For a cube, after removing a 6-coordinate edge atom, two 7-coordinate interior atoms are revealed. Modulating the etching potential changes the likelihood of removing that interior atom. B) For a rhombic dodecahedra, after removing a 6-coordinate edge atom, a 6-coordinate interior atom is revealed. Modulating the potential does not change the likelihood of removing that interior atom.

Chapter 4

Controlling Oxidative Etching Using the Electron Beam Dose Rate

The chemical environment in the graphene liquid cell is complex due to electron beam-generated radiolysis products. From a materials science perspective, it is challenging to design liquid cell electron microscopy experiments to isolate specific phenomena when the composition of the liquid environment is undefined. Understanding and controlling the chemistry of the graphene liquid cell is critical for enabling systematic and reproducible experiments. The initial $FeCl_3$ concentration and the electron beam are two variables that cause etching of gold nanocrystals, but the interaction between those two factors and how they induce oxidative etching is unknown. In the previous chapter, it was shown that the initial $FeCl_3$ concentration modulates the chemical potential of the oxidative etching, and this determines which atoms can be removed. In this chapter, through the analysis of volume trajectories of etching nanocrystals while varying the electron beam dose rate, the impact of the electron beam dose rate on the chemical environment will be elucidated. Understanding the chemical changes induced by the electron beam will also provide insights into how $FeCl_3$ controls the chemical potential of the oxidative etching. Finally, *ex situ* etching experiments will be used to confirm the mechanisms seen in the liquid cell as well as yield further information about the chemistry of the graphene liquid cell environment. Through a deeper understanding of the chemistry of graphene liquid cell experiments, controllable tuning of the liquid environment will enable observation of a wider array of intriguing nanoscale phenomena.

4.1 Tracking Etching Nanocrystals Volume Trajectories

Gold nanocrystal etching is a useful probe of the chemical environment in the graphene liquid cell due to the well-defined nature and geometry of the initial nanocrystals and the developed knowledge of their oxidative etching processes.[46–48] Using a combination of $FeCl_3$ and electron

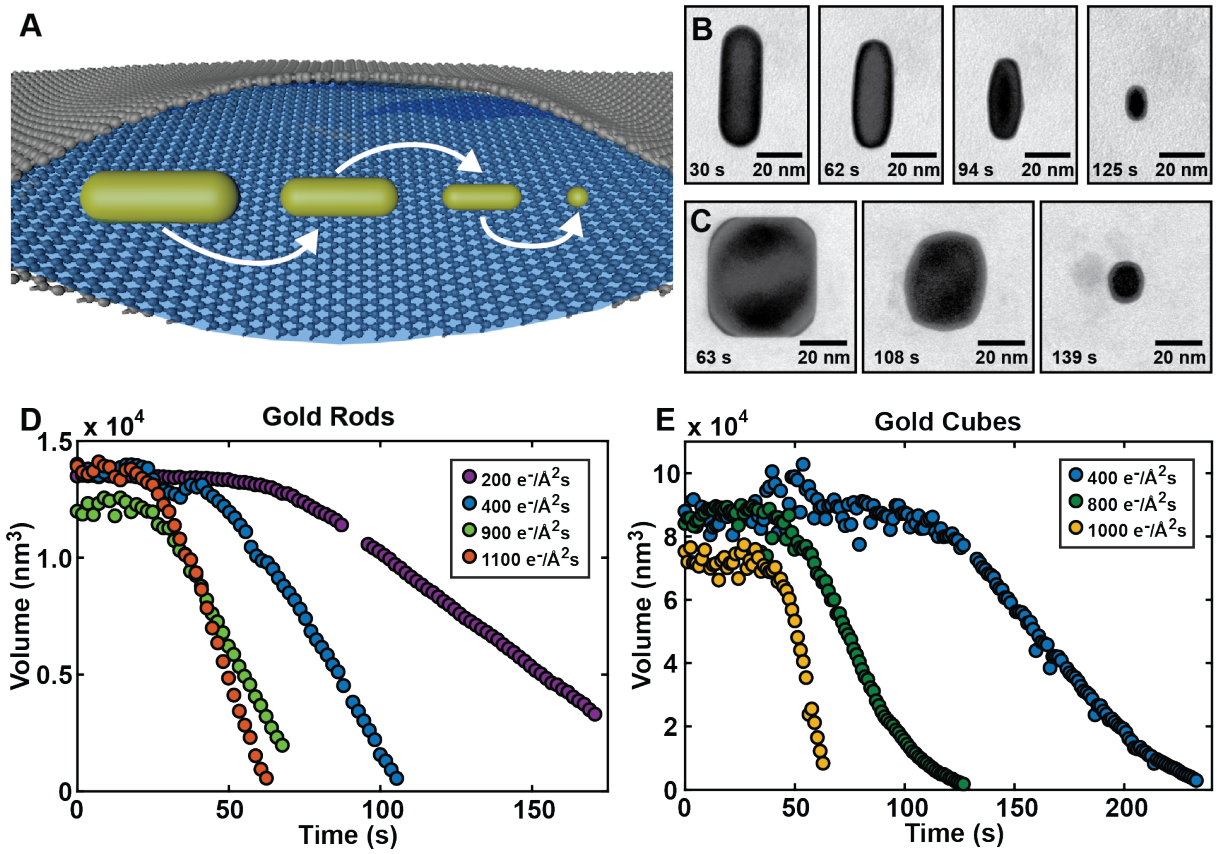

Figure 4.1: Following volume trajectories of gold nanocrystals during oxidative etching. A) Schematic of a gold nanorod etching in a graphene liquid cell. B) Representative images from gold nanorod etching. C) Representative images from gold cube etching. D) Volume trajectories of individual gold rods etching at different electron beam dose rates. E) Volume trajectories of gold cubes etching at different electron beam dose rates. Notice the similarity in the trajectory behavior between the nanorods and nanocubes.

beam induced radiolysis products, gold nanocrystals can be etched in the graphene liquid cell, where the shape and size tranformations of the gold nanocrystals can be followed over time. (Figure 4.1A,B,C) By tracking over 150 individual nanocrystal trajectories at defined electron beam dose rates, the effect of the electron beam on the etching process can be elucidated. From the 2D TEM images, the 3D shape of the nanocrystal can be extracted using image analysis techniques. (Appendix A.3) The volume trajectory can be plotted for both nanorods and nanocubes showing similar trends with three destinct regions. (Figure 4.1D and E) Initially, no etching occurs during an induction period despite being at an electron beam dose rate sufficiently high enough to etch the nanocrystals. After the induction period, etching proceeds at a constant rate that increases with increasing electron beam

dose rate. Finally, some of the trajectories exhibit a slowing of the etching rate when the nanocrystal becomes small. Understanding each region of the reproducible trajectory will yield information about how the chemistry of the liquid cell can be controlled by the electron beam dose rate.

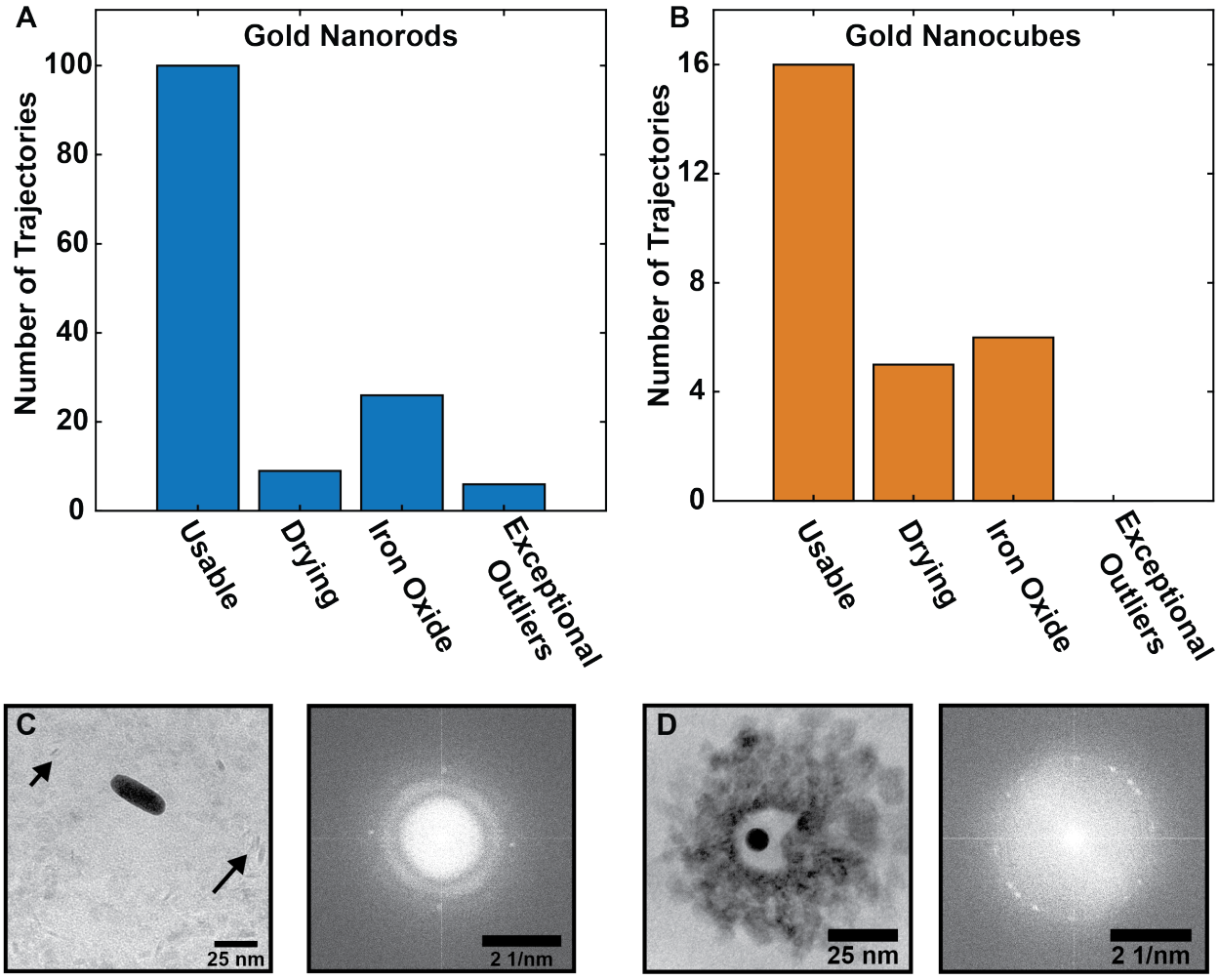

Figure 4.2: Some etching trajectories were unusable due defined failure modes including drying of the pocket, iron oxide precipitation, and exceptionally high etching rates more than 3 standard deviations above the average. A) Distribution of etching trajectories for gold nanorods. B) Distribution of etching trajectories for gold nanocubes C) FeO(OH) precipitation that did not affect the etching rate. D) $Fe(OH)_3(H2O)_{0.25}$ precipitation that caused a slowing of the etching rate.

Before analysis of the volume trajectories, it is important to acknowledge failure modes that led to abnormal etching behavior and unusable data. (Figure 4.2A and B) First, roughly

8% of the graphene liquid cell pockets dried out during etching, leading to a quantifiable slowing of etching rate and ultimately termination of the etching. This drying of the pocket was also characterized by lack of bubble movement and dried solvent features in the background. A small number of nanorods had exceptionally fast, greater than three standard deviations above the average, etching rates likely caused by abnormally formed pockets or aberrantly high concentrations of etchant species in the local environment. The final cause of unusable data, and the largest prevelence of the failure modes, was precipitation of iron oxyhydroxides around the nanocrystal. A benign iron oxyhydroxide precipitate in solution near the nanocrystals was found to be FeO(OH) using HRTEM.[49,50] (Figure 4.2 C) More troublesome was the precipitation of $Fe(OH)_3(H2O)_{0.25}$ around the nanocrystal, determined using HRTEM.[49,51] (Figure 4.2D) When this iron oxyhydroxide grew on or closely surrounding the nanocrystals, it limited the etchant species from reaching the surface of the gold nanoparticles. Roughly 20% of the etching videos showed this diffusion limited etching that resulted in a slower, but still constant, etching rate. (Figure 4.3) Formation of the iron oxyhydroxides is unsurprising given the liquid cells contain preloaded $FeCl_3$ and highly reactive radiolysis products. The iron oxyhydroxide precipitation appeared to be suppressed when the added nanocrystal solution was thoroughly cleaned of excess ligands although the exact cause of this observation is not well understood. The majority of the etching trajectories did not show any of these failure modes and provided a sufficient amount of data to draw conclusions about the effects of the electron beam dose rate.

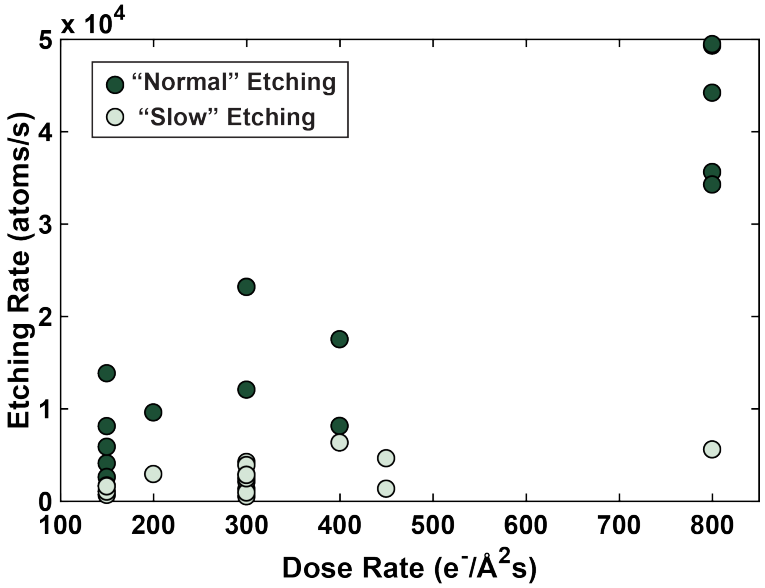

Figure 4.3: Precipitation of iron oxyhydroxide around nanocrystals leads to measureably lower diffusion-limited etching rates.

4.2 Hydrogen Bubble Induction Period

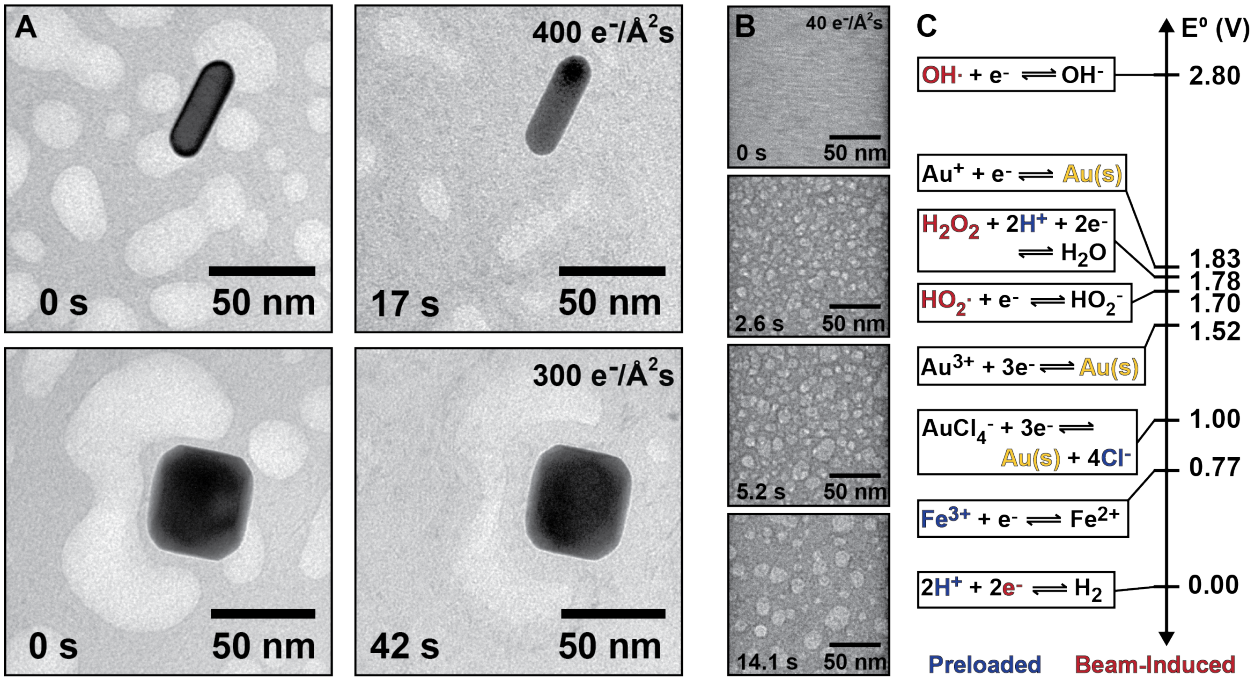

Figure 4.4: Hydrogen nanobubbles are generated at low electron dose rates and are a sacrificial reductant that sets a time zero for the etching process. A) Bubbles are observed around nanocrystals at time zero. As the electron beam illumination continues, the bubbles are consumed. B) Representative images of bubble generation at a low electron beam dose rate of 40 $e^-/Å^2s$. C) Oxidation potentials of species in the liquid cell in volts under standard conditions including beam-generated species (red), preloaded species (blue), and gold species (yellow).

All of the etching trajectories show an initial induction period of no etching, and this is a beneficial feature that allows the etching process to be fully captured while also providing useful insight into the chemistry of the graphene liquid cell. In the beginning of the data collection procedure, nanocrystals are found in the liquid pockets while imaging at low dose rates (20 to 40 $e^-/Å^2s$) to prevent premature etching before video collection has started. After focusing on the nanocyrstal of interest, an automated script is used to begin collecting a TEM time series while simultaneously increasing the electron beam dose rate to the etching dose rate (between 300 and 1300 $e^-/Å^2s$). This is considered time zero for the etching process. At the time zero, bubbles can be seen surrounding the nanocrystals. (Figure 4.4A) As the electron beam illumination continues, the nanobubbles decrease in size, and etching of the nanocrystals commences when the bubbles are fully consumed. The bubbles, which are generated at low electron beam dose rates (Figure 4.4B), protect the nanocrystal from

etching. The generation and consumption of the bubbles happens even in graphene liquid cells that are not pre-loaded with nanocrystals. (Figure 4.5) This reproducible protection of the nanocrystals is a useful feature that provides a time zero for the etching process and allows the entire dynamics of etching to be observed.

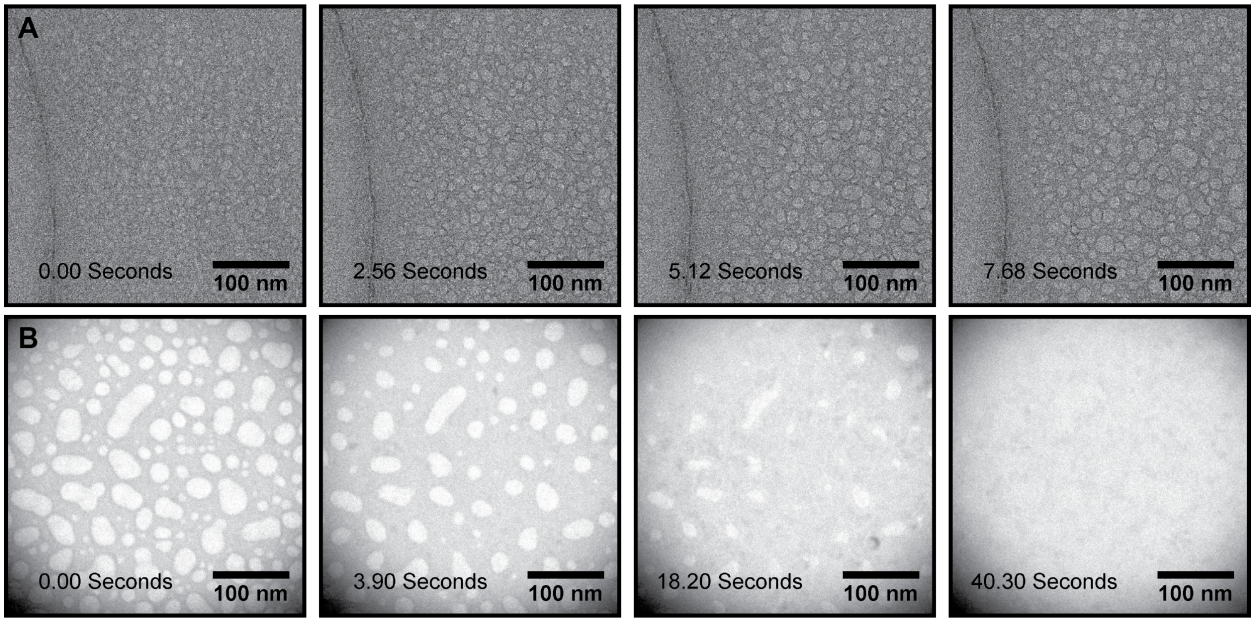

Figure 4.5: Bubble generation and consumption occurs even in graphene liquid cells without pre-loaded nanocrystals. A) Generation of bubbles at low dose rates (20 $e^-/Å^2s$) B) Consumption of bubbles at higher dose rates (400 $e^-/Å^2s$)

Utilizing knowledge of oxidation chemistry and literature precedent of dynamics in liquid electron microscopy, the bubble behavior can be explained. *In situ* spectroscopy to exactly determine the concentrations of species in the liquid cell during electron beam radiation is not currently experimentally possible. However, indirect methods such as monitoring the dynamics of nanocrystals and bubbles can be used to learn about the environment in the liquid cell. Radiolysis of water has been previously shown to generate hydrogen gas,[38,42,43,52,53] so it is reasonable to deduce that the bubbles generated upon electron beam irradiation are hydrogen gas. The temperature in the liquid cell is thought to only rise a few degrees celsius under electron beam irradiation, so it can be concluded that the bubbles are not thermally generated.[53,54] At increased electron beam dose rates, it is proposed that more oxidative radical species are generated, and these oxidative species consume the hydrogen bubbles that are generated at low electron beam dose rates. By modeling the chemistry of the liquid cell pocket using the rates of all the interrelated reactions,[43] the concentration difference between oxidative species and reductive species is shown to increase.[44] (Figure 1.6) Of the oxidative species generated through the radiolysis of water by the electron beam, the strongest oxidiz-

ers are the OH radical, H_2O_2, and HO_2 radical.[55–59] Among the species in solution including the gold nanocrystals, the iron ions, and the hydrogen bubbles, the hydrogen gas is oxidized most easily. Through this mechanism, the hydrogen bubbles generated by the radiolysis of water at low electron beam dose rates are oxidized first when the electron beam dose rate increases, thereby acting as a sacrificial reductant in the system and preventing premature etching of the nanocrystals.

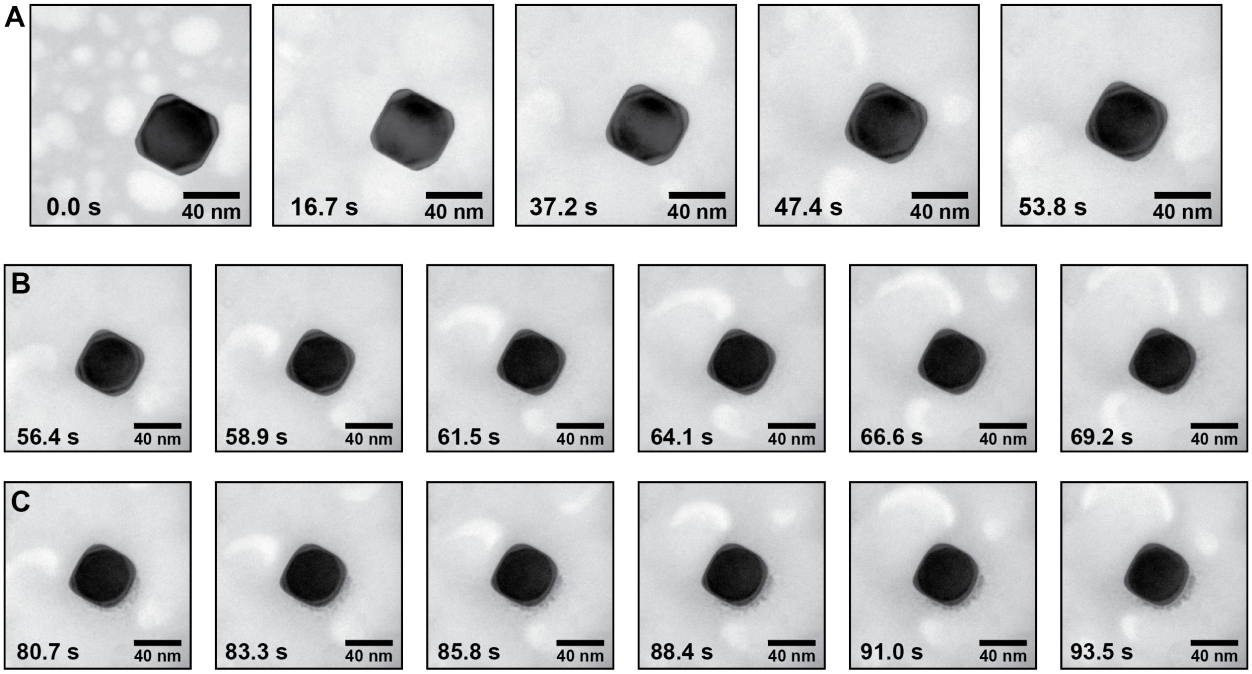

Figure 4.6: Bubble movement around a nanocrystal in the graphene liquid cell A) Consumption of bubbles in the imaging window when the electron beam dose rate is increased. B) Bubbles enter from outside the viewing window and begin circling the nanocrystal. C)The circling behavior of the bubbles entering from outside the viewing window is remarkably consistent and repeatable.

The movement and dynamics of the nanobubbles provide valuable insight into the physical structure of the graphene liquid cell pockets. After irradiation by the electron beam, the small bubbles initially generated rapidly coalesce into larger, stable nanobubbles. (Figure 4.5A) These bubbles are often seen aggregated around the gold cubes and rhombic dodecahedra. (Figure 4.4A) There is less aggregation around the gold nanorods (Figure 4.4A), suggesting the liquid pocket is closer in size to the 50-60 nm cubes. It is unlikely that the nanocrystals are wrapped tightly by the graphene sheets as the nanocrystals etch uniformly. Additionally, squeezing out the last few nanometers of water necessary to wrap the nanocrystals has been shown to be extremely difficult.[60,61] After increasing the electron beam dose rate and consuming the hydrogen bubbles in the viewing window, bubbles

move in from outside the viewing area towards the nanocrystal before being consumed themselves. The nanobubbles never travel over the nanocrystal and instead, rotate consistently around the nanocrystal. (Figure 4.6) This is further evidence that the pocket thickness is not significantly more than the nanocrystal size. Movement of the nanobubbles towards the nanocrystal is slightly unexpected with the visible diffusion of gold ions away from the nanocrystal. It is possible that the nanocrystals are bulging the pocket slightly, which results in the bubbles being drawn towards the nanocrystals. The nature of nanoscale bubbles has been heavily studied using liquid cell electron microscopy,[53,54,62–64] but this system could allow future researchers to study the response of nanobubbles to fluid current or driving force. In most liquid cell electron microscopy experiments, the beam-generated bubbles are a nuisance that impede the desired observation;[28,45,65] however, for the etching of metallic nanocrystals, the nanobubbles are a useful sacrificial reductant that also provide information on the liquid cell environment.

4.3 Etching Rate Dependence on Electron Beam Dose Rate

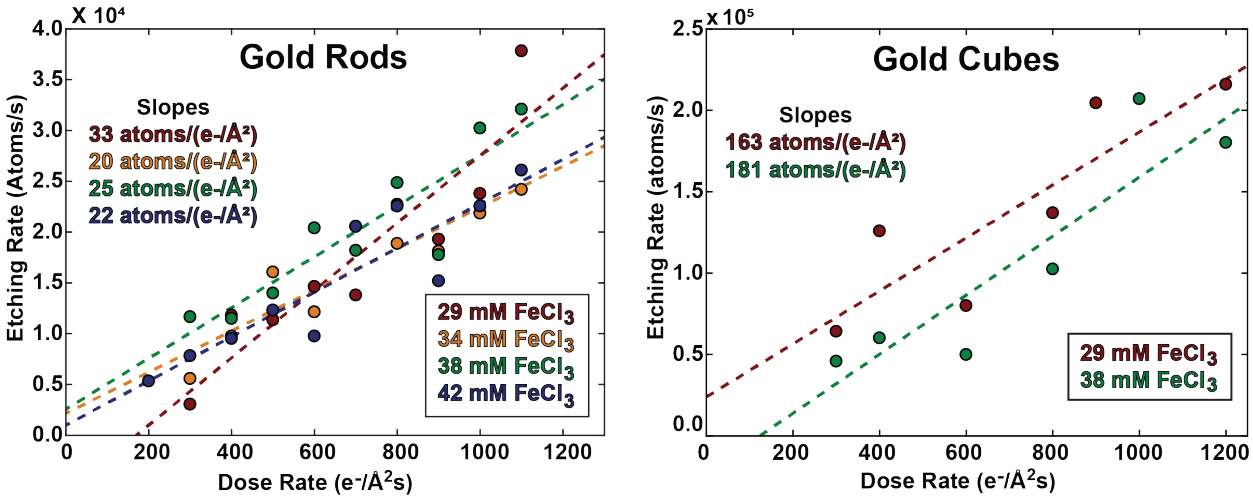

Figure 4.7: The etching rate of gold nanorods and gold nanocubes varies linearly with the electron beam dose rate, and the initial $FeCl_3$ concentration does not have a measurable effect on the etching rate. Each data point is the average of multiple etching trajectories at that dose rate and $FeCl_3$ concentration.

Following the consumption of the hydrogen bubbles, etching of the gold nanocrystals commences at a steady rate, and the effect of $FeCl_3$ concentration and electron beam dose rate on the etching rate can be used to understand the chemistry occurring in the graphene liquid

cell environment. In each graphene liquid cell containing different, predetermined, initial concentrations of $FeCl_3$, many individual trajectories of nanocrystals etching at different electron beam dose rates can be collected using a home-written, automated TEM dose rate script. In Figure 4.7, the average etching rates for nanocrystals at varying dose rates are shown, and the colors represent the initial concentration of $FeCl_3$ in the liquid cell. The etching rate varies linearly with the electron beam dose rate, indicating that the electron beam-generated oxidative species are the limiting reactant in the etching process. The etching rates are independent of the initial nanocrystals' size and surface area. (Figure 4.8) The data for the nanocubes has more scatter than the nanorods because it was more challenging to acquire large numbers of etching nanocube trajectories for averaging. The slope of the fits for the cubes are steeper than the nanorods due to the greater size of the cubes that enables the cubes to interact with a greater number of oxidative species over a larger region of the pocket. There is no measurable difference in the etching rate as the initial $FeCl_3$ concentration is modulated. In Chapter 3 of this thesis, it was shown that the same range of initial $FeCl_3$ concentrations led to a significant change in the chemical potential of the environment inducing a measurable change in the intermediate surface facets. The etching rate and surface facets can be independently controlled in the liquid cell by the electron beam dose rate and initial $FeCl_3$ concentration respectively, and this provides researchers the ability to systematically control the etching reactions in the graphene liquid cell.

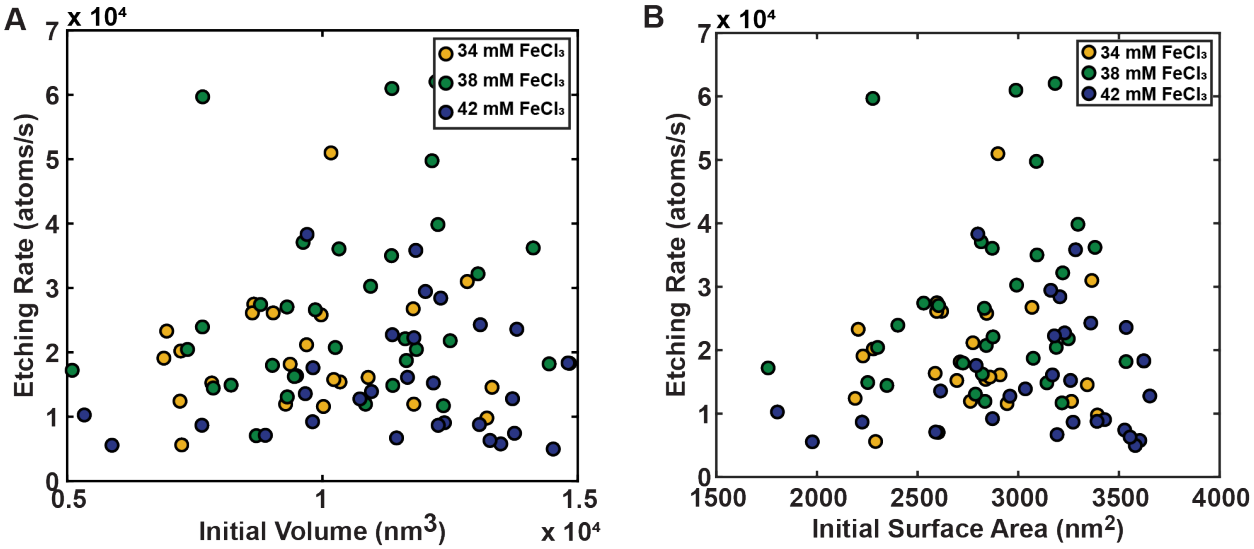

Figure 4.8: The etching rate of gold nanorods has no dependence on its initial volume (A) or surface area (B).

The independent effects of the etching rate and chemical potential is at first unexpected, but it yields useful insight into the chemistry of the liquid cell. Based on the oxidation potentials of the radiolysis products and the iron ions, (Figure 4.4), highly oxidative beam-

generated species such as OH radical and H_2O_2 are likely the reactive species that are oxidizing the gold surface atoms. This is consistent with the observation that the etching rate varies linearly with the electron beam dose rate. Although the total concentration of oxidizing species is controlled by the electron beam dose rate, not all beam-generated species are of equal oxidizing strength. Since the initial $FeCl_3$ concentration has been shown to determine the chemical potential of the liquid environment, it is proposed that the $FeCl_3$ modulates the ratios between the beam-generated species. Increased amounts of $FeCl_3$ cause a great ratio of stronger oxidizing species to weaker oxidizing species in the graphene liquid cell. This model allows the electron beam to control the etching rate by determining the total concentration of etching species in the liquid pocket, and the $FeCl_3$ controls which atoms can be removed by modulating the ratio between the beam-generated oxidative species.

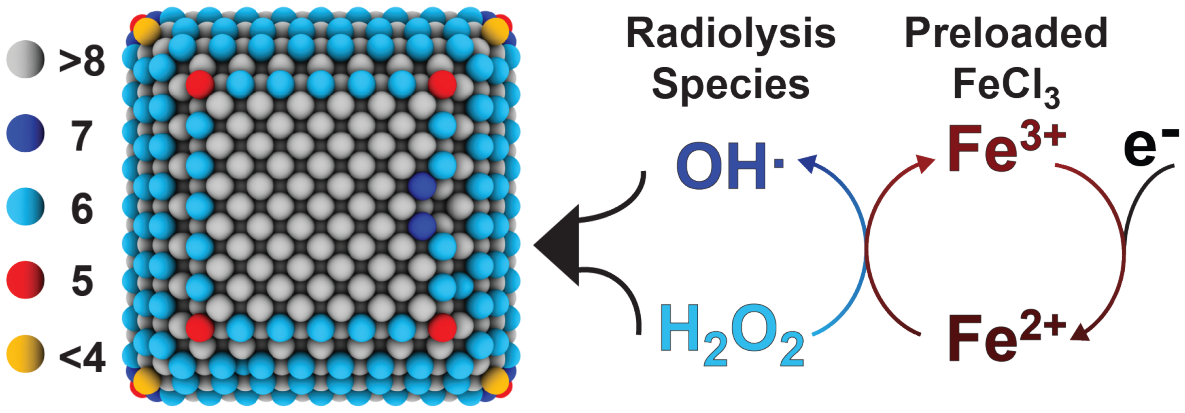

Figure 4.9: Model describing how the electron beam dose rate controls the etching rate and $FeCl_3$ determines which atoms can be removed. Returning to the zero temperature, atomic ball model, the surface of the etching nanocube has 6- and 7-coordinated edge atoms. Only the beam-generated oxidative species can remove these atoms, and the electron beam dose rates controls their total concentration. The $FeCl_3$ concentration determines the ratio between the oxidizing species of different strengths.

Deciphering the exact chemical path by which the $FeCl_3$ and the electron beam regulate the ratio and total concentration of oxidative species is challenging because the system is a complex mixture of interrelated reactions and equilibria. Ideally, the concentrations of the species in solution would be directly measurable using *in situ* spectroscopy techniques, but current experimental capabilities render such experiments unfeasible. However, a hypothesis about the chemistry of the graphene liquid cell can be proposed using the indirect observations of nanocrystal etchings. There is a strong literature precedent for iron ions reacting with H_2O_2 to form the more oxidative OH radical, similar to what is predicted in the liquid cell. Upon radiolysis of the water solution, Fe(III) ions would rapidly react with

the hydrated electrons in solution, producing Fe(II) ions.[66] These Fe(II) ions can react with H_2O_2 to form OH radical through the well-studied Fenton Reaction.[67–69] These two steps would be cyclic, both removing reductive hydrated electrons and converting H_2O_2 to the more oxidative OH radical while keeping the total concentration of oxidative species in solution constant. (Figure 4.9) This proposed pathway is simply one piece of a larger network of reactions and equilibria leading to a steady state of species in the etching environment, but the hypothesis that $FeCl_3$ can control the ratio of oxidative species is well within literature precedent, especially at low pH values.[66,70,71]

Although the nanocrystals etch at a constant rate until they become small, there is consistent evidence that the etching rate slows down at the end of the etching trajectories. Since this slowing of the etching rate is independent of the total etching time and is only correlated with the nanocrystal's size, it does not seem likely that this is a drying artifact. A more reasonable hypothesis is that the limiting reactant in the etching process is changing from the concentration of oxidative species in solution to the number of edge sites on the nanocrystal. Only surface atoms can be etched, so as the nanocrystals become small, it is reasonable that the number of available edge sites could become less than the concentration of etchants in solution. Future work could investigate how this crossover in limiting reactants changes with the electron beam dose rate and initial $FeCl_3$ concentration.

4.4 *Ex Situ* Correlative Etching of Gold Nanorods

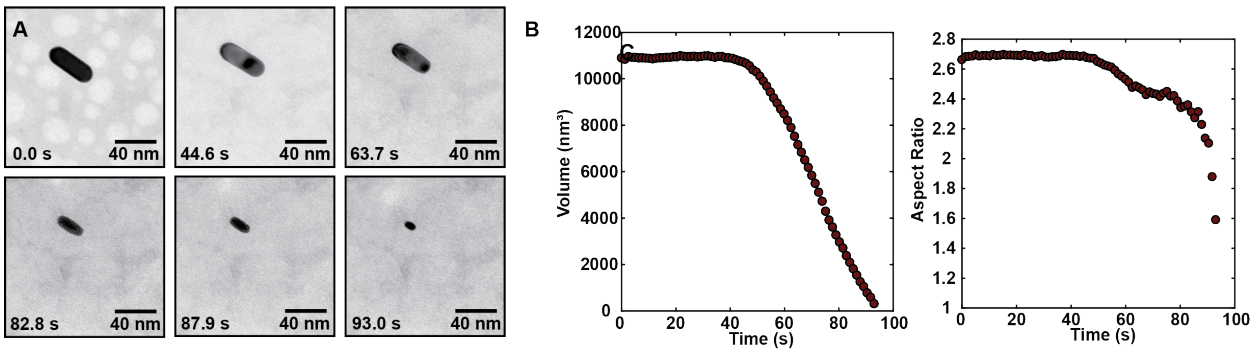

Figure 4.10: The aspect ratio of nanorods during graphene liquid cell etching remains relatively constant until the rod becomes small. A) Images from a representative etching trajectory. B) Volume and aspect ratio trajectory for nanorod in A).

The graphene liquid cell provides a window into understanding the dynamics of nanocrystal shape tranformations, but for the insight to be broadly applicable, correlative *ex situ* studies need to be performed. Gold nanorods have strong plasmon resonances that can be followed using UV/Vis spectroscopy to track the etching process for traditional benchtop

reactions. The energy of the longitudinal surface plasmon resonance (LSPR) of the nanorod depends on its aspect ratio (ratio of major axis length to minor axis length), and the intensity of the LSPR depends on the size of the nanorod. Therefore, the size and aspect ratio of nanorods during *ex situ* etching can be compared with the size and shape trajectories of nanorods etching in the graphene liquid cell. (Figure 4.10) Following the LSPR is a bulk technique averaged over many nanocrystals in solution, so individual trajectories and subtle shape transformations such as faceting can no longer be tracked. However, correlative *ex situ* studies show that the dynamics observed in the liquid cell translate to synthetic methods commonly carried out in traditional laboratories.

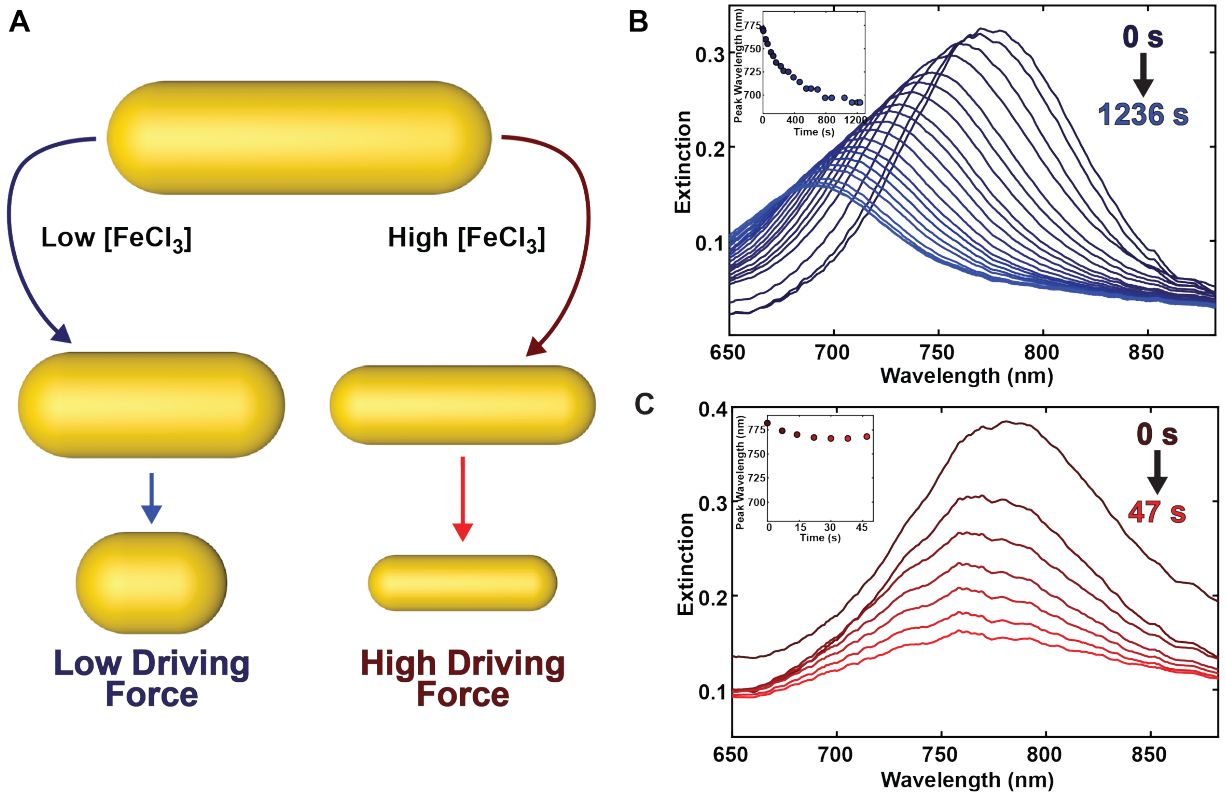

Figure 4.11: *Ex situ* etching of gold nanorods tracked by their LSPR. A) Schematic of how the aspect ratio changes during etching in the high- and low-driving-force regimes. B) Extinction spectra while etching gold nanorods at low-driving-force. Inset shows the blue-shifting of the LSPR. C) Extinction spectra while etching gold nanorods at high-driving-force. Inset shows the LRPR staying relatively constant.

Reproducing the etching behavior from the graphene liquid cell in *ex situ* synthesis requires control of the etching kinetics. Previous work has shown etching of gold nanorods from the tips using $FeCl_3$, causing a decrease in the aspect ratio of the nanorods and leading to a

blue-shift in the LSPR.[72,73] Since the lowest coordinated atoms on the tips of the nanorods are being removed, this etching behavior occurs in the low-driving-force regime. The etching of gold nanorods in the graphene liquid cell have a constant aspect ratio until the nanorods became small. (Figure 4.10) In this high-driving-force regime, atoms are etched from both the sides and the tips. In the *ex situ* etching experiments, the driving force was controlled by modulating the concentration of $FeCl_3$ in the system. Increasing the $FeCl_3$ concentration from 0.135 M to 1 M changes the oxidative etching of the nanorods from low-driving-force etching to high-driving-force etching. (Figure 4.11B and C)

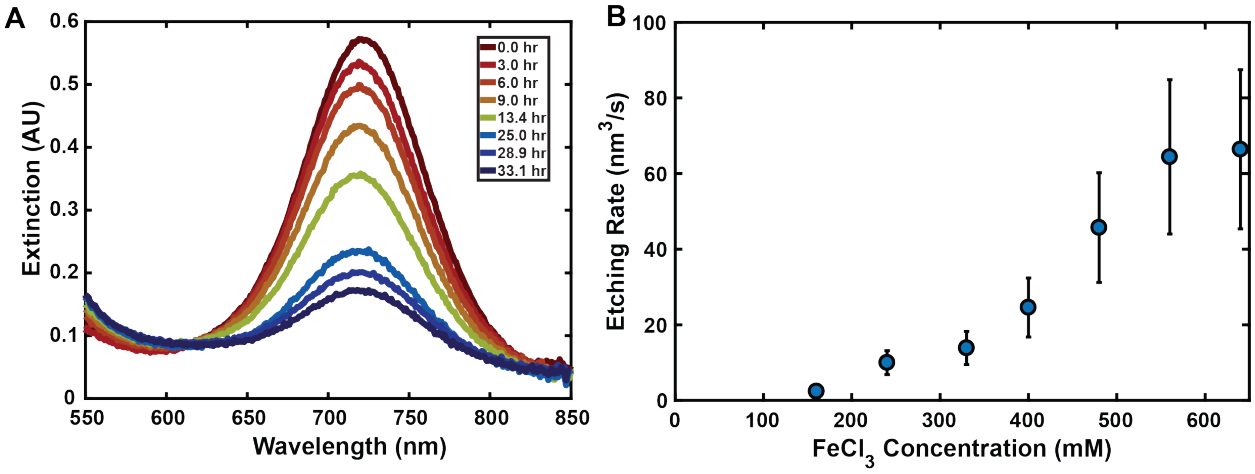

Figure 4.12: Etching rates of *Ex Situ* etching of gold nanorods with $FeCl_3$. A) Etching of gold nanords with the same initial conditions as the graphene liquid cell (40 mM $FeCl_3$. The etching takes over 30 hours, much slower than the 30 second etching in the liquid cell. B) *Ex Situ* etching rates of gold nanorods as a function of $FeCl_3$. For comparison, the graphene liquid cell etching experiments had an initial $FeCl_3$ concentration of 25 to 45 mM and electron beam dose rate dependent etching rates between 100 and 1000 nm^3 per second.

With the ability to reproduce the etching observed in the graphene liquid cell, comparisons can be made between the two environments to better understand the chemistry in the graphene liquid cell. A solution containing the same contents as the graphene liquid cell (Tris Buffer-HCl, 40 mM $FeCl_3$, gold nanorods) takes over 30 hours to etch without the electron beam, confirming the hypothesis that the strong oxidizing species generated by the electron beam are actively inducing the faster etching. (Figure 4.12) Getting to the high-driving-force etching regime requires a concentration of $FeCl_3$ that is 25 times greater than what was used in the graphene liquid cell experiments. The observation in the liquid cell of no difference in the etching rate between 29 and 42 mM of $FeCl_3$ is consistent with *ex situ* concentration dependent studies that show that range of $FeCl_3$ would have no measurable change on etching rate. High-driving-force etching opens new synthetic pathways to making high energy nanocrystals, and the goal would be to use colloidal synthesis to make large numbers of these

shapes. This requires stopping the etching process and locking in the kinetic shape. However, keeping the kinetic shape intact is challenging because the nanocrystal surface can readily rearrange to a lower energy shape. The rearrangement is consistent with *in situ* observations of nanocrystals in drying pockets. After a liquid cell has dried, nanocrystals transition from the intermediate tetrahexahedral shape back to lower energy cubes or truncated octahedra. (Figure 4.13) This rearrangement of the surface atoms shows the value of *in situ* techniques including liquid cell TEM. In the future, efforts to lock in the surface atoms on these kinetic shapes could involve using tighter binding ligands or low-temperature quenching. The ability to reproduce high-driving-force etching mechansims outside the graphene liquid cell opens up new opportunities to make non-equilibrium nanocrystal shapes with high energy facets.

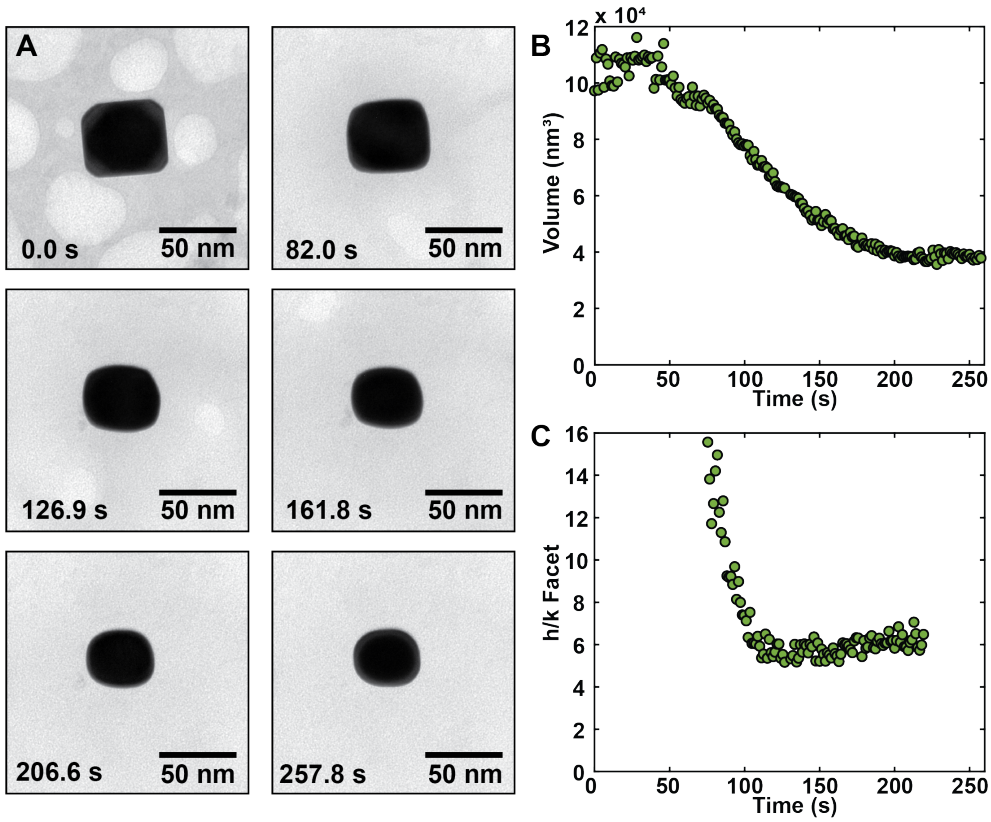

Figure 4.13: Relaxation to lower energy facets after the liquid cell pocket dries. A) Representative images from a nanocube etching to an intermediate tetrahexahedra before stopping etching as the pocket dries. After etching stops, the nanocrystal transforms back to a cube or cube octahedra shape. B) Volume trajectory C) The h/k facet value increases after etching stops.

Understanding the chemistry during liquid cell electron microscopy is critical to performing reproducible and sytematic materials science experiments. Since etching of gold

nanocrystals yields a wealth of size and shape information, these etching processes are an enlightening probe of the chemical environment. Through the understanding of the effect of the electron beam dose rate and initial $FeCl_3$ concentration on the etching rate, the etching rate and chemical potential can be independently tuned to explore specific etching phenomena. Electron beam effects such as bubbles can be mitigated or even utilized to the advantage of the researcher. Coupling the electron beam-generated species with known processes such as the Fenton Reaction show how systematic experiments can be performed using liquid cell electron microscopy. Finally, the work in the liquid cell ultimately should inform traditional colloidal processes outside of the electron microscope, so correlative studes help show how insights can be translated to benchtop chemistry. Liquid cell electron microscopy is a powerful technique for understanding nanoscale processes, and through the developed understanding of the chemistry in the liquid pockets, the technique will be even more versitile and informative.[74]

Chapter 5

Other Nanocrystal Systems Studied Using Liquid Cell TEM

In situ electron microscopy can be used to observe a variety of other phenomena beyond oxidative etching. Visually striking processes such as the Kirkendall effect and electron stimulated desorption of alkali halides can be imaged in the electron microscope in realtime during the transformations. The following sections will explore this work, including the observations, analysis, and potential future directions. Although the data is intriguing, the chemical environment in the graphene pocket is much less understood for these processes than the work presented in Chapters 3 and 4. This makes it difficult to draw too many meaningful conclusions about the observations' relevance to *ex situ* dynamics, but further development of these systems could eventually lead to control similar to oxidative etching in the liquid cell.

5.1 Kirkendall Effect in Silver Nanocrystals

The Kirkendall effect is a useful synthetic approach for making unique hollow structures as well as a way to understand atomic diffusivities, so observing and quantifying the process through liquid cell electron microscopy could provide a wealth of information. The Kirkendall effect was first reported in 1942 and showed how differing diffusivities of atoms can lead to inequitable mass flow and the formation of hollow voids.[75] Since the discovery of the nanoscale kirkendall effect in 2004,[76] the technique has been used to synthesize many different hollow colloidal nanoparticles and nanotubes.[77–81] Extensive experimental work has gone into understanding this complex process, but most of the research involves stopping the reaction and imaging aliquots of the sample.[80–82] As we have shown previously in Chapter 4, *in situ* experiments can be useful for removing possible artifacts from the quenching and drying process. *In situ* TEM experiments using a silicon nitride liquid cell have been done using bismuth nanocrystals,[83] and we hoped to build on this work by studying silver nanocrystals with the enhanced resolution of the graphene liquid cell.

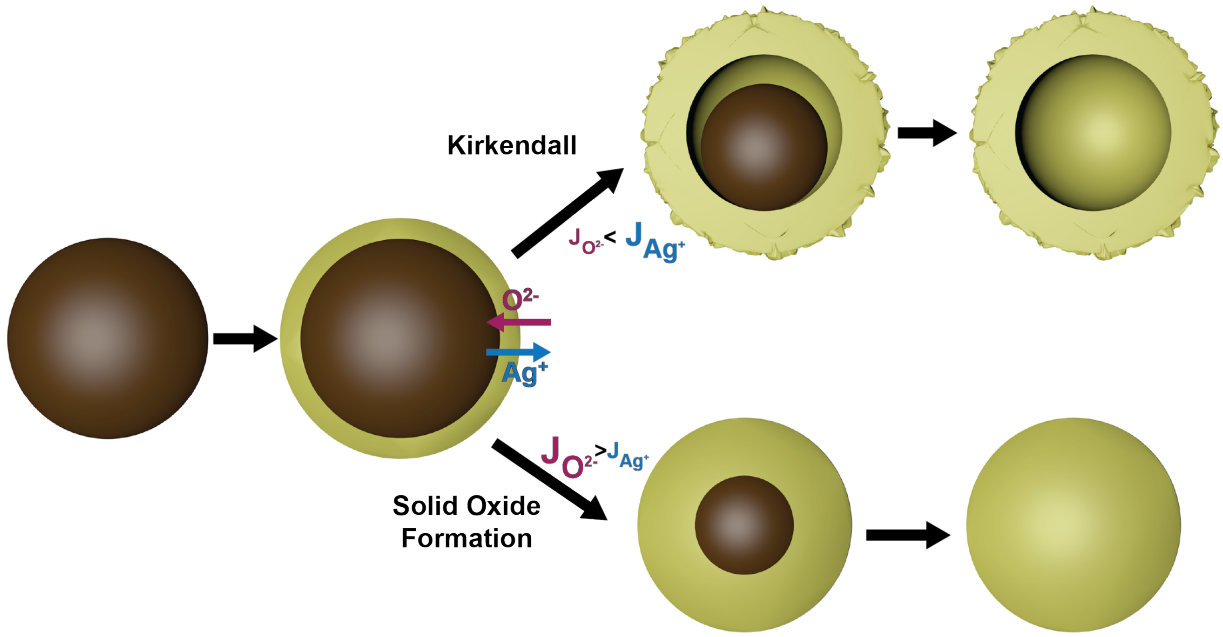

Figure 5.1: Schematic of the nanoscale Kirkendall effect for oxidation of silver nanoparticles. If the diffusivity of silver ions in the oxide shell is greater than the diffusivity of oxygen ions, then oxide will grow outward creating a hollow shape. If the diffusivity of oxygen ions is greater than the diffusivity of silver ions, then a solid oxide nanoparticle will form.

The overall mechanism of the Kirkendall effect is simply a difference in diffusivities. For the oxidation of silver nanoparticles, the two diffusing species are oxygen and silver atoms. After the outer layer of the silver nanoparticle is oxidized, there are two options for further oxidation. If the diffusivity of oxygen atoms through the silver oxide shell is greater than silver atoms, oxygen will diffuse through the oxide shell and react with the silver core, yielding a solid silver oxide nanoparticle. (Figure 5.1) However, if the diffusivity of silver through the shell is greater than oxygen, silver atoms will leave the silver core and react with oxygen near the oxide shell's outer interface. This will leave behind vacancies in the silver core which will eventually coalesce into hollow volumes. This Kirkendall process results in a hollow oxide nanoparticle. The ratio of diffusivities of silver and oxygen atoms through the silver oxide shell determines the direction of mass flow, and usually the actual behavior is between the two extremes shown in Figure 5.1 for each individual system, with oxide growth both inward and outward.

Upon electron beam illumination, the silver nanocyrstals begins decreasing in size. However, a lighter contrast ring also begins forming around the silver nanoparticle, indicating the nanocrystal is undergoing the Kirkendall effect instead of oxidative etching. (Figure 5.2A) Eventually, the vacancies in the silver core coalesce, usually at one or more of the tips of the

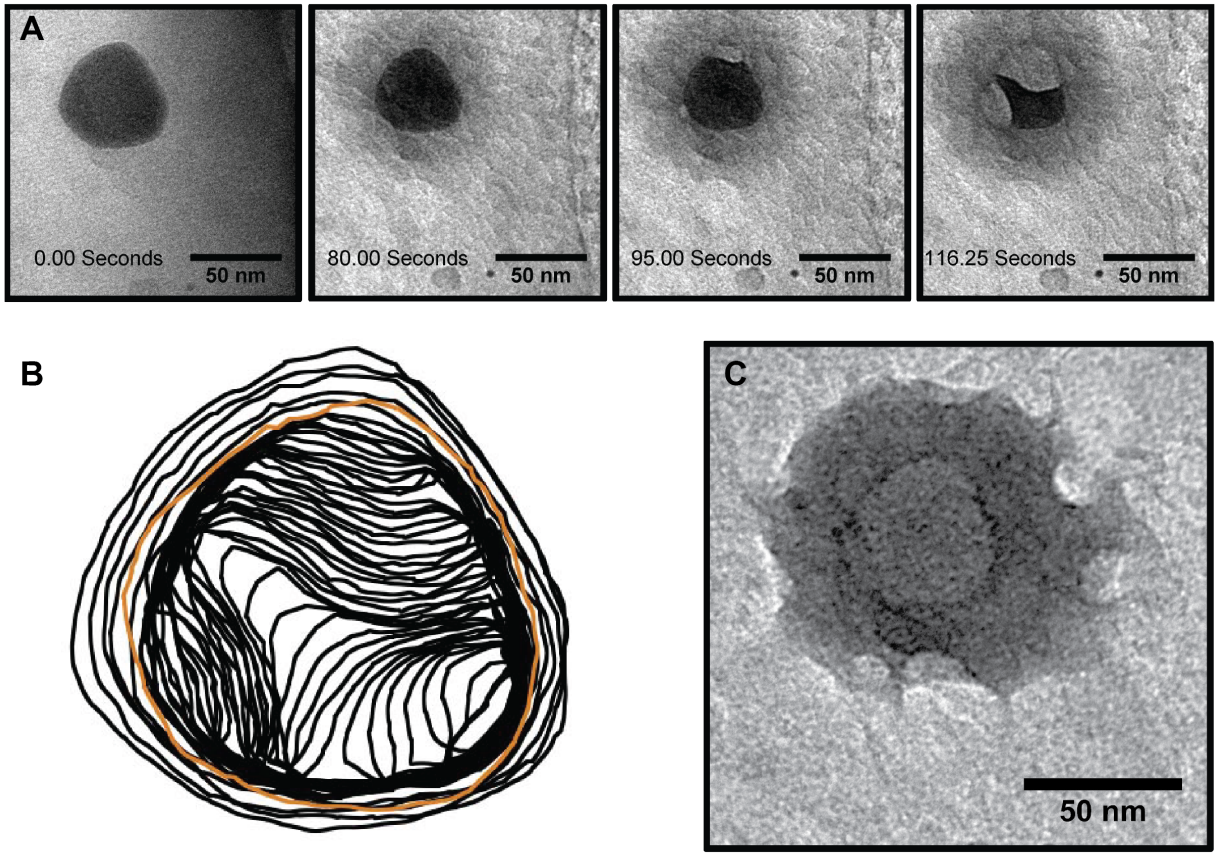

Figure 5.2: Kirkendall effect of oxidation of silver nanocrystals in the graphene liquid cell. A) Images from a representative trajectory of a silver nanocrystal undergoing the Kirkendall effect. B) Outlines from the video in the top panel. Orange outline is the nanocrystal when the vacancies coalesced. C) Final silver oxide nanocrystal.

former silver nanoparticle. The silver core continues to rapidly shrink in size as the oxide shell continues growing. The outlines of the inner silver core can be traced for each frame of the movie to follow the Kirkendall dynamics. (Figure 5.2B) The orange outline is at the time point of vacancy coalescence, showing both inward and outward oxide growth. This means neither the diffusivity of silver nor oxygen completely dominates. The final hollow silver oxide nanostructure is shown in Figure 5.2C, and the outer morphology seems to be somewhat influenced by the dryness of the liquid pocket, with indents in the surface corresponding to dry regions. This Kirkendall effect was imaged multiple times in the graphene liquid cell, so analytical models for this process can be used to extract more quantitative information about the transformation.

Using diffusion and mass balance equations, the diffusion constant of silver ions in silver

oxide can be extracted. The derivation of these equations is modified from Rubinstein et al.[84] Unlike many Kirkendall models, this model accounts for both oxygen diffusion inward and silver diffusion outward, which is necessary because silver oxide grows both inward and outward. (Figure 5.2B) In this model, the nanoparticles are approximated as spheres, so only videos with spherical nanoparticles are used in the analysis.

The diffusion of silver ions through the shell is:

$$\frac{dQ_{Ag^+}}{dt} = -4\pi D_{Ag^+}(c_{Ag^+,2} - c_{Ag^+,1})\frac{a_1 a_2}{a_1 - a_2} \tag{5.1}$$

where Q_{Ag^+} is the mass of the silver ions, t is time, D_{Ag^+} is the diffusion constant of silver ions in silver oxide, $c_{Ag^+,2}$ is the concentration of silver ions at the outer surface of the silver oxide shell, $c_{Ag^+,1}$ is the concentration of silver ions at the inner surface of the silver oxide shell, a_1 is the radius at the inner surface of silver oxide shell, and a_2 is the radius at the outer surface of silver oxide shell.

This diffusion of silver ions will equal the mass loss of silver in the core:

$$\frac{dQ_{Ag^+}}{dt} = -\frac{dQ_{Ag^0}}{dt} = \frac{4}{3}\frac{\rho_{Ag^0}}{FW_{Ag^0}}\pi a_0^3\frac{d\delta}{dt} \tag{5.2}$$

where Q_{Ag^0} is the mass of silver atoms in the core, ρ_{Ag^0} is the bulk mass density of silver, FW_{Ag^0} is the atomic weight of silver atoms, a_0 is the initial radius of the nanocrystal, and δ represents time in terms of the fraction of silver that has been converted to silver oxide:

$$\delta(t) = \frac{V_{Ox}(t)}{ZV_0} = \frac{V_0 - V_{Ag}(t)}{V_0} \tag{5.3}$$

where V_{Ox} is the volume of oxide, V_0 is the original silver nanocrystal volume, and Z is the coefficient of expansion from the silver to silver oxide.

Equation 4.1 and 4.2 can be set equal to each other and integrated with respect to time. Another useful definition which is the fraction of the oxide growth that is inward:

$$\phi = -Z\frac{dV_1}{dV_{Ox}} \tag{5.4}$$

where Z is the coefficient of expansion, dV_1 is the core contraction or change in the volume enclosed by the inner oxide interface, and dV_{Ox} is the change in the oxide volume.

The resulting equation for silver diffusion is:

$$\frac{k_{out}}{a_0^2}t = (1 - \frac{\phi}{Z})\frac{Z - \phi[1 - (\phi - Z)\delta]^{\frac{2}{3}} - (Z - \phi)(1 - \phi\delta)^{\frac{2}{3}}}{2(Z - \phi)\phi} \tag{5.5}$$

where k_{out} is:

$$k_{out} = \frac{FW_{Ag^0}}{\rho_{Ag^0}}D_{Ag^+}(c_{Ag^+,2} - c_{Ag^+,1}) \tag{5.6}$$

From the outlines of silver nanocrystals undergoing the Kirkendall effect, all of the values from the right side of Equation 4.5 can be calculated for each frame of the TEM video. Then, the right side can be plotted against time with the slope being equal to k_{out}/a_0^2. Using k_{out}, the diffusion constant can be calculated.

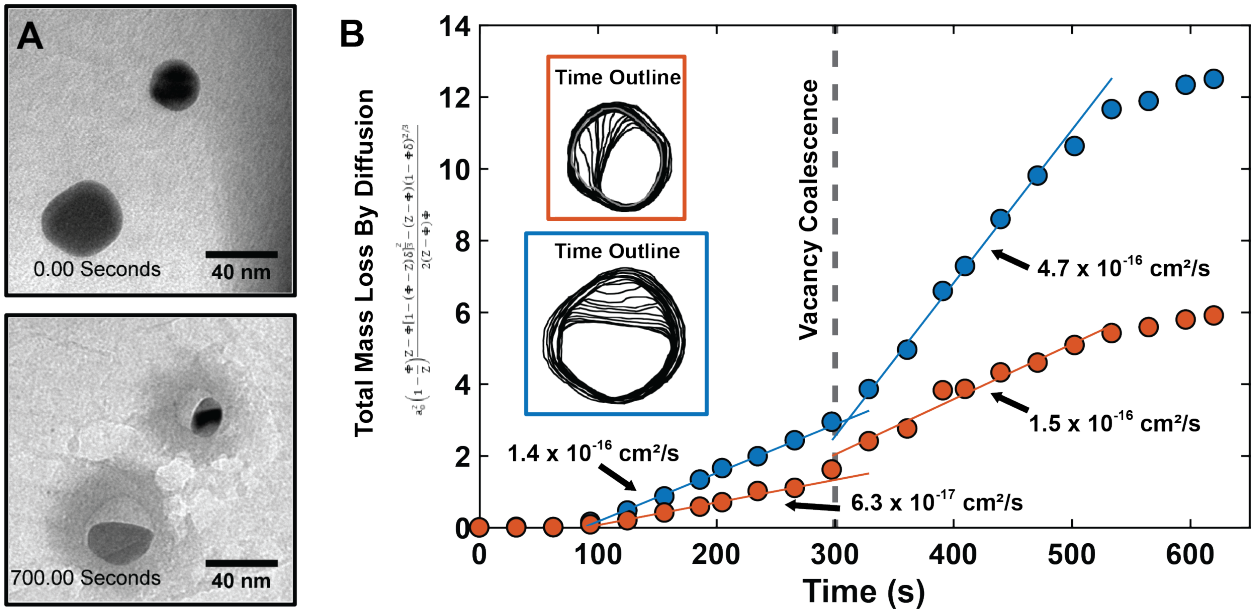

Figure 5.3: Graphical analysis of Kirkendall trajectories can yield the diffusion constant of silver ions in silver oxide. A) Initial and final frames of a TEM video of two spherical silver nanoparticles undergoing the Kirkendall effect B) Plot of the right side of Equation 4.5 against time. Inset is the outlines of the cores of the two nanocrystals being investigated. The gray dotted line shows the time point where the vacancies coalesced, leading to a noticeable change in slope. The diffusion constants based on the linear fits are shown in the figure. The slowing of the Kirkendall effect at the end of the trajectories is due to drying of the liquid pocket.

Using the derivation for mass flow during the Kirkendall effect and the outlines of the core for each frame, the diffusion constant of silver in silver oxide can be extracted. The spherical nanoparticles used in the diffusion constant analysis are shown in Figure 5.3A. From the outlines, the right-hand side of Equation 4.5 can be calculated for each frame and plotted against time, and linear fits to the plot can be used to calculate the diffusion constant of silver ions in silver oxide. (Figure 5.3B) When the vacancies coalesce, the calculated diffusion constants abruptly increase, but this shows a limitation of visual analysis techniques for the Kirkendall effect. The first diffusion constant likely underestimates the true value because random vacancies in the core are undetectable. The actual diffusion constant is likely near the middle of the calculated values, around 10^{-16} cm^2 per second. Previous literature analysis of

the Kirkendall effect using *in situ* transmission X-Ray microscopy (TXM) of 350 nm diameter silver nanowires oxidized in air over 30 minutes yielded a diffusion constant of silver in silver oxide of 1.2 x 10^{-13} cm^2 per second.[85] Potentially, the differences between our result and the TXM result might be due to our accounting for the diffusion of oxygen into the oxide shell in the analysis. The geometry and experimental resolution were also different for each study.

Although *in situ* graphene liquid cell of silver nanocrystal Kirkendall effect creates stunning videos that can be quantifiably analyzed, there are some shortcomings with the study. The chemistry during the reaction is not fully understood, so neither the nature of the oxygen source nor the parameters that determine oxidative etching versus oxidative Kirkendall effect are clear. Further, the unknown concentration of the oxidizing species means the oxygen diffusion constant cannot be calculated. The exact silver oxide was also not characterized, and it is not known if the oxide shell is even crystalline. Finally, the pockets seemed to be quite dry for these experiments, so the reaction may not have occurred in a completely liquid environment. To better understand the chemistry of the system, electron beam dose rate dependent studies could be performed similar to the work in Chapter 4. If the chemistry of the Kirkendall effect can be better understood, future experiments could investigate the Kirkendall effect in other nanoscale materials or nanostructures. Potentially, nanocrystals with areas of high curvature could cause unique vacancy coalescence and interesting resulting morphologies. The Kirkendall effect is a well-studied nanoscale process, and *in situ* electron microscopy imaging of the dynamics of this process provides a window into understanding the chemistry and physically properties that determine the final nanostructure.

5.2 Electron Stimulated Desorption of NaCl

In situ electron microscopy can also provide a unique perspective to watch electron stimulated desorption of alkali halide materials to better understand how to controllably modify materials' surfaces. Electron and photon beams can be used to pattern the surface of materials which is useful in a variety of technological applications.[86] Alkali halides are considered a model system for studying materials modification by electronic excitation due to their well-characterized geometric and electronic structures.[87,88] Through atomic force microscopy (AFM) and other spectroscopy techniques, it has been found that rectangular pits form on the surface of the material upon irradiation which eventually leads to layer-by-layer desoprtion of the material.[87,89–93] Imaging the surface using AFM after irradiation has yielded a wealth of information, but there is always the risk of surface rearrangement before the system can be captured with the AFM. Ideally this electron stimulated desorption could be performed while imaging in the electron microscope, and our expertise in nanomaterials can also provide new insights into how this process previously studied on bulk materials translates to nanocrystals.

Although this study will focus on the surface morphological transformations of NaCl, it is valuable to first consider the mechanisms behind electron stimulated desorption. Irradiation of alkali halides with electrons generates hot electron-hole pairs or free electrons

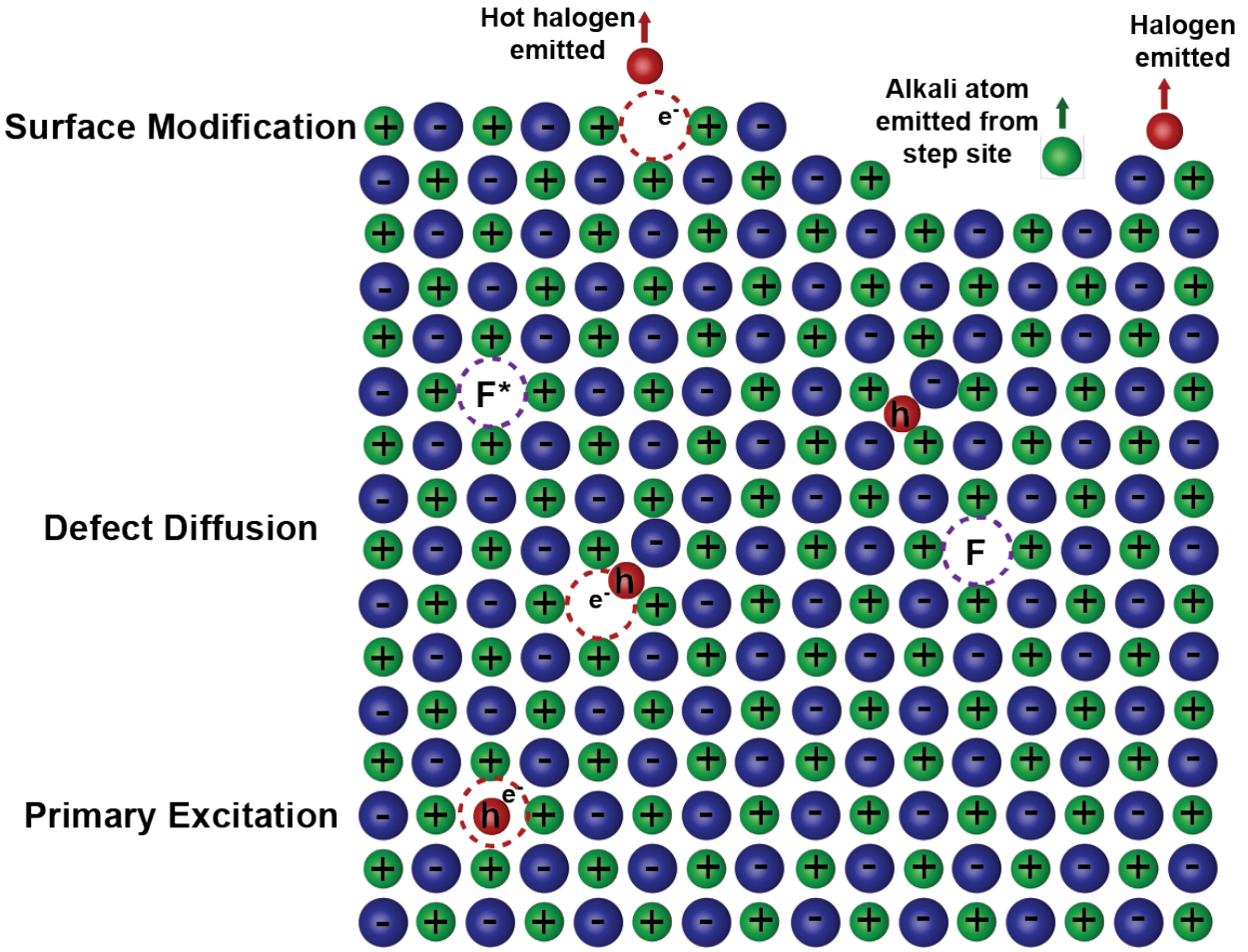

Figure 5.4: Mechanism of electron beam stimulated desorption of alkali halides, showing the primary excitation, diffusion of defects to the surface, and ultimate emission of atoms from the surface.

in the material, leading to defect production and diffusion. If thermalisation of the excitation products (free excitons and electron-hole pairs) occurs, the electrons and holes will cause lattice rearrangements to minimize energy. This will cause Frenkel defects (F- and H-centers) in the bulk, leading to diffusion and recombination at the surface.[91] Since the experiments presented here are performed at relatively high electron beam dose rates and energies, lattice rearrangement may have less of a role in the observed behavior.[94] Figure 5.4 shows the different stages of electron stimulated desorption including Primary Excitation, Defect Diffusion, and Surface Modification. *In situ* TEM of nanoparticles has the ability to observe the surface dynamics of electron stimulated desorption far better than internal defect mechanisms, but it is useful to be aware of the underlying processes.

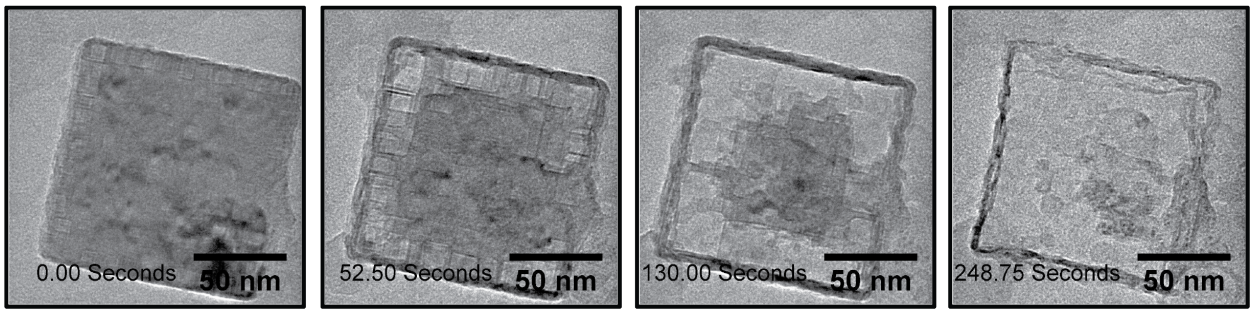

Figure 5.5: Representative images from the TEM video of electron stimulated desorption of NaCl nanocube induced by the electron beam.

The observation of electron stimulated desorption of NaCl nanocrystals was actually an unintended result, as the original experiment was designed to use an aqueous NaCl solution with metallic nanocrystals in a graphene liquid cell. The liquid pockets dried out, leaving NaCl nanocubes and rectangular prisms, whose composition was confirmed by electron diffraction. Although all these studies were performed in a dry graphene liquid cell, we do not think that the results are dependent on being between graphene sheets. Upon electron beam irradiation, rectangular features appear on the surface of the nanocrystal, consistent with the atomic layer surface desorption documented for bulk alkali halides.[90,92] These rectangles often proceed from the edges and continue growing towards the center. After the top rectangular pits becomes large, a new pit can form in the next atomic layer. It could be interesting to quantify the rates of growth of the rectangular pits, and even extend the analysis to other alkali halides. The process takes around 2 minutes for the roughly 150 nm nanocube to be fully consumed. Interestingly, a rigid shell remains behind after the process has finished.

It was unexpected for an outer layer to remain because this process involves the removal of surface atoms with no literature precendent for a shell. Returning to the composition of the liquid pocket, CTAB surfactant from the silver nanoparticles likely is present, so it is possible that CTAB is attached to the surface of the NaCl nanocubes. CTAB has a positive head group and negatively charged bromine counter ion, so CTAB could interact quite strongly with the ionic NaCl surface. Although further experiments would need to be performed to confirm this hypothesis, we propose that the shell is made of CTAB and potentially a few monolayers of NaCl. The thin shell remains stable for quite a while after the NaCl nanocrystal has been consumed before eventually collapsing. (Figure 5.6) Holes in the thin shell are clearly visible, and these may be the areas through which the Na and Cl atoms escape. Some fluctuation leads to removal of a few surface NaCl atoms, and desorption proceeds from those holes. Eventually, atoms from layers under the surfactant protected surface are also removed, and once the core is detached from the surface, atoms can be removed and leave through the hole. (Figure 5.7) Additional work could go into characterizing the thin

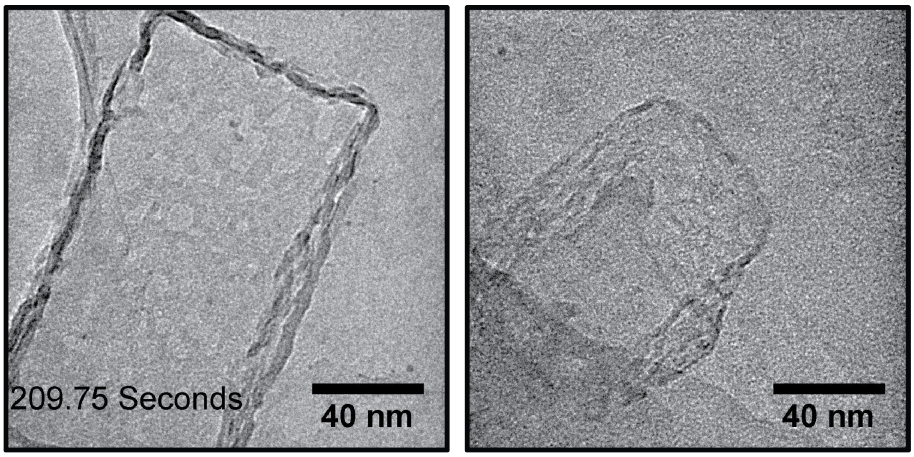

Figure 5.6: Representative images of the final structure of the remaining shell after electron stimulated desorption of NaCl nanocrystals.

shells and understanding if they have any useful properties or applications.

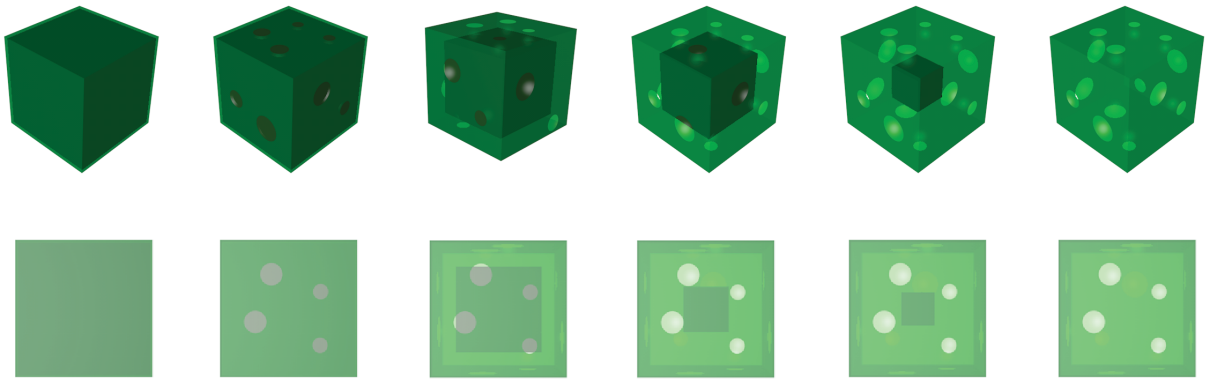

Figure 5.7: Schematic showing the process of electron stimulated desorption of NaCl nanocrystals. First, holes are formed in the shell of surfactant-protected NaCl. Then, atoms are removed from the core until the hollow shell is left behind. Top row of images are the nanocrystal at an angle and the bottom row of images are looking directly at the (100) facet.

Visualizing nanoscale processes using *in situ* electron microscopy reveals the beauty of nature while also showing potential ways to develop synthetic control for a variety of applications. Electron stimulated desorption of alkali halides generates rectangular, atomic-depth pits on the surface. For NaCl nanocrystals with surfactant on the surface, the same rectangular, atomic pits are observed, leading to layer-by-layer desorption. A thin shell is left

behind that maintains the shape of the initial nanocrystal. Further studies quantifying nanocrystal desorption rates, understanding the thin shell, performing electron beam dose rate dependence on electron stimulated desorption, and comparing different materials could yield exciting new insights into controllable nanostructures.

Chapter 6

Undergraduate Research Using Liquid Cell TEM Data

6.1 Advantages and Models for Undergraduate Research

Undergraduate research experiences can have a profound impact on the academic journey of STEM (Science, Technology, Engineering, and Mathematics) students, leading to positive outcomes such as improved performance in classes, higher self-identification as scientists, better graduation rates, and better retention of students from underrepresented demographics.[95–101] Becoming a member of a research team and working in a laboratory environment on open-ended scientific problems is an opportunity for young scientists to explore their interests and build their questioning and problem solving skills. Even on a more personal level, most current academic researchers, from graduate students to professors, can point to a transformative undergraduate research experience that set them on their current career path. Universities and scientific funding agencies have realized the importance of undergraduate research experiences and have put significant resources into getting undergraduate students into explorative, scientific environments. By understanding the current dominant models of undergraduate research, innovative programs can be developed with an inherent scalability that provides research opportunities for undergraduate students.

Arguably, the most common form of undergraduate research is the apprenticeship model where undergraduate students work directly in a research laboratory under the guidance of an experienced graduate student, post doctoral scholar, or professor.[102] This one-on-one mentorship allows for hands-on teaching of research principles and demonstration of experimental techniques. Hearing the experienced researcher's thought process and working on problems together can be a valuable learning experience for the undergraduate students, and the mentor can provide guidance and advice as the young scientist navigates their academic career and beyond. Although apprenticeship research models possess many positive attributes, there is a high cost per undergraduate researcher in terms of time and money

for the research groups. Due to the amount of investment required, apprenticeship research positions are usually designed for advanced undergraduate students who are willing to make a long-term commitment. Additionally, the research projects are usually focused on the needs of the research group without concern for the scientific maturation of the undergraduate researcher. Apprenticeship research positions are valuable experiences for experienced undergraduate students who seek a deep dive into academic research, but other models may better serve undergraduate students who simply seek to explore the research process.[103]

As a way of engaging more undergraduate students in the research mentality earlier in their college experience, many universities (including University of California-Berkeley) have implemented Course-Based Undergraduate Research Experiences (CUREs).[101,104–106] Undergraduate students enroll in a laboratory class that allows them to explore an open-ended question of their choosing. Unlike traditional "cookbook"-style laboratory classes, the undergraduate students have the opportunity to use the scientific method to work through challenging problems that lack clear answers, and students in CUREs have shown increased learning outcomes. Unfortunately, it is difficult to fully replicate an actual research environment in a laboratory class, and the range and complexity of projects is severely limited by the lack of cutting-edge equipment. Since students' interests can be wide-ranging, graduate student instructors are rarely an expert in the fields of interest and are often unable to provide the needed feedback and guidance. Additionally, in the CURE model, undergraduate students do not recieve a mentor who can help them on their academic and professional journey. Although CUREs are able to immerse larger numbers of undergraduate students in open-ended problem solving, including research groups in this early engagement would provide a more realistic experience of the research process.

Research Group-Based Undergraduate Research models (GURPs) are a hybrid between apprenticeship positions and CUREs. (Figure 6.1) In the GURP model, graduate students or post doctoral scholars from an academic research group lead a semester-long program where undergraduate students are able to use pre-collected data from the research group to ask and try to answer interesting research questions. Undergraduate students in the program learn research fundamentals while working through the scientific method in a low-stress environment. Under the guidance of experienced researchers in the field, undergraduate students learn how to come up with interesting research inquiries and then use the pre-collected data to create new knowledge. GURPs have a multiplicity factor of about 20 undergraduate students per 1-2 graduate student mentors, so this model could be advantageous for large departments that want to engage large numbers of undergraduate students in research early in their college experience. Since the research groups will be investing time guiding the undergraduate students on their projects, successful implementation of this research group-based model will involve the undergraduate students' work being beneficial to the group's research goals. Research projects with large amounts of pre-collected data that is time intensive or tedious to analyze completely seems to work well for GURPs. Undergraduate students learn about the area of research and the analysis methods while the research group gains information about the large data set. By having the undergraduate students perform data analysis instead of in-lab work, research groups save time and money training the stu-

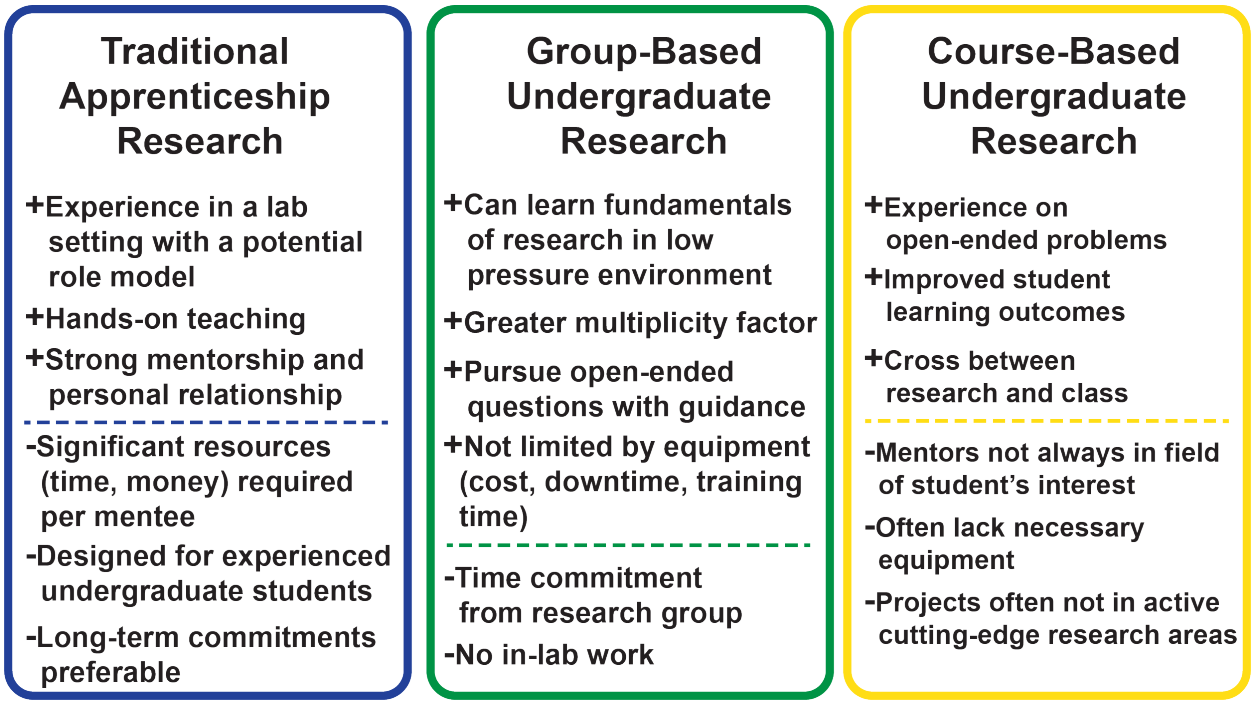

Figure 6.1: Common undergraduate research models with their associated advantages and disadvantages. The research group-based undergraduate research model tries to combine positive aspects of both apprenticeship research and CUREs.

dents on expensive and delicate equipment. Although the lack of in-lab work means that undergraduate students are not able to learn experimental techniques, the research thought process and data analysis are critical parts of scientific research. By not losing time to training and equipment malfunctions, undergraduate students are able to go through an entire research cycle in a single semester. The GURP model of undergraduate research allows more undergraduate students to engage in academic research within a research group early in their academic careers which will greatly increase the efficacy of STEM undergraduate education programs.

6.2 Alivisatos Group Undergraduate Research Program: Recruitment and Structure

During my time as a graduate student, I collaborated with Justin Ondry to develop a single semester program called the Alivisatos Group Undergraduate Research Program, or AGURP. This research opportunity was designed for first-year undergraduate students in their second semesters who had no prior research experience beyond chemistry fundamentals learned in

introductory college chemistry classes. We made announcements in the Introductory Chemistry course for first-year Chemistry majors (Chem 4A) and posted flyers in the Chemistry buildings. This program was designed to be open to every lower division student and not simply cater to the highest achieving students. To truly understand if a program like AGURP could help the learning outcomes of lower division undergraduate students, a true cross-section of the class was desired. The recruitment stressed that no prerequisite knowledge was required and the program was specifically designed for students with no prior research experience. Two informal informational sessions were held, and the application process was simply two 400-word essays on their interests and curiosity. No transcripts, letters of recommendation, or resumes were required to provide a more realistic cross-section of the student body. Recruitment yielded 60 applicants for the 20 slots in the program. The first selection criteria was attendance at one of the informational sessions or contacting us directly. AGURP required a significant time commitment from the undergraduate students, so it was important that the students understood the expectations. From the remaining 40 applicants, a random number generator was used to choose the 20 students for the program and 10 students for the wait-list. The applicants' essays were read to guage their interest in AGURP, but no students were removed due to low quality essays. Consistent with the goal of the program, most of the admitted undergraduate students in AGURP had no prior research experience. (Figure 6.2)

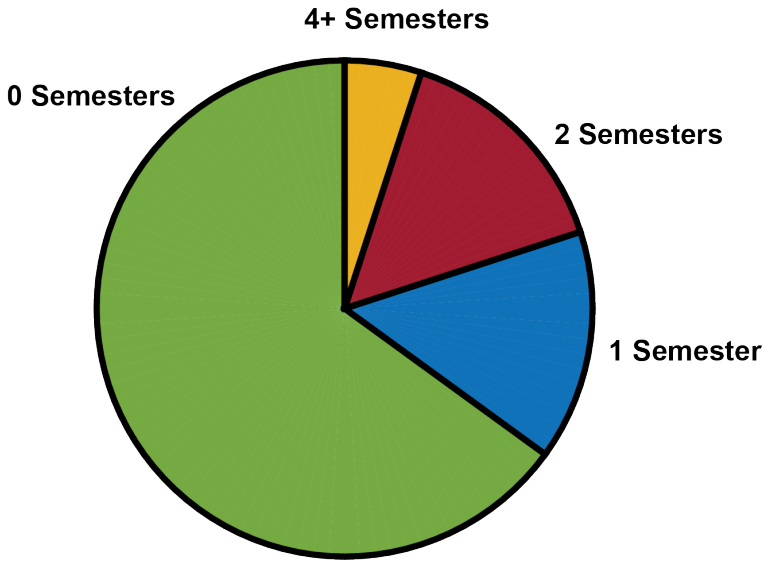

Figure 6.2: Prior research experience of undergraduate students in AGURP. The majority of participants had never done research prior to AGURP.

The semester-long program was divided into Fundamentals, Open-Ended Research, and Dissemination of Results. (Figure 6.3) Each week involved 2 one-hour meetings with about 6 hours of out-of-class work, and the students received two course credits for independent

research. Since most students came into the program with no previous nanomaterials experience, the beginning of the semester involved lectures on the the relevant fundamentals in addition to lessons on how to move beyond the theorized scientific method and actually implement the non-idealized, and sometimes messy, research process. Topics covered included technical practical knowledge such as basics on crystallography, electron microscopy, and nanocrystal growth mechanisms as well as broad skills such as how to use the scientific literature to keep up with the latest knowledge. We tried not to inundate the students with unnecessary information while also trying to make connections between this content and their coursework. The research lessons attempted to be applicable beyond simply nanomaterials, so students could utilize the skills developed in AGURP in any future research position they pursued. The research program was designed to be interactive and curiosity-driven, so lectures were kept to a minimum with most of the course time spent in peer learning activities or doing team problem solving.

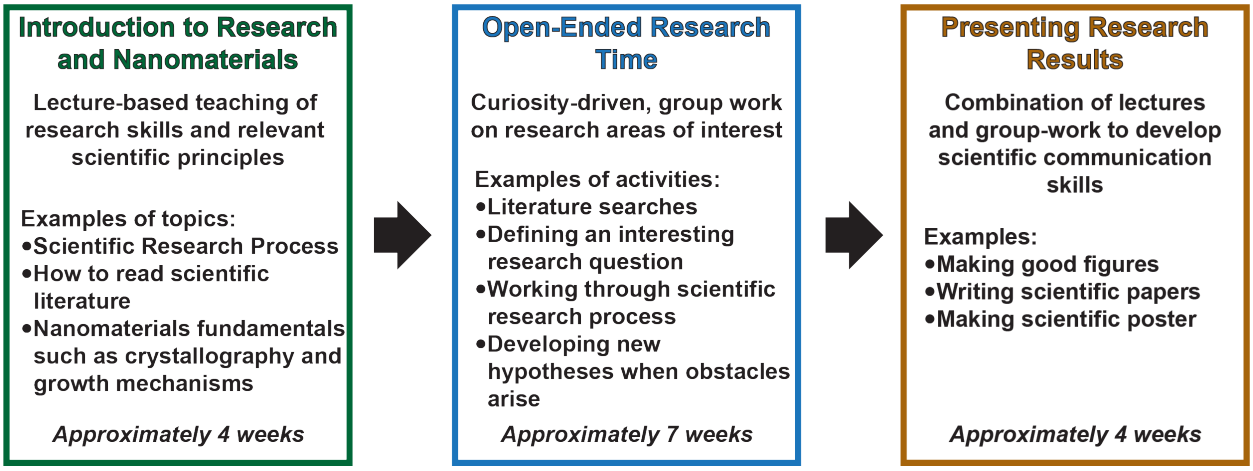

Figure 6.3: Structure of AGURP Program. After building a foundation of nanomaterials and research methodology knowledge, undergraduate students pursued curiosity-driven research on the provided data before finishing with presentations of their results.

Once the undergraduate students had formed a suitable foundation of nanomaterials research knowledge, the students were provided the pre-collected data and asked to study the data and develop an interesting question that could potentially be answered by the data. Students were grouped based on the questions they wanted to investigate, and for the rest of the research projects they worked in these teams. One of the strengths of this program was that students were given the opportunity to ask questions and test hypotheses without the pressure of the success of their hypotheses being tied to a grade. If a hypothesis was invalidated by the experiments, the students learned how to use that information to pivot to another hypothesis. Every week, each team would present their work with the associated failures and progress, similar to the traditional research group meetings held by professors

for their research groups. Through these presentations, ideas were shared, and students were able to learn from each other. Instructors were always available if students needed guidance on their research projects, but the students were encouraged to work through challenging problems in their teams. Unlike conventional courses, research does not have known right answers, so the students were taught that the only way to solve challenging research problems is to work through the process of designing experiments and testing hypotheses.

Scientific communication of research results is a critical step in the research process, so the final part of AGURP focused on how to disseminate results to the broader community. Assembling a presentation of data also is useful for the AGURP participants because it can help in understanding the flow of a research project and how each step in the process fits together to generate a complete research story. Students were given lessons on figure making and scientific writing, and then each group was asked to prepare a research poster and a final report in ACS journal format. The semester culminated in a Poster Session where participants were able to share their results with colleagues and friends. The undergraduate students in AGURP took ownership of their research projects and had the unique opportunity to experience a complete cycle of scientific research. The skills learned and confidence built during AGURP will be beneficial for the students as they continue their academic journeys with various future career goals.

6.3 Use of Electron Microscopy Data

Since AGURP is strucured around undergraduate students analyzing pre-collected data, engaging data that allows the participants to work through various hypotheses is critical for the success of the program. As mentioned previously, GURPs need to be mutually beneficial to both research groups and the undergraduate researchers, so ideally the data would require time intensive, but not overly complicated, analysis. For example, potential research data sets could include research projects with repetitive analysis or data that could be investigated from a variety of angles. The data needs to be interesting enough to keep the undergraduate students' attention but not so complex that it is not understandable in a semester. For our implementation of AGURP, we chose to use pre-collected graphene liquid cell TEM data watching growth and attachment of Pt nanocrystals. (Figure 6.4) Participants expressed multiple times their motivation to be working on actual cutting-edge data rather than a contrived experiment without broader relevance.

The original graphene liquid cell Science paper[24] was only able to fully analyze a couple of the high quality videos of platinum nanocrystal growth due to the time intensive nature of video data analysis. The Alivisatos group still has the other videos, so the AGURP students were able to analyze these high quality videos collected using a state-of-the-art electron microscope. Typically, the use of such equipment is too expensive and delicate for undergradudate researchers, so undergraduate students rarely have the opportunity to interact with such cutting-edge and relevant data. Through watching and tracking nanocrystals movement and size, the undergraduate students were able to start trying to understand

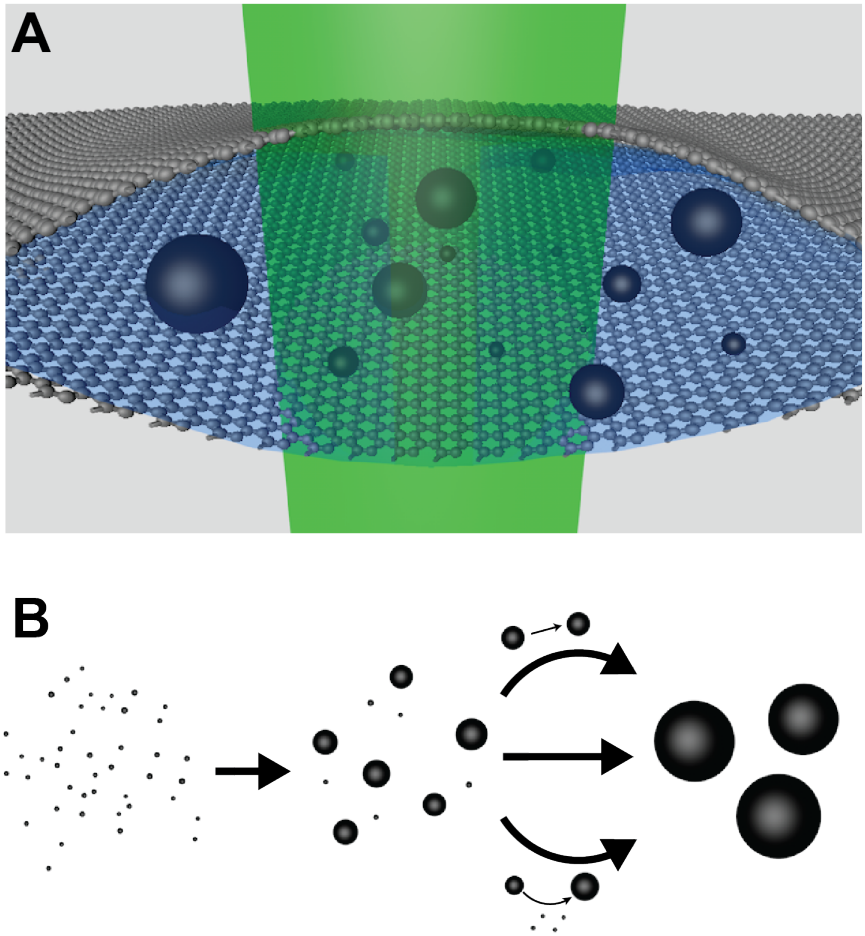

Figure 6.4: Schematics of graphene liquid cell experiments of platinum nanocrystal growth. (A) Schematic of platinum nanocrystals in a graphene liquid cell (B) Schematic of growth pathways from atomic platinum precursor to platinum nanocrystals. Example growth pathways shown are monomer addition, oriented attachment, and Ostwald ripening.

how different growth mechanisms contribute to the overall nanocrystal growth trajectories. There are numerous individual nanocrystals in each video, many with atomic resolution, (Figure 6.5) so the students could begin building up statistics on the growth trajectories. The undergraduate students developed their own projects from start to finish, so a wide variety of research questions were studied. A couple examples of titles from their final reports are *Exploring Orientation Patterns of Platinum Nanoparticles During Coalescence* and *The Dynamic Nature of the Aggregative Growth Rate Constant in Platinum Nanocrystals*. The students knew that their projects were directly building on a recent publication, so they had hope that their work could potentially lead to a future publication. AGURP participants expressed pride in contributing to an area of active research that is of interest to other professional scientists.

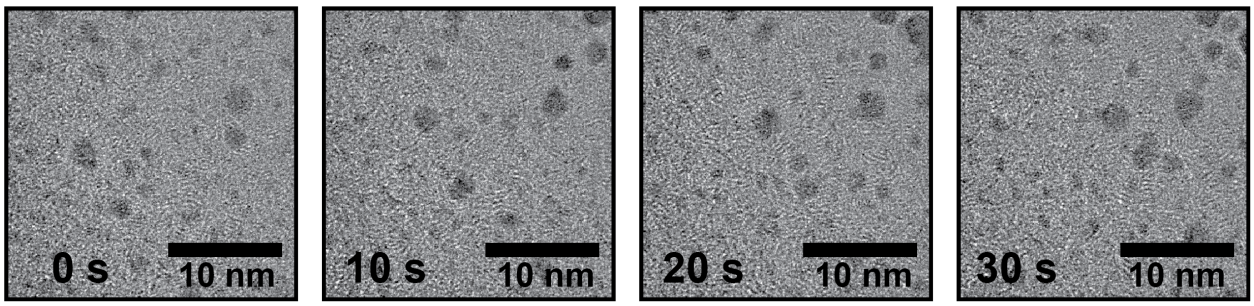

Figure 6.5: Example images from the TEM video of platinum nanocrystal growth in the graphene liquid cell. Nanocrystals can be seen moving while also changing shape and size.

6.4 Program Results

The goal of AGURP was to expose first-year undergraduate students to research and help them self-identify as scientists, so pre- and post-program surveys were administered to provide feedback on the effect of the program. These surveys also provided information about the students' background entering the program and how AGURP could be improved. Online surveys were sent to the participating students and all 20 students completed the pre- and post-program surveys. The study protocol was approved by the Internal Review Board (IRB reference no. 2018-04-10956) of the University of California-Berkeley. Questions asked the students to rate their own abilities in a number of skills relevant to nanomaterials research and also their interest level in pursuing graduate school. One-sided Welch's unequal variance t-tests were used to analyzed the survey results and determine the impact of the program. Based on the p-value differences between the pre- and post-program surveys, all of the quantitative questions were statistically different in the pre- and post- program surveys except the question about interest level in graduate school. (Table 5.1)

Question	Pre-Course Mean ± Standard Deviation	Post-Course Mean ± Standard Deviation	Difference	p-Value
How would you describe your research skills?	3.8 ± 2.0	6.4 ± 1.5	2.6	2.7×10^{-5}
How would you describe your nanomaterials knowledge?	3.6 ± 1.7	7.0 ± 0.9	3.4	4.9×10^{-9}
How would you describe your scientific literature searching skills?	5.2 ± 1.5	7.4 ± 0.8	2.2	1.0×10^{-6}
How would you describe your scientific communication skills (oral, written, PowerPoint)?	6.8 ± 1.5	8.1 ± 1.2	1.3	2.4×10^{-3}
How likely are you to pursue a graduate degree in Chemistry/Chemical Engineering/Material Science?	7.9 ± 2.5	7.8 ± 2.5	-0.1	0.55

Table 6.1: Results of AGURP Pre- and Post-Program Surveys

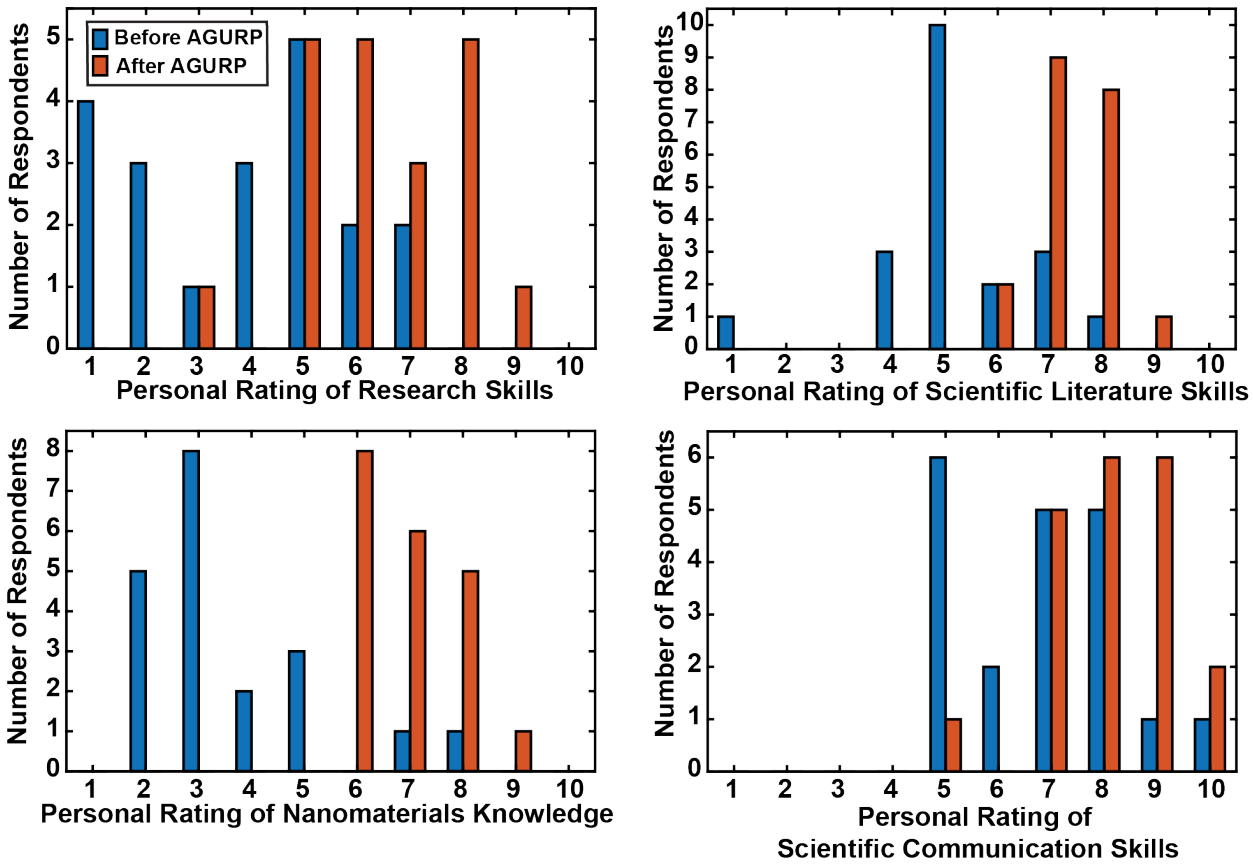

Figure 6.6: AGURP participants self-ratings for research, nanomaterials, scientific literature, and scientific communication skills on pre- and post-program surveys. Blue represents pre-program survey responses and orange represents post-program survey responses.

From qualitative observations and quantitative analysis of the survey data, the undergraduate students in AGURP significantly increased their self-identification as scientists over the course of the program. Identifying as a scientist is critical to success in STEM, especially for students from underrepresented backgrounds in STEM,[95,107] so helping undergraduate students develop a scientific identity early in their college experience is vital. In conversations with participants in AGURP, the students took ownership of their projects and were proud of their accomplishments. The undergraduate students also had quantifiable gains in their self-identification of their nanomaterials knowledge and research, scientific literature, and scientific communication skills. (Figure 6.6) Although the AGURP participants likely did not develop into nanomaterials experts over the course of a single semester, the critical takeaway is that the students felt like authentic, nanomaterials researchers. The students could leave AGURP with confidence in their accomplishment of working through a cycle of academic research, and this confidence will be valuable when they need to persevere through

challenges and obstacles on their STEM journey.

AGURP also had positive benefits for the undergraduate students as they pursued future endeavors. AGURP participants were highly likely to recommend AGURP based on our conversations and post-program surveys. (Figure 6.7) Comparing the undergraduate students' likelihood to go to graduate school shows no change; (Figure 6.7) however, convincing the students to attend graduate school was never a goal of the program. Rather, the program was designed to expose the undergraduate students to research and help them determine whether research aligns with their interests. The participants could then use that information to apply for the appropriate research or internship positions in the future. Although we did not collect data on the number of participants who recieved reseach or internship positions after AGURP, multiple students said AGURP was helpful in securing a position. Programs like AGURP are hopefully going to be mutually beneficial to undergraduate students and research groups, and it was promising that some of the students' projects had intriguing results that could be the subject of more in-depth investigation. Despite the small sample size of 20 undergraduate students in a single semester program, the early returns suggest that programs like AGURP increase first-year undergraduate students' self-identification as scientists and sets them up for future success in STEM.

6.5 Future

Based on the success of the first iteration of AGURP, the Alivisatos group plans to continue running the program with new graduate student leaders and incorporating the feedback from the AGURP participants. The visual nature of the liquid cell TEM videos was helpful for engaging the students, but other types of non-visual data should also work for this model. The next iterations of the program will use UV/Vis and fluorescence data for varieties of synthesis conditions and have the students analyze what plays a role in bright quantum dots. Feedback from the undergraduate students requested more lab tours, so future iterations will be more intentional about exposing the participants to our wet lab and instruments. Potentially, having experienced alumni from one iteration of AGURP help lead a future iteration would allow more peer-learning[108] and less time commitment from the instructors. Instructors in the first iteration of AGURP spent roughly 10-15 hours/week preparing and working on the program and about another 80-100 hours setting up the program in the prior semester. Future iterations would require much less start-up time because the structure is already developed. Early exposure to research is extremely valuable to undergraduate students, so we hope that other schools and departments will be inspired by this implementation of AGURP and use it as a model for starting their own research group-based undergraduate research programs.

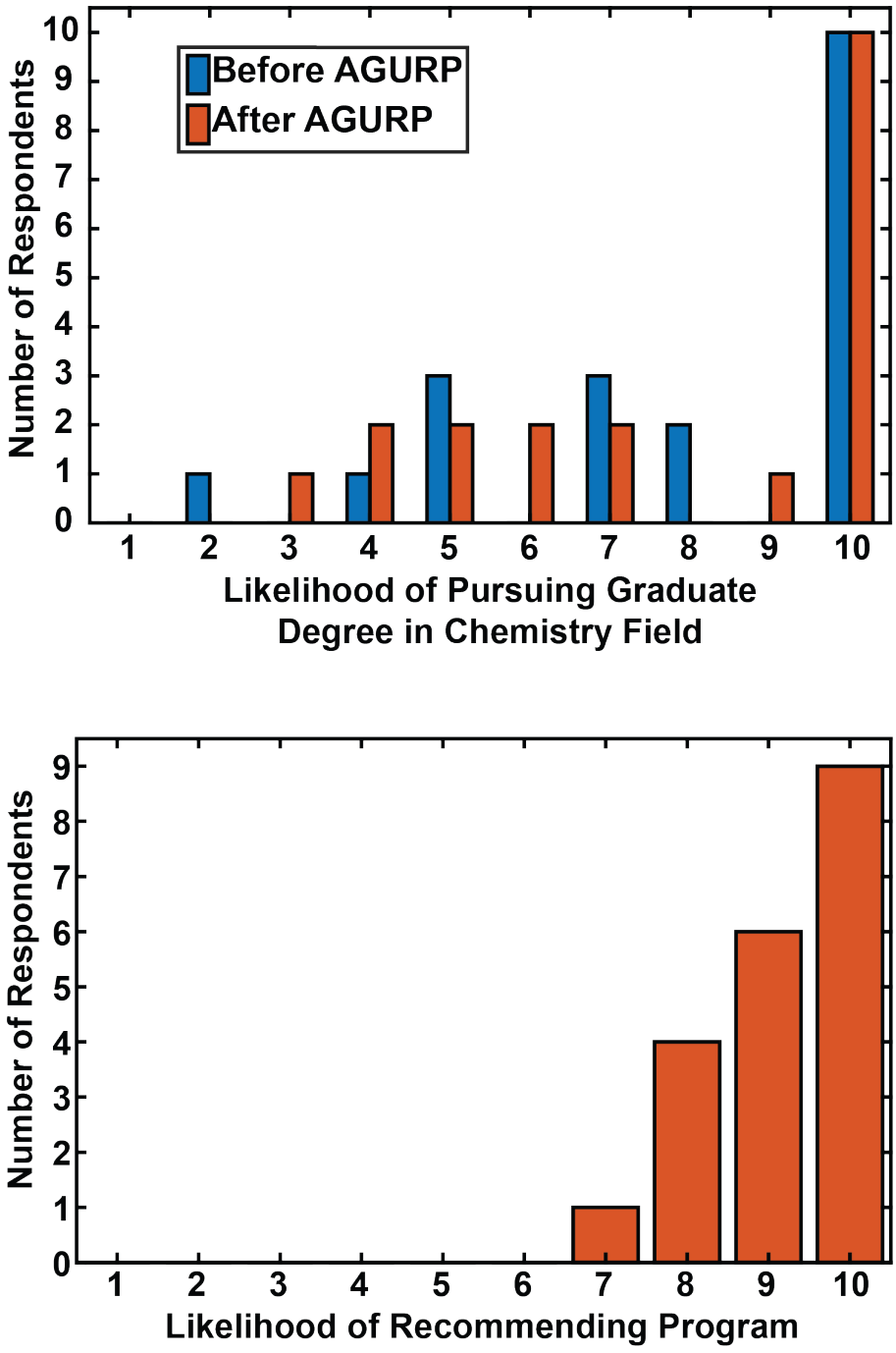

Figure 6.7: Likelihood of AGURP participants recommending the program to future students, and the likelihood of AGURP participants pursuing gradaute school in Chemistry/Chemical Engineering/Material Science

Appendix A

Supplemental Methods

A.1 Nanocrystal Synthesis

All nanocrystal syntheses followed previously published procedures. All water used was millipore filtered.

Gold Nanorods

125 μL of 10 mM $HAuCl_4$ was mixed with 5 mL of 100 mM hexadecyltrimethylammonium bromide, CTAB, (TCI) before adding 300 μL of 10 mM ice cold $NaBH_4$ (Sigma Aldrich). After stirring for 1 minute, the solution was aged for 30 minutes. 24 μL of this solution was injected into 20 mL of 100 mM CTAB, 1 mL of 10 mM $HAuCl_4$, 0.18 mL of 10 mM $AgNO_3$ (Sigma Aldrich), and 0.114 mL of 100 mM ascorbic acid (Sigma Aldrich).[109]

Gold Universal Seeds

Following previously reported procedure,[110] universal seeds were made from the nanorods for making the cubes and rhombic dodecahedra.

After redispersing in 50 mM CTAB, the optical density, OD, of the LSPR of the gold nanorods was brought to 2. Between 0.087 and 0.105 μL of 1 mM $HAuCl_4$, depending on the size of the nanorods, was added for each mL of nanorod solution and let stir gently for 4 hours at 40 degrees celsius. The universal seed solution was spun down 2 times for 30 minutes at 11,000 rpm and brought to an OD of 1 with 100 mM cetylpyridinium chloride, CPC, (TCI).

Gold Nanocubes

Between 350 and 400 μL of universal seeds, depending on the desired size of the nanocubes, was injected into a solution of 5 mL of 100 mM CPC, 500 μL of 100 mM KBr, 100 μL of 10

mM $HAuCl_4$, and 150 μL of 100 mM ascorbic acid.[110]

Gold Rhombic Dodecahedra

Between 50 and 100 μL of universal seeds, depending on the desired size of the rhombic dodecahedra, was injected into a solution of 5 mL of 100 mM CPC (TCI), 250 μL of 1 M HCl (Fischer Chemical), 13 μL of 10 mM $AgNO_3$, 250 μL of 10 mM $HAuCl_4$, and 30 μL of 100 mM ascorbic acid.[110]

Silver Nanocrystals

Note: For the work on Kirkendaal Effect of Silver Nanocrystals, Silver nanocrystals from a poly-disperse nanorod synthesis were used. Below is the Silver Nanorod Synthesis.[111]

The silver seeds were made by mixing and vigorously stirring acqueous solutions of 10 mL of 0.5 mM $AgNO_3$ and 10 mL of 0.5 mM Trisodium Citrate. $NaBH_4$ (0.6 mL, 10 mM) was added and the solution stirred for another 30 seconds. The seed solution was aged for 2 hours.

The silver nanocrystals were made by adding $AgNO_3$ (0.25 mL, 10 mM) and ascorbic acid (0.5 mL, 100 mM) to 10 mL of 80 mM CTAB. Finally, between 0.06 and 1 mL of silver seed solution (depending on desired nanocrystal size) was injected to the precursor solution before adding 0.1 mL 1 M NaOH.

A.2 Image Analysis of Nanocrystals

Converting from the 2-D TEM image projection to 3-D objects, necessary to follow the volume and shape trajectories of nanocrystals, requires a combination of image analysis techniques and geometry. First, the native dm3 files were converted to avi files using ImageJ. Then, the metadata such as electron beam dose rate and time were extracted from the files using Gatan software. Each frame of the avi file was then loaded into Matlab and converted to a matrix of grayscale values for each pixel. The pixels are then inverted because Matlab's thresholding algorithm searches for light objects. After thresholding the image to find the outline of the nanocrystal for each frame of the TEM video, geometric analysis was performed to determine the 3-D shape of each nanocrystal.

Nanorods

Following the extraction of the nanorod outline for each frame of the TEM video, the outline was sliced down the major axis. (Figure A.9) Each of the resulting half outlines were rotated around the major axis to provide two calculations of the volume using a calculus concept called the Method of Rings. This calculation of the volume assumes the nanorod is rotational symmetric. Since the two halves provide two different volume calculations, the volumes can be compared to check for rotational symmetry. The nanorods were observed to etch symmetrically as long as there was no iron oxide deposition on parts of the nanorod.

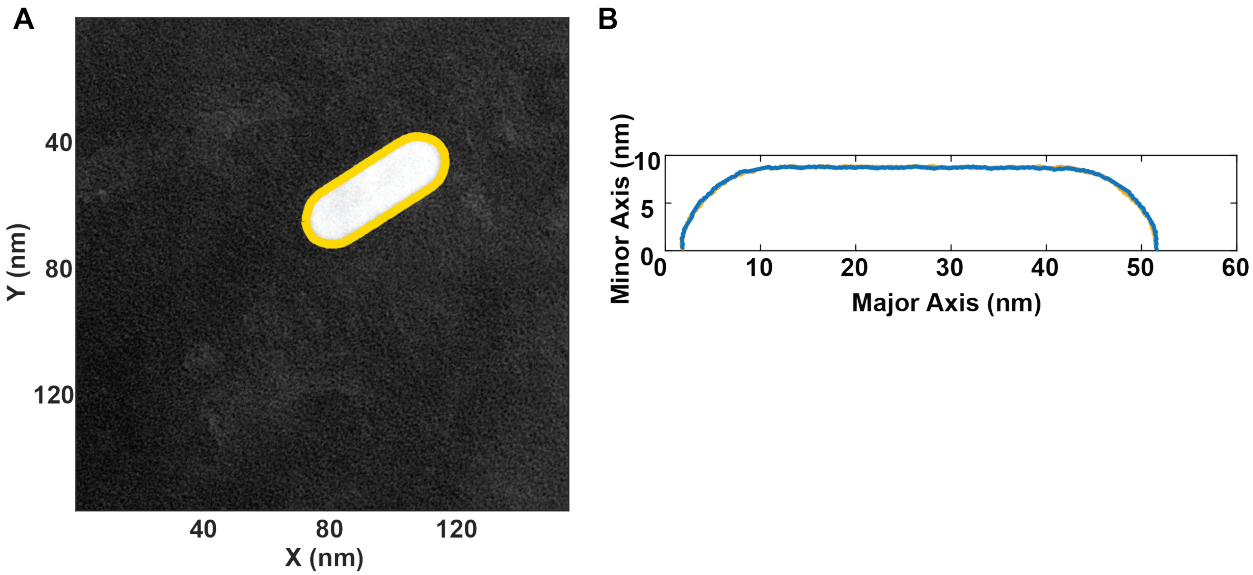

Figure A.1: Extracting the 3D geometry of gold nanorods from the 2D TEM images. A) Thresholding the TEM image finds the outline of the nanorod. B) Slicing the nanorod outline down the major axis yields two half-outlines. These outlines can be rotated around the major axis to find the volume of the nanorod.

Tetrahexahedra from Cubes

After extracting the outline of the cube/tetrahexahdra using thresholding, the distances between the center and each point on the outline were calculated. The "corners" of the shape were determined by finding the local maxima of the distances from the center. (Red dots in Figure A.8B) The facet tips (green dots in Figure A.8B) were the furthest points from a line connecting the red dots. After the facet tips were found, points a distance away from the tip (blue dots in Figure A.8B) were used to form lines (orange lines in Figure A.8B) that make up the facet. Since the tips are slightly rounded, points a distance away from the tip provide the most accurate measure of the facet. The angle between the two facet

lines were used to calculate the h/k value of the facet. (Figure A.8D) For cubes, the angle between the two facet lines would simply approach 180 degrees. To calculate the volume of the tetrahexahedra, the volume of the cube formed by the red dots was added to 6 times the volume of a pyramid with a base equal to distance between the red dots and a height corresponding to the average h/k value of the facets.

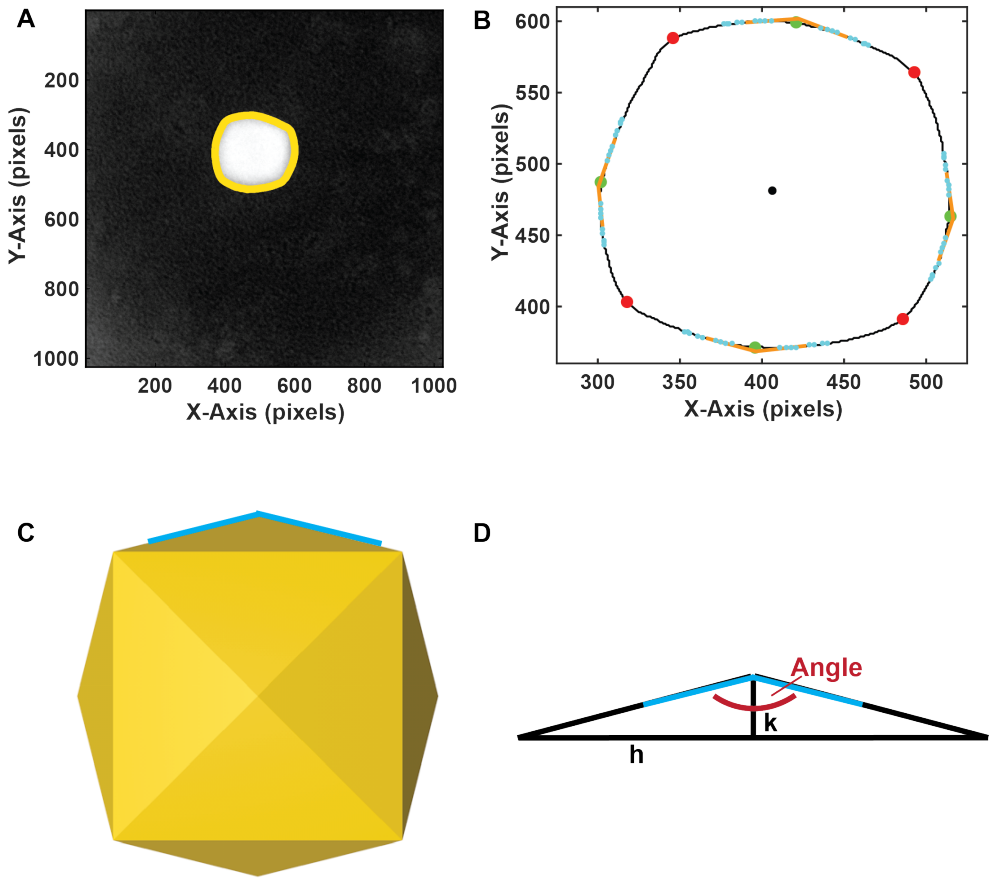

Figure A.2: Extracting the 3D geometry of tetrahexahdra etching from nanocubes. A) Thresholding the TEM image finds the outline of the tetrahexahdra. B) From the outline, the tips of the tetrahexahedra are determined by finding the points that are local maxima from the center (black dot). Once the tips are found, the points a short distance from the tip (light blue dots) are used to form lines (orange lines) that make up the facets. C) Schematic of how the lines of the facets correspond to the tetrahexahedra shape. D) Geometrically, the angle between the facets can be used to determine the h/k value of the facets.

Tetrahexahdera from Rhombic Dodecahedra

The only difference in the procedure for calculating the tetrahexahedra facets when etching from rhombic dodecahedra instead of cubes is that the nanocrystals are rotated due to different initial preferred orientations. The corners (red dots) and tips (yellow dots in Figure A.9B) are found using the local maximas in the distance to the center. The facets (orange lines) are found using points a distance away from the tips (blue dots). Geometric relations can be used to convert the angle between the two facets to an h/k value for the intermediate tetrahexahedra shape.

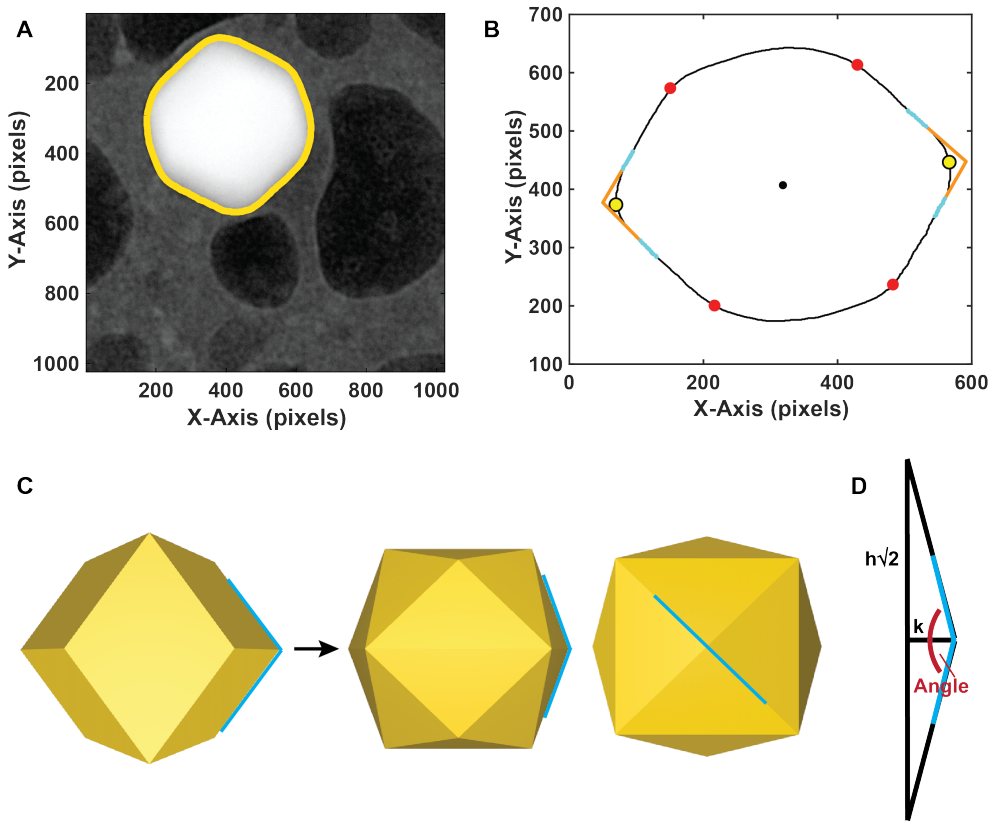

Figure A.3: Extracting 3D geometry of gold tetrahexahdra etching from rhombic dodecahedra. A) Thresholding the TEM image finds the outline of the tetrahexahdra. Notice that it is rotated from the tetrahexahdra formed from cubes. B) From the outline, the tips of the tetrahexahedra are determined by finding the points that are local maxima from the center (black dot). Once the tips are found, the points a short distance from the tip (light blue dots) are used to form lines (orange lines) that make up the facets. C) Schematic of how the lines of the facets correspond to the tetrahexahedra shape. D) Geometrically, the angle between the facets can be used to determine the h/k value of the facets.

Bibliography

[1] Yin, Y.; Alivisatos, A.; Paul, *Nature* **2005**, *437*, 664–670.

[2] Buffat, P.; Borel, J.-P. *Physical Review A* **1976**, *13*, 2287–2298.

[3] Pelton, M.; Aizpurua, J.; Bryant, G. *Laser and Photonics Reviews* **2008**, *2*, 136–159.

[4] Alivisatos, A. P. *Science* **1996**, *271*, 933–937.

[5] Jing, H.; Zhang, Q.; Large, N.; Yu, C.; Blom, D. A.; Nordlander, P.; Wang, H. *Nano Letters* **2014**, *14*, 3674–3682.

[6] Narayanan, R.; El-Sayed, M. A. *Nano Letters* **2004**, *4*, 1343–1348.

[7] Bronstein, N. D.; Yao, Y.; Xu, L.; OBrien, E.; Powers, A. S.; Ferry, V. E.; Alivisatos, A. P.; Nuzzo, R. G. *ACS Photonics* **2015**, *2*, 1576–1583.

[8] Lu, X.; Rycenga, M.; Skrabalak, S. E.; Wiley, B.; Xia, Y. *Annual Review of Physical Chemistry* **2009**, *60*, 167–192.

[9] Dreaden, E. C.; Alkilany, A. M.; Huang, X.; Murphy, C. J.; El-Sayed, M. A. *Chem. Soc. Rev.* **2012**, *41*, 2740–2779.

[10] Huang, X.; El-Sayed, I. H.; Qian, W.; El-Sayed, M. A. *Journal of the American Chemical Society* **2006**, *128*, 2115–2120.

[11] Huang, X.; El-Sayed, M. A. *Alexandria Journal of Medicine* **2011**, *47*, 1–9.

[12] Khosla, K.; Wang, Y.; Hagedorn, M.; Qin, Z.; Bischof, J. *ACS Nano* **2017**, *11*, 7869–7878.

[13] Medintz, I. L.; Uyeda, H. T.; Goldman, E. R.; Mattoussi, H. *Nature Materials* **2005**, *4*, 435–446.

[14] Xia, Y.; Gilroy, K. D.; Peng, H.-C.; Xia, X. *Angewandte Chemie International Edition* **2017**, *56*, 60–95.

[15] Ruditskiy, A.; Xia, Y. *ACS Nano* **2017**, *11*, 23–27.

[16] Wang, Y.; He, J.; Liu, C.; Chong, W. H.; Chen, H. *Angewandte Chemie International Edition* **2015**, *54*, 2022–2051.

[17] Kittel, C. *Technology*; 2004; Vol. 108.

[18] Williams, D.; Carter, C. *The Transmission Electron Microscope*, 2nd ed.; Springer, 2009.

[19] Abrams, I. M.; McBain, J. W. *Journal of Applied Physics* **1944**, *15*, 607–609.

[20] Fullam, E. F. *Review of Scientific Instruments* **1972**, *43*, 245–247.

[21] Williamson, M. J.; Tromp, R. M.; Vereecken, P. M.; Hull, R.; Ross, F. M. *Nature Materials* **2003**, *2*, 532–536.

[22] Radisic, A.; Ross, F. M.; Searson, P. C. *The Journal of Physical Chemistry B* **2006**, *110*, 7862–7868.

[23] Zheng, H.; Smith, R. K.; Jun, Y.-w.; Kisielowski, C.; Dahmen, U.; Alivisatos, A. P. *Science* **2009**, *324*, 1309–1312.

[24] Yuk, J. M.; Park, J.; Ercius, P.; Kim, K.; Hellebusch, D. J.; Crommie, M. F.; Lee, J. Y.; Zettl, A.; Alivisatos, A. P. *Science* **2012**, *336*, 61–64.

[25] Rasool, H.; Dunn, G.; Fathalizadeh, A.; Zettl, A. *physica status solidi (b)* **2016**, *253*, 2351–2354.

[26] Kelly, D. J.; Zhou, M.; Clark, N.; Hamer, M. J.; Lewis, E. A.; Rakowski, A. M.; Haigh, S. J.; Gorbachev, R. V. *Nano Letters* **2018**, *18*, 1168–1174.

[27] Ahmad, N.; Wang, G.; Nelayah, J.; Ricolleau, C.; Alloyeau, D. *Nano Letters* **2017**, *17*, 4194–4201.

[28] Hauwiller, M. R. et al. *Nano Letters* **2018**, *18*, 6427–6433.

[29] Woehl, T. J.; Evans, J. E.; Arslan, I.; Ristenpart, W. D.; Browning, N. D. *ACS Nano* **2012**, *6*, 8599–8610.

[30] Liao, H.-G.; Zherebetskyy, D.; Xin, H.; Czarnik, C.; Ercius, P.; Elmlund, H.; Pan, M.; Wang, L.-W.; Zheng, H. *Science* **2014**, *345*, 916–919.

[31] Jiang, Y.; Zhu, G.; Lin, F.; Zhang, H.; Jin, C.; Yuan, J.; Yang, D.; Zhang, Z. *Nano Letters* **2014**, *14*, 3761–3765.

[32] Wu, J.; Gao, W.; Yang, H.; Zuo, J.-M. *ACS Nano* **2017**, *11*, 1696–1703.

[33] Tan, S. F.; Anand, U.; Mirsaidov, U. *ACS Nano* **2017**, *11*, 1633–1640.

[34] Li, D.; Nielsen, M. H.; Lee, J. R. I.; Frandsen, C.; Banfield, J. F.; De Yoreo, J. J. *Science* **2012**, *336*, 1014–1018.

[35] Park, J.; Zheng, H.; Lee, W. C.; Geissler, P. L.; Rabani, E.; Alivisatos, A. P. *ACS Nano* **2012**, *6*, 2078–2085.

[36] Tan, S. F.; Chee, S. W.; Lin, G.; Mirsaidov, U. *Accounts of Chemical Research* **2017**, *50*, 1303–1312.

[37] Sutter, E.; Sutter, P.; Tkachenko, A. V.; Krahne, R.; de Graaf, J.; Arciniegas, M.; Manna, L. *Nature Communications* **2016**, *7*, 11213.

[38] Woehl, T. J.; Jungjohann, K. L.; Evans, J. E.; Arslan, I.; Ristenpart, W. D.; Browning, N. D. *Ultramicroscopy* **2013**, *127*, 53–63.

[39] Belloni, J.; Mostafavi, M.; Remita, H.; Marignier, J.-L.; Delcourt, M.-O. *New Journal of Chemistry* **1998**, *22*, 1239–1255.

[40] Hermannsdörfer, J.; de Jonge, N.; Verch, A. *Chem. Commun.* **2015**, *51*, 16393–16396.

[41] Zhang, Y.; Keller, D.; Rossell, M. D.; Erni, R. *Chemistry of Materials* **2017**, *29*, 10518–10525.

[42] Le Caër, S. *Water* **2011**, *3*, 235–253.

[43] Schneider, N. M.; Norton, M. M.; Mendel, B. J.; Grogan, J. M.; Ross, F. M.; Bau, H. H. *The Journal of Physical Chemistry C* **2014**, *118*, 22373–22382.

[44] Park, J. H.; Schneider, N. M.; Grogan, J. M.; Reuter, M. C.; Bau, H. H.; Kodambaka, S.; Ross, F. M. *Nano Letters* **2015**, *15*, 5314–5320.

[45] Cho, H.; Jones, M. R.; Nguyen, S. C.; Hauwiller, M. R.; Zettl, A.; Alivisatos, A. P. *Nano Letters* **2017**, *17*, 414–420.

[46] Hauwiller, M. R.; Ondry, J. C.; Alivisatos, A. P. *Journal of Visualized Experiments* **2018**, 1–9.

[47] Ye, X.; Jones, M. R.; Frechette, L. B.; Chen, Q.; Powers, A. S.; Ercius, P.; Dunn, G.; Rotskoff, G. M.; Nguyen, S. C.; Adiga, V. P.; Zettl, A.; Rabani, E.; Geissler, P. L.; Alivisatos, A. P. *Science* **2016**, *354*, 874–877.

[48] Hauwiller, M. R.; Frechette, L. B.; Jones, M. R.; Ondry, J. C.; Rotskoff, G. M.; Geissler, P.; Alivisatos, A. P. *Nano Letters* **2018**, *18*, 5731–5737.

[49] Bergerhoff, G.; Brown, I. D.; Allen, F. H.; Others, *International Union of Crystallography, Chester* **1987**, *360*, 77–95.

[50] Christensen, H.; Christensen, A. N.; Turpeinen, U.; Andresen, A. F.; Smidsrød, O.; Pontchour, C.-O.; Phavanantha, P.; Pramatus, S.; Cyvin, B. N.; Cyvin, S. J. *Acta Chemica Scandinavica* **1978**, *32a*, 87–88.

[51] Birch, W. D.; Pring, A.; Reller, A.; Schmalle, H. W. *American Mineralogist* **1993**, *78*, 827–834.

[52] Ross, F. M. *Science* **2015**, *350*, 1490–.

[53] Grogan, J. M.; Schneider, N. M.; Ross, F. M.; Bau, H. H. *Nano Letters* **2014**, *14*, 359–364.

[54] Yang, J.; Alam, S. B.; Yu, L.; Chan, E.; Zheng, H. *Micron* **2019**, *116*, 22–29.

[55] Lingane, J. J. *Journal of Electroanalytical Chemistry (1959)* **1962**, *4*, 332–342.

[56] Whittemore, D. O.; Langmuir, D. *Journal of Chemical & Engineering Data* **1972**, *17*, 288–290.

[57] Skibsted, L. H.; Bjerrum, J. *Journal of the Indian Chemical Society* **1977**, *54*, 102–108.

[58] Jordan, J.; Parsons, R.; Bard, A. J.; Chemistry, I. U. o. P.; Applied, *Monographs in electroanalytical chemistry and electrochemistry*; 1985; p 834.

[59] Legrini, O.; Oliveros, E.; Braun, A. M. *Chemical Reviews* **1993**, *93*, 671–698.

[60] Pashley, R. M.; Israelachvili, J. N. *Colloids and Surfaces* **1981**, *2*, 169–187.

[61] Israelachvili, J. N.; Pashley, R. M. *Nature* **1983**, *306*, 249–250.

[62] White, E. R.; Mecklenburg, M.; Singer, S. B.; Aloni, S.; Regan, B. C. *Applied Physics Express* **2011**, *4*, 055201.

[63] Shin, D.; Park, J. B.; Kim, Y. J.; Kim, S. J.; Kang, J. H.; Lee, B.; Cho, S. P.; Hong, B. H.; Novoselov, K. S. *Nature Communications* **2015**, *6*, 6068.

[64] Park, J. B.; Shin, D.; Kang, S.; Cho, S. P.; Hong, B. H. *Langmuir* **2016**, *32*, 11303–11308.

[65] Mehdi, B. L.; Qian, J.; Nasybulin, E.; Park, C.; Welch, D. A.; Faller, R.; Mehta, H.; Henderson, W. A.; Xu, W.; Wang, C. M.; Evans, J. E.; Liu, J.; Zhang, J. G.; Mueller, K. T.; Browning, N. D. *Nano Letters* **2015**, *15*, 2168–2173.

[66] Bouniol, P. *Journal of Nuclear Materials* **2010**, *403*, 167–183.

[67] Fenton, H. J. H. *J. Chem. Soc., Trans.* **1894**, *65*, 899–910.

[68] Haber, F.; Weiss, J. *Proceedings of the Royal Society A: Mathematical, Physical and Engineering Sciences* **1934**, *147*, 332–351.

[69] Pignatello, J. J.; Oliveros, E.; MacKay, A. *Critical Reviews in Environmental Science and Technology* **2006**, *36*, 1–84.

[70] Buxton, G. V.; Greenstock, C. L.; Helman, W. P.; Ross, A. B. *Journal of Physical and Chemical Reference Data* **1988**, *17*, 513–886.

[71] Ruppert, G.; Bauer, R.; Heisler, G. *Journal of Photochemistry and Photobiology, A: Chemistry* **1993**, *73*, 75–78.

[72] Ni, W.; Kou, X.; Yang, Z.; Wang, J. *ACS Nano* **2008**, *2*, 677–686.

[73] Zou, R.; Guo, X.; Yang, J.; Li, D.; Peng, F.; Zhang, L.; Wang, H.; Yu, H. *CrystEngComm* **2009**, *11*, 2797.

[74] Hauwiller, M. R.; Ondry, J. C.; Chan, C. M.; Khandekar, P.; Yu, J.; Alivisatos, A. P. *Journal of the American Chemical Society* **2019**, *141*, 4428–4437.

[75] Kirkendall, E. O. *Trans. AIME* **1942**, 104–110.

[76] Yin, Y. *Science* **2004**, *304*, 711–714.

[77] Tianou, H.; Wang, W.; Yang, X.; Cao, Z.; Kuang, Q.; Wang, Z.; Shan, Z.; Jin, M.; Yin, Y. *Nature Communications* **2017**, *8*, 1261.

[78] Chiang, R.-K.; Chiang, R.-T. *Inorganic Chemistry* **2007**, *46*, 369–371.

[79] Cabot, A.; Ibanez, M.; Guardia, P.; Alivisatos, A. P. *Journal of the American Chemical Society* **2009**, *131*, 11326–11328.

[80] Jin fan, H.; Knez, M.; Scholz, R.; Nielsch, K.; Pippel, E.; Hesse, D.; Zacharias, M.; Gösele, U. *Nature Materials* **2006**, *5*, 627–631.

[81] Fan, H. J.; Gösele, U.; Zacharias, M. *Small* **2007**, *3*, 1660–1671.

[82] Railsback, J. G.; Johnston-Peck, A. C.; Wang, J.; Tracy, J. B. *ACS Nano* **2010**, *4*, 1913–1920.

[83] Niu, K. Y.; Park, J.; Zheng, H.; Alivisatos, A. P. *Nano Letters* **2013**, *13*, 5715–5719.

[84] Susman, M. D.; Vaskevich, A.; Rubinstein, I. *The Journal of Physical Chemistry C* **2016**, *120*, 16140–16152.

[85] Yu, L.; Yan, Z.; Cai, Z.; Zhang, D.; Han, P.; Cheng, X.; Sun, Y. *Nano Letters* **2016**, acs.nanolett.6b03218.

[86] Mativetsky, J. M.; Burke, S. A.; Fostner, S.; Grutter, P. *Small* **2007**, *3*, 818–821.

[87] Alexandrov, A.; Piacentini, M.; Zema, N.; Felici, A. C.; Orlando, T. M. *Physical Review Letters* **2001**, *86*, 536–539.

[88] Tokutaka, H.; Prutton, M.; Higginbotham, I.; Gallon, T. *Surface Science* **1970**, *21*, 233–240.

[89] Höche, H.; Toennies, J. P.; Vollmer, R. *Physical Review B* **1994**, *50*, 679–691.

[90] Such, B.; Czuba, P.; Piatkowski, P.; Szymonski, M. *Surface Science* **2000**, *451*, 203–207.

[91] Szymonski, M.; Kolodziej, J.; Such, B.; Piatkowski, P.; Struski, P.; Czuba, P.; Krok, F. *Progress in Surface Science* **2001**, *67*, 123–138.

[92] Bennewitz, R.; Schär, S.; Barwich, V.; Pfeiffer, O.; Meyer, E.; Krok, F.; Such, B.; Kolodzej, J.; Szymonski, M. *Surface Science* **2001**, *474*.

[93] Mativetsky, J. M.; Miyahara, Y.; Fostner, S.; Burke, S. A.; Grutter, P. *Applied Physics Letters* **2006**, *88*, 1–4.

[94] Szymoński, M.; Kołodziej, J.; Postawa, Z.; Czuba, P.; Piatkowski, P. *Progress in Surface Science* **1995**, *48*, 83–96.

[95] Chemers, M. M.; Zurbriggen, E. L.; Syed, M.; Goza, B. K.; Bearman, S. *Journal of Social Issues* **2011**, *67*, 469–491.

[96] Linn, M. C.; Palmer, E.; Baranger, A.; Gerard, E.; Stone, E. *Science* **2015**, *347*, 1261757–1261757.

[97] Russell, S. H.; Hancock, M. P.; McCullough, J. *Science* **2007**, *316*, 548–549.

[98] Thiry, H.; Laursen, S. L.; Hunter, A.-B. *The Journal of Higher Education* **2011**, *82*, 357–388.

[99] Hunter, A.-B.; Laursen, S. L.; Seymour, E. *Science Education* **2007**, *91*, 36–74.

[100] Eagan, M. K.; Hurtado, S.; Chang, M. J.; Garcia, G. A.; Herrera, F. A.; Garibay, J. C. *American Educational Research Journal* **2013**, *50*, 683–713.

[101] Rodenbusch, S. E.; Hernandez, P. R.; Simmons, S. L.; Dolan, E. L. *CBELife Sciences Education* **2016**, *15*.

[102] Sadler, T. D.; Burgin, S.; McKinney, L.; Ponjuan, L. *Journal of Research in Science Teaching* **2009**, *47*.

[103] Wei, C. A.; Woodin, T. *CBELife Sciences Education* **2011**, *10*, 123–131.

[104] Auchincloss, L. C.; Laursen, S. L.; Branchaw, J. L.; Eagan, K.; Graham, M.; Hanauer, D. I.; Lawrie, G.; McLinn, C. M.; Pelaez, N.; Rowland, S.; Towns, M.; Trautmann, N. M.; Varma-Nelson, P.; Weston, T. J.; Dolan, E. L. *CBE Life Sciences Education* **2014**, *13*, 29–40.

[105] Szteinberg, G. A.; Weaver, G. C. *Chem. Educ. Res. Pract.* **2013**, *14*, 23–35.

[106] Full, R. J.; Dudley, R.; Koehl, M. A. R.; Libby, T.; Schwab, C. *Integrative and Comparative Biology* **2015**, *55*, 912–925.

[107] Graham, M. J.; Frederick, J.; Byars-Winston, A.; Hunter, A.-B.; Handelsman, J. *Science* **2013**, *341*, 1455–1456.

[108] Tien, L. T.; Roth, V.; Kampmeier, J. *Journal of Research in Science Teaching* **2002**, *39*, 606–632.

[109] Nikoobakht, B.; El-Sayed, M. A. *Chemistry of Materials* **2003**, *15*, 1957–1962.

[110] OBrien, M. N.; Jones, M. R.; Brown, K. A.; Mirkin, C. A. *Journal of the American Chemical Society* **2014**, *136*, 7603–7606.

[111] Jana, N. R.; Gearheart, L.; Murphy, C. J. *Chemical Communications* **2001**, 617–618.